POLITECNICO DI MILANO
Facoltà di Ingegneria dell'Informazione
Corso di Laurea Specialistica in Ingegneria Elettronica

DESIGN AND CHARACTERIZATION OF CMOS ACTIVE PIXELS WITH A TUNABLE COLOR SPACE

Relatori: **Prof. Antonio LONGONI**
Prof. Giacomo LANGFELDER

Tesi di Laurea Specialistica di
Alice PELAMATTI
matr. 751170

Anno Accademico 2010/11

Ai miei genitori e al mio fratellino ...

Ringraziamenti

Questi 5 anni al Politecnico sono stati stimolanti, duri, divertenti, lunghi, talvolta molto lunghi, stressanti ... ma sono riuscita, superando non pochi ostacoli, ad arrivare alla fine di questo percorso. E per questo voglio ringraziare tutte le persone che mi sono state vicine, chi per un pò, chi per l'intero viaggio, e che studiando con me, distraendomi, o solamente ascoltandomi mi hanno aiutata a non demordere e ad arrivare sino in fondo.

Innanzitutto desidero ringraziare *i miei genitori*, per avermi sempre incoraggiata a dare il meglio e a seguire i miei sogni, e per essere riusciti a starmi vicini nei momenti difficili, anche dall'altra parte del mondo.

Un ringraziamento al Prof. *Antonio Longoni*, per le sue lezioni cariche di passione, e per avermi permesso, insieme al Prof. *Federico Zaraga*, di lavorare a questo progetto. E un grazie di cuore a *Giacomo Langfelder*, per aver avuto fiducia in me e per avermi sopportata e supportata in quest'ultimo anno, insegnandomi, con simpatia, molto molto più di quanto potessi sperare.

Ringrazio il Professor*Franco Zappa*, che mi ha fatto scoprire l'elettronica, spingendomi ad intraprendere questo viaggio.

Ringrazio con affetto *Cosimo* e *Michi*, per l'amicizia e la simpatia con cui avete rallegrato questi 5 anni, tenendomi compagnia durante le lezioni, nelle pause pranzo e durante lunghe e gogliardiche cene.

Ringrazio tutti i miei *amici del LabLONG* per aver reso meno lunghe le mie giornate in laboratorio, tra pause caffe',chiaccherate, pettegolezzi e abbuffate. Grazie a *Cece* per l'aiuto e i prosecchini, e ad *Ale Crotti*, compagno di sventura.

Grazie a tutti i miei *acroamici*, per avermi accolta nella vostra grande famiglia, permettendomi di sfogare tutto lo stress quotidiano con flic, spaccate (magari), salti, acrocene e acrotrebbia.

Thank you, to all my Blachhof friends *Alexandra*, *Theis*, *Tim*, *Roberto*, *Fede*, **Franciccio**, **Joan**, *Omara* and all the crew, for the amazing semester in Zrich.

Un ringraziamento speciale a *Damiano*, per essermi stato vicino, rendendo questi anni ancora più speciali.

Alice

Sommario

La ricerca nel campo dell'imaging digitale si sta pian piano indirizzando verso lo sviluppo di pixel "intelligenti", capaci di adattare la loro risposta alla scena, in termini di range dinamico (intensità) e resa cromatica, e di misurarne anche altre proprietà spettrali. Il Transverse Field Detector (TFD), un innovativo pixel per sensori di immagine digitale in tecnologia CMOS, proposto di recente al Politecnico di Milano, presenta caratteristiche tali da rispondere a tali criteri. Oltre a permettere un acquisizione diretta del colore in ogni punto dell'immagine, eliminando i problemi legati agli algoritmi di demosaicing, ha uno spazio colore che può essere "accordato" semplicemente cambiando le tesioni agli anodi. Tale "accordabilità" può essere sfruttata per acquisire immagini con un numero di bande spettrali maggiore di tre.

Questa tesi descrive la simulazione e il design del TFD in una nuova tecnologia, con l'obiettivo di massimizzare la sua "tunability" spettrale e di realizzare mini-matrici attive di 2×2 pixels. In una prima parte vengono discusse le basi dell'aqcuisizione del colore, ponendo particolare attenzione alle problematiche legate alla ricostruzione del colore e alla differenza tra la riflettanza spettrale di una superficie ed il suo colore apparente, che non è una proprietà intrinseca dell'oggeto, bensì dipendente dall'illuminante. Il design è stato orientato a due applicazioni del TFD, la prima permette di migliorare l'accuratezza nella riconstruzione del colore, la seconda di misurare la riflettanza spettrale di un oggetto.

A tali scopi, la finestra di illuminazione del pixel è stata ottimizzata, trovando un buon compromesso tra Fill Factor, tunability e precisione sistematica nella ricostruzione del colore. Diverse geometrie di pixel passivi e mini-matrici attive sono state disegnate in Cadence. Inoltre è stato dimensionato e disegnato un nuovo tipo di pixel attivo, che risponde al requisito (per un corretto funzionamento del TFD) di mantenere il potenziale agli anodi fisso durante il tempo di integrazione. I dispositivi sono stati caratterizzati, risolvendo alcuni problemi che affioravano ottenendo

nel design precedente, ottenendo risultati in linea con le attese, e dimostrando le potenzialità del TFD sia in modalità RGB standard, che per acquisiszione multi-banda.

Abstract

Digital imaging is moving toward the development of ”smart” pixels, capable of adapting their response to the scene, in terms of dynamic range (intensity) and chromatic performances, and to measure other spectral properties. A recently proposed CMOS color-sensitive pixel for digital imaging applications, the Transverse Field Detector, presents characteristics that respond to these new criteria. It is a CMOS filter-less pixel whose color space can be tuned by changing the anodes biasing scheme. Its tunability allows to acquire images with a number of spectral filters greater than three.

This dissertation addresses the simulation and optimal design of the TFD in a new technology, focused on the maximization of its spectral tunability. Color imaging fundamentals are discussed in the first place, with particular attention to errors in color reconstruction and to the difference between the spectral reflectance of a surface and its apparent color, which is not an intrinsic property, but depends also on the illuminant. The design was oriented for two applications of the TFD tunability: the first to improve color accuracy, and the second to measure objects spectral reflectance.

For this purpose, the pixel illumination window has been optimized by means of simulations, finding a trade-off between Fill Factor , tunability and systematic precision in color reconstruction. The VLSI design of passive pixels and active pixels is described. Due to the additional requirement of the TFD , with respect to standard CMOS sensors, to maintain a constant anode potential during the integration time, a new active pixel topology has been designed. The devices have been characterized, solving some of the problem encoutered in the last design, and obtaining results in line with the expectations, proving the suitability of the detector for both RGB image acquisition and multi-band acquisitions.

Contents

List of Figures

Estratto

Vengono presentati i risultati del lavoro di Tesi Specialistica iniziato presso il Dipartimento di Ingegneria dell'Informazione al Politecnico di Milano nel settembre 2010. Tale lavoro si inserisce nel contesto dello sviluppo di un pixel per sensore di colore per imaging digitale, chiamato Transverse Field Detector (TFD).

Il TFD permette di misurare direttamente il colore in ogni punto della scena acquisita senza l'utilizzo di filtri colorati. I due principali vantaggi derivanti da un'acquisizione "diretta" del colore sono una maggiore efficienza quantica rispetto ai sensori CMOS con Color Filter Arrays ed il fatto di non dover ricorrere ad algoritmi di demosaicing, che introducono artifizi e riducono la risoluzione in termini di colore. Rispetto ad altri sensori "filter-less", il TFD ha la particolarità di avere uno spazio colore "tunable", il che significa che la sua sensitività spettrale può essere modificata cambiando le tensioni di polarizzazione.

In questo lavoro il TFD è stato ottimizzato per massimizzare la sua "tunability" spettrale, al fine di implementare un dispositivo capace, sia di acquisire immagini in modalità RGB standard, sia di integrare nuove funzioni. In particolare nella tesi vengono proposte due possibili applicazioni: High Color Accuracy (HCA) Imaging e Multispectral Imaging. Nella prima applicazione, la "tunability" del TFD viene sfruttata per sovracampionare le proprieta' cromatiche della scena (tramite 4 o piu' sensitivita' spettrali, ottenute tramite piu' aqcuisizioni dell'immagine con una diversa polarizzazione), riducendo cosi' l'errore di ricostruzione del colore. Il Multispectral Imaging consiste nello stimare la riflettanza spettrale di una scena, campionandola con un numero limitato di filtri equivalenti (6-8), e sfruttando la Principal Component Analysis. Questa seconda funzione è utile laddove, per problemi di costi o di ingombro, non è possibile utilizzare uno spettroscopio. Il TFD basa il suo principio di funzionamento sulla dipendenza del coefficiente di assorbimento dalla lunghezza d'onda della luce incidente. Le tre diverse componenti spettrali (rosso, verde e blu) vengono separate raccogliendo mediante tre anodi su-

perficiali, debitamente polarizzati, le cariche foto generate a diverse profondità. Tale separazione è ottenuta tramite un campo elettrico trasversale, che viene generato sovraponendo al campo elettrico verticale di svuotamento un campo orizzontale, dovuto alla differenza di tensione tra gli anodi.

Nei run precendenti sono stati testati la fattibilità tecnologica di un implementazione CMOS del dispositivo e il principio di funzionamento del TFD. In questo run sono stati realizzati sia pixel passivi con diverse geometrie (simmetrici e asimmetrici), sia mini-matrici attive di 2×2 pixel. I dispositivi sono stati realizzati in una nuova tecnologia (tecnologia 150nm di LFoundry). Il nuovo design dei pixel e' stato ottimizzato per massimizzare la tunability delle risposte spettrali. Le principali fasi di questo lavoro possono essere riassunte come segue:

- Analisi dei problemi di funzionamento dei canali verde e rosso dei pixel delle minimatrici disegnate nel run precedente. Si è ipotizzato che, a causa di un insufficiente isolamento tra pixel, scorressero correnti di punch-through tra gli anodi di pixel affacciati. Questa ipotesi è stata prima avallata da misure sperimentali, in cui si è osservato uno scambio di corrente tra i canali di due diversi pixel, poi confermata tramite simulazioni 3D ad elementi finiti (realizzate in Dessis) di due pixel di una minimatrice. In questo run è stato realizzato un migliore isolamento, la cui efficacia è stata simulata tramite ulteriori simulazioni 3D.

- Disegno e simulazione in Dessis di diverse geometrie del TFD in tecnologia a 150nm:

  - L'isolamento tra gli anodi di uno stesso pixel è stato realizzato inserendo tra un anodo e l'altro due Shallow Trench Isolation (STI), separate da una diffusione p+. Tramite simulazioni sono state valutate le tensioni per le quali la struttura entra in break-down o per le quali scorrono correnti di punch-through. Tali tensioni sono dell'ordine di 16V-18V, quindi ben superiori a quelle usate per la polarizzazione del TFD.
  - Due diverse strutture di TFD, una simmetrica e una asimmetrica, sono state disegnate in Dessis, rispettando i requisiti e le dimensioni della nuova tecnologia.
  - Per entrambe le strutture la finestra di illuminazione è stata ottimizzata al fine di ottenere un buon tuning delle risposte spettrali dei tre canali,

mantenendo un Fill Factor (FF) accettabile. In particolare per il pixel simmetrico si è scelta una finestra centrale corrispondente ad un FF del 31%, mentre per il pixel asimmetrico è stata scelta una finestra laterale corrispondente ad un FF del 49%. Da simulazione, il picco spettrale del canale verde ha un range di tunability di 80nm-90nm. Oltre che per ragioni di FF e tunability queste finestre sono state scelte tenendo presente che, per una buona ricostruzione del colore, è preferibile utilizzare dei filtri equivalenti ben bilanciati e con un ridotta sovrapposizione spettrale delle risposte. Dove per filtri equivalenti si intende il rapporto tra la fotocorrente misurata, e la fotocorrente che si misurerebbe all'anodo in un pixel "bianco".

- Una volta scelta la finestra di illuminazione, i filtri equivalenti dei tre canali (rosso verde e blu) del dispositivo sono stati simulati in diverse condizioni di polarizzazione. Tali risposte sono state utilizzate per valutare, tramite il toolbox di Matlab ISET, la matrice di conversione dallo spazio colore CIE XYZ ed il corrispondente errore di ricostruzione del colore. Ne è stata quindi dedotta la condizione ottima di polarizzazione per la ricostruzione del colore in un'acquisizione RGB standard, tenendo conto anche di effetti sulla propoagazione del rumore.

- Lo step successivo è stato il diegno VLSI in Cadence dei dispositivi. In particolare sono stati disegnati sia pixel passivi (simmetrici e asimmetrici) sia mini-matrici attive (costituite da 2×2 pixel simmetrici). Nei pixel attivi per sensori d'immagine CMOS la fotocorrente viene integrata sulla capacità di svuotamento del fotodiodo, per cui la tensione dell'anodo decresce proporzionalmente alla carica integrata. Invece, al fine di un buon funzionamento, gli anodi del TFD devono rimanere ad un potenziale costante durante tutto il tempo di integrazione, altrimenti verrebbe modificato il profilo del campo elettrico, e quindi la sensitività spettrale del dispositivo, cosa non accettabile durante la singola aqcuisizione. Per tale ragione si è dovuta disegnare e dimensionare un' elettronica di lettura integrata ad hoc. Nella topologia proposta in questa tesi l'integrazione avviene sulla capacità di feedback di un preamplificatore di carica costituito da un singolo transistore retroazionato negativamente. La capacità viene resettata dopo ogni integrazione tramite un transistore posto in parallelo. Il circuito di base comprende altri due transistori, uno per la po-

larizzazione del preamplificatore ed uno in configurazione source follower che permette la lettura del segnale di uscita a bassa impedenza. Vi sono inoltre due circuiti ausiliari che permettono di polarizzare il preamplificatore tramite uno specchio di corrente e di traslare il segnale di reset della capacità a seconda della tensione di polarizzazione dell'anodo. Nella tesi viene descritto il dimensionamento di tutti i transistori, supportato da simulazioni in Cadence.

- Definizione del set-up sperimentale: Il set-up sperimentale consiste in una sorgente luminosa accoppiata con un monocromatore, che opera una scansione in lunghezza d'onda; il fascio viene poi focalizzato sul sensore tramite un sistema di lenti. Il segnale dei tre canali colore viene misurato su tutto l'intervallo del visibile (da 400nm a 700nm) facendo uno sweep sulla lunghezza d'onda tramite il monocromatore. I dispositivi sono stati bondati su una board a componenti discreti, che permette di leggere i segnali di uscita e di polarizzare gli anodi. La lettura dei segnali in uscita e la polarizzazione degli anodi sono gestite tramite routine Labview.

  Per le mini-matrici attive, la board di lettura, i cui circuiti sono stati simulati e disegnati in Orcad, fornisce anche il segnale di riferimento per il reset delle capacità di feedback su cui viene integrata la carica. Per poter polarizzare lo stadio di uscita dell'elettronica integrata e leggere il segnale, sono stati disegnati dei generatori di corrente stabilizzati a componenti discreti, uno per ogni canale, che, grazie ad una retroazione negativa, garantiscono una alta resistenza di uscita ($> 9G\Omega$). Poiché per una delle mini-matrici non è stato disegnato un traslatore integrato, sulla board sono stati disegnati anche 3 traslatori di tensione per il segnale di reset dei 3 canali colore dei pixel della minimatrice.

  Per i pixel passivi è stata utilizzata una diversa board di lettura (il cui disegno non è stato oggetto di questa tesi).

- Misure sperimentaIi: i pixel passivi e le mini-matrici attive sono stati caratterizzati. In particolare le mini-matrici sono state caratterizzate in termini di rumore, linearità, range dinamico e ripetibilità, mentre per i pixel passivi sono state valutate le risposte spettrali. Le risposte spettrali delle mini-matrici non vengono presentate poiché al momento della scrittura della tesi non era disponibile un una scheda di acquisizione che permettesse di polarizzare gli

anodi alle tensioni ottime. I risultati ottenuti sia in termini di prestazioni nella ricostruzione del colore che di tunability si sono rivelati ben in linea con quelli attesi da simulazione. Una discordanza con le simulazoni è stata riscontrata per quanto riguarda la risposta del canale rosso, il cui segnale a basse lunghezze d'onda è risultato elevato di quello simulato. Nella tesi vengono analizzate alcune possibili cause questo fenomeno e presentate le soluzioni che saranno adottate nel prossimo run per provare a risolvere il problema. Per quanto riguarda l'elettronica di lettura integrata, è stato ottenuto un range dinamico di 75dB e una buona ripetibilità tra pixel. Non sono più stati riscontrati problemi di isolamento tra pixel nelle minimatrici.

Per concludere, i risultati ottenuti in questo lavoro sono molto promettenti nell'ottica dello sviluppo di un sensore capace sia di acquisire immagini in modalità RGB standard, sia di integrare uleriori funzioni che sfruttino la tunability del suo spazio colore. Per ora è stato provato il concept del TFD come pixel tunable, lo step successivo sarà la realizzazione di un prototipo di sensore avanzato. In particolare sarà necessaria un'ottimizzazione dello spazio nella disposizione dei pixel nella matrice, e uno studio sui limiti di scalabilità del sensore.

Introduction

Since the last decade, digital imaging has become an important part of everyday life: still cameras and video cameras have become consumer products and are sold in great quantities all around the world. This enormous market potential made it one of the most pervasive fields in Information Technology, and has pushed digital cameras producers to continuously propose new products with the best performance at the lowest price. Until now the CMOS Color Filter Array technology (CFA) has proved to be the most competitive one for consumer applications, and the main focus of the companies has been on pixel scaling. Today CFA technology is mature: resolution limits are now set by diffraction and no longer by pixel dimensions, and the "pixel war" has nearly come to an end. The next step for digital imaging seems to be in the direction of "smart pixels", that add new functionalities with respect to the simple RGB acquisition. The cameras of the future have to be "flexible" and "adaptable" to the scene, and this can be obtained both at pixel level and by designing a "smarter" readout circuitry. Examples of this new trend towards different solutions are filter-less pixels, which avoid demosaicing algorithms and the reduction of the quantum efficiency due to the color filters. Further examples are HDR (High Dynamic Range) and Pixel Binning technologies which allow some flexibility of the sensor response, depending on the brightness range of the scene. This new trend of the digital imaging research toward functionalities integration is strongly driven by important industries such as the automotive and the biomedical ones, but also by sectors like cultural heritage or security applications.

This Master's Thesis falls within the framework of the development of a new filter-less optical sensor with electrically tunable spectral response, called Transverse Field Detector. The device has been proposed and developed by the research group of professor A. Longoni and F. Zaraga at Politecnico di Milano. Spectral tuning enables the adaptation of the camera response to the scene characteristics, and therefore a "smart" acquisition of the image. The possible applications of such

sensors are many, both for consumer, industrial and scientific purposes. Nowadays the tunability of existing sensors is still weak. Some sensors can shift their dynamic range to optimize the contrast depending on the image brightness, but none of them can adapt to the chromaticity of the scene. Being able to tune the spectral sensitivity would enable many new features such as HCA (High Color Accuracy) Imaging, or the estimation of the scene spectral reflectance with a good approximation (Multispectral Imaging). The development of a device, with reduced costs (in standard CMOS technology), compact, embeddable and adaptable to specific applications could be of great scientific relevance.

The TFD was first conceived for color imaging applications, but the potential flexibility of the TFD still has to be fully developed. Its operating principle is based on the dependence of the Silicon absorption coefficient from the incident wavelength. Color separation is implemented by means of transverse electric fields, obtained with surface anodes, which collect electrons photo-generated at specific depths. By changing the anodes voltages, the collection depth changes, and the filters responses can be dynamically modified. This device can be designed with a number of spectral sensitivities greater than 3, without having to use complex demosaicing algorithms. This additional feature can be used for a better color reconstruction, or for IR signals acquisition in parallel to simple RGB acquisition.

This thesis was focused on the optimization of the TFD to obtain the maximum tunability of its color space, while ensuring an acceptable Fill Factor and good performances in terms of color reconstruction. The work can be divided into 4 main steps, which are described in the last three chapters. The first chapter introduces basics of Color Science and Digital Imaging technologies.

First the device has been drawn and simulated with the ISE-TCAD Dessis electron device simulator. The isolation between the anodes of one pixel and within a matrix have been verified. A symmetrical and an asymmetrical TFD structures have been drawn respecting the requirements of the technology that has been used in this run, and their spectral response for different illumination window and biasing conditions have been simulated. The results of these simulations have been used to size the illumination window to obtain a good trade-off between Fill Factor, spectral tunability and color performances. The latest have been evaluated by means of the Matlab tool ISET, which allows to calculate the Color Conversion Matrix and the error in color reconstruction.

The following chapter describes the VLSI design in Cadence of single passive

pixels and of active mini-matrices. Implementing active pixels with a Transverse Field Detector is not trivial, since standard readout electronics for CMOS active pixels cannot be used. In fact, unlike for CMOS sensors, the potential of the anodes of the TFD must not change during the integration time to maintain a constant transverse electric field profile in the device. I took part to the sizing of the readout electronics and in part of the VLSI design of the devices.

The last chapter describes the last two topics of this work: the experimental set-up and the experimental characterization of both passive pixels and active mini-matrices. In particular the spectral response of passive pixels has been measured, while mini-matrices have been characterized in terms of noise, linearity, dynamic range and Fixed Pattern Noise. The simulation and design of the board for the biasing and readout of active mini-matrices has been realized in Orcad. The measurements confirmed the simulations regarding the enormous improvement in the color performances and tunability of the device with respect to the past run. The new isolation solution for the mini-matrices have proved to work, opening doors to the design of a bigger matrix and then to the development of a complete TFD digital image sensor.

Chapter 1

Color Science and Digital Color Imaging

The word photography comes from the Greek words $\rho\tilde{\omega}\varsigma$ (photo, "light") and $\gamma\rho\alpha\phi\grave{\eta}$ (graphé, "process of writing or recording"). Thus photography is the art and science of creating pictures by recording radiation on a radiation-sensitive medium, such as a photographic film, or an electronic image sensor. This practice was born at the beginning of the 19th century, when many scientists and inventors, like Joseph Nicéphore Niépce, Louis Daguerre, John Herschel, Hercules Florence and William Fox Talbot developed the photographic process, some collaborating with each others, some unaware of the work of their colleagues. The photographic science resulted from the combination of many inventions and sciences that had been developed in the previous centuries, such as the pinhole camera, the camera obscura, optics and chemistry. The middle class of the Industrial Revolution was the perfect audience for an art that could enable faster and fancy portrait, thus the historical period had been fundamental for the development of photography. Already twenty years after the first black&white picture was taken, colored pictures were introduced by using three layers of emulsion to capture full color at every point in the image [8]. The technology kept improving and less than one century after the invention of the daguerreotype [9], pictures were made on 35mm film. The origin of digital imaging is usually timed to coincide with the invention of Charge Coupled Device (CCD) by Willard Boyle and George E. Smith at the AT & T Bell Labs in 1969, for which they were awarded a Nobel Prize for Physics in 2009 [10] [11]. In 1976 Bryce Bayer of Kodak patented the Bayer filter mosaic pattern for CCD color image

sensors, initiating Color Digital Imaging. Some years later CMOS sensors were introduced. For the first decade CCD remained the dominant technology, confining CMOS sensors to low quality cameras, but with the development of the CMOS technology, thanks to its flexibility and low cost, CMOS sensors became quickly competitive with CCDs.

Since the first digital picture was taken, digital imaging has quicker and quicker pervaded both our day-life and the industry, becoming essential for communication, entertainment, security, process control etc... In the last decade, the market, and hence research and innovation, have split into two main domains: on one side low cost sensors with high volume of production for commercial applications; on the other high performance sensors for industrial and scientific applications, which are produced in lower volume. New technologies in this field are continuously required, and a lot effort is being put by companies to continously propose innovative products, with the highest quality, at the lowest price.

In this chapter basics of radiometry and photometry will be discussed. The working principle of the Human Visual System will be described, as well as the concept of color, and the difficulties that are met in the attempt of measuring and reproducing it. The final section of this first chapter will deal with the technologies today available for color digital imaging, their strengths and their limits, to have an overview of which seems to be the trend for imaging technologies in the future.

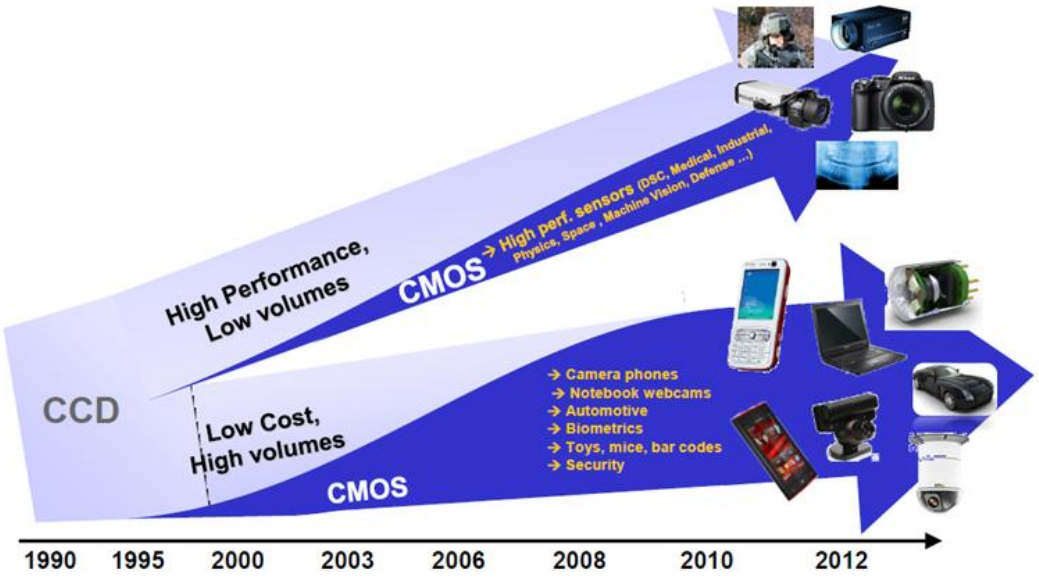

1.1 Spectrum: from the light source to the sensor

1.1.1 Light Sources and Spectral Power Distribution

Light sources are characterized by a physical property called Spectral Power Distribution (SPD), which describes the power of a light ray per unit wavelength. Spectra involved in human vision locate in the visible range, which goes approximately from 400nm to 700nm wavelength.

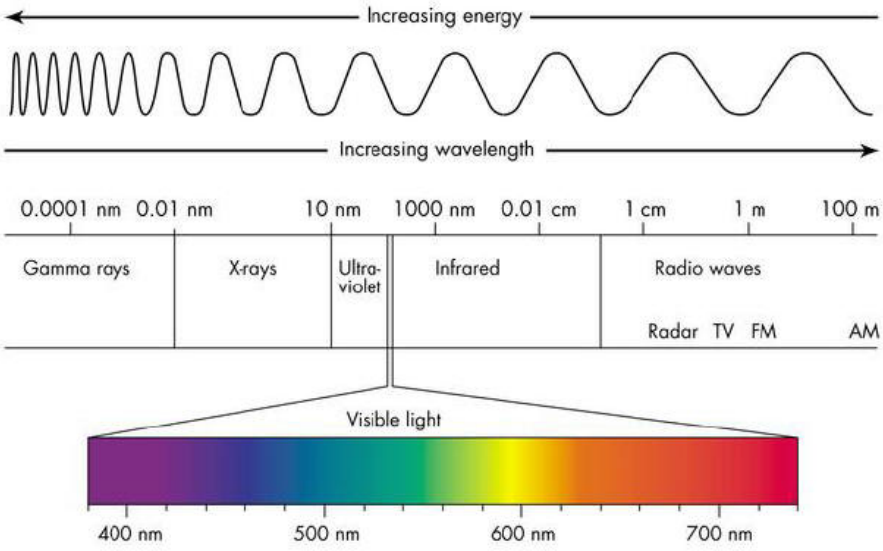

Figure 1.1 *Visible Spectrum.*

For this reason light can be quantitatively described both using radiometric and photometric units. Photometry is the science of the measurement of light in terms of its perceived brightness to the human eye. It is distinct from radiometry, which measurements the radiant energy in terms of absolute power. The conversion from photometric to radiometric units can be obtained with the following formula:

$$\Phi = \int W(\lambda) V_\lambda dx \tag{1.1}$$

where Φ [lm] is the luminous flux, $W(\lambda)[\frac{W}{nm}]$ is the SPD per unit wavelength and V_λ is the luminous efficiency curve for photopic vision, which weights each wavelength modeling the human eye sensitivity [12].

Figure 1.3 shows the Spectral Power Distribution of different light sources. Daylight has an almost flat SPD all along the visible spectrum, while tungsten lamps

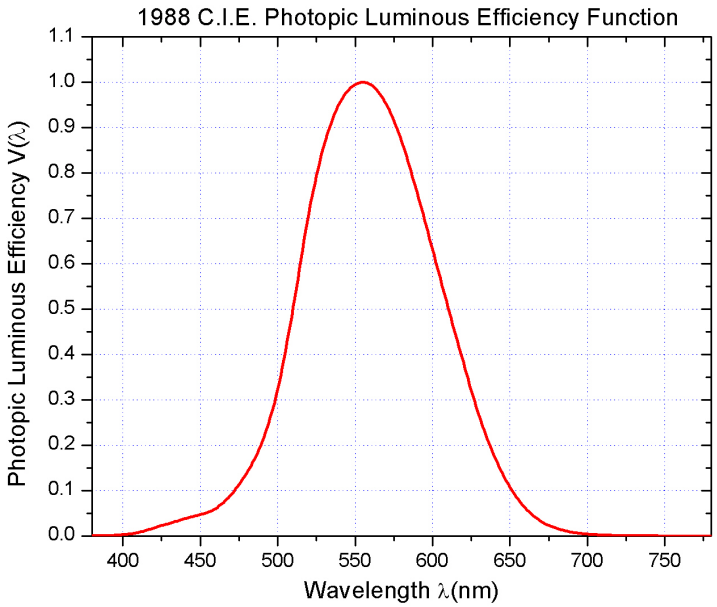

Figure 1.2 *Normalized Photopic Luminous Efficiency*

have a low luminous efficiency as their emitted power is mainly concentrated in the infrared. In comparison LED's light, thanks to its spectral sharpness, can be completely restrained to the visible spectrum.

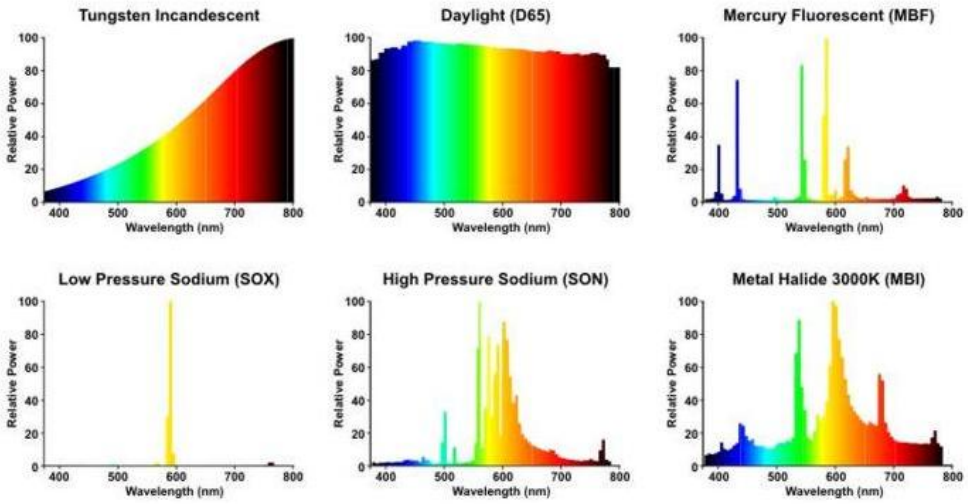

Figure 1.3 *Relative Spectral Power Distribution of some Light Sources.*

Since the incident spectrum on the image sensor strongly depends on the illumi-

nation condition, the Commission Internationale de l'Éclairage (usually abbreviated CIE) has defined a set of standard illuminants (CIE standard illuminants) and of artificial light sources (CIE standard sources). A standard illuminant is a light specified by a (relative) spectral distribution $P(\lambda)$, and a standard source is an artificial apparatus, such as an incandescent light bulb, that realizes the standard illuminant in practice. The CIE has selected incandescent light and daylight as standard illuminant [13]. One of the most commonly used standard illuminant is the D65 which corresponds roughly to a mid-day sun at medium latitudes, hence it is also called a "daylight illuminant". Figure 1.4 represents the principal standard illuminants. Illuminant A corresponds to the light emitted by an incandescent light bulb that has a spectral power distribution of a Planckian radiator at 2856 K (also called Colored Correlated Temperature), while the standard illuminant B represents noon sunlight with a CCT of 4874 K and illuminant C refers to average daylight with a CCT of 6774 K.

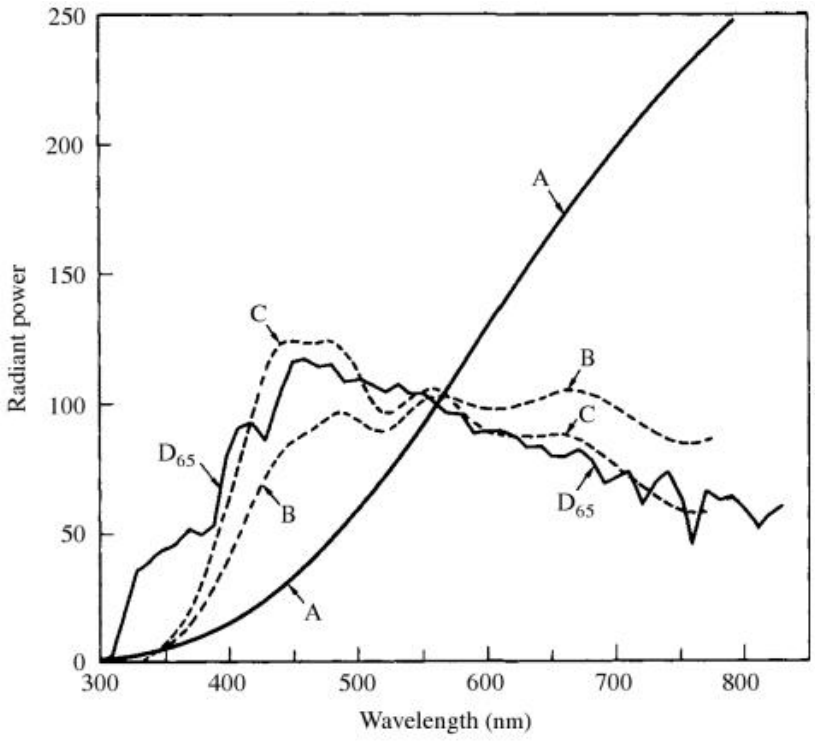

Figure 1.4 *Spectral Distribution of CIE standard illuminants A,B,C and D65*

1.1.2 Spectral Properties of Materials

If a material is irradiated, some portion of the incident optical radiation is reflected, another portion absorbed, and a third portion transmitted. Thus three spectral properties of a material can be defined: spectral reflectance, spectral transmittance and spectral absorbtance [14].

1.1.2.1 Spectral Reflectance

The spectral reflectance $R(\lambda)$ at the boundary between two materials is defined as the ratio of intensities of the reflected light to the incident light under specified geometric conditions:

$$R(\lambda) = \frac{I(\lambda)}{I_0(\lambda)} \tag{1.2}$$

where $I(\lambda)$ and $I_0(\lambda)$ are the reflected and incident intensities. Spectral reflectance applies to boundaries of all kinds of materials, including opaque, transparent and translucent [15]. For a given reflectance $R(\lambda)$ and an incident light intensity $I_0(\lambda)$, the material surface will alter the reflected light intensity as:

$$I(\lambda) = I_0(\lambda)R(\lambda) \tag{1.3}$$

The value of $R(\lambda)$ depends on the two material refraction indexes n_1 and n_0. In particular:

$$R = \frac{(n_1 - n_0)^2}{(n_1 + n_0)^2} \tag{1.4}$$

Reflectivity also varies with other parameters, such as the wavelength or the angle of incidence of the light, thus it is not a constant parameter. As an example figure 1.5 shows how silicon reflectivity changes with wavelength.

Each object is characterized by its own spectral reflectance, which doesn't depend on the spectrum of the incident light. On the other hand,the reflected spectral power distribution, and hence the color perceived by the human eye, strongly depends on the illuminant spcetrum. Figure 1.6 shows the reflected spectral power distribution of skin uder different light sources. Being spectral reflectance an intrinsic property of the object, it can be used to identify the object itself.

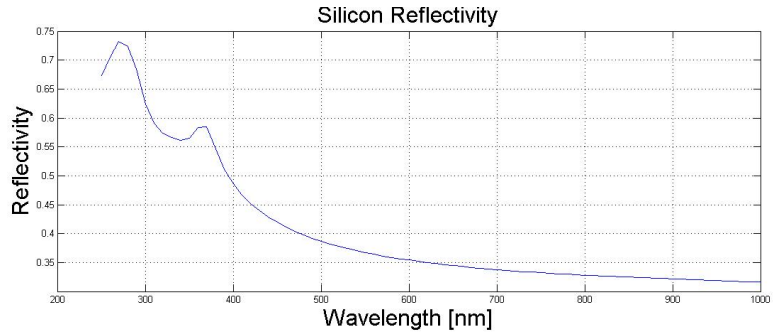

Figure 1.5 *Silicon reflectivity vs wavelength for a light incident perpendicularly to the surface*

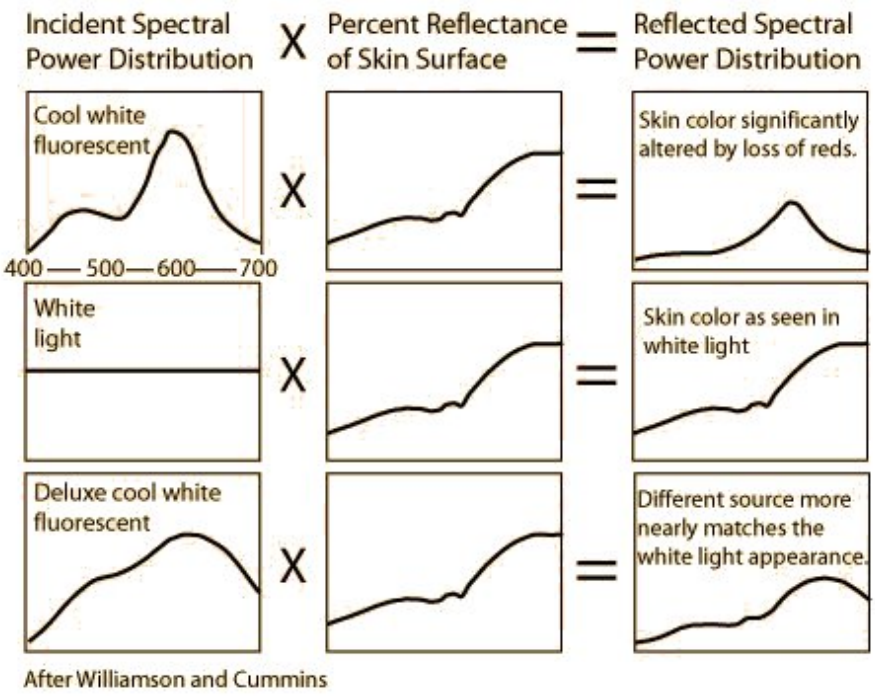

Figure 1.6 *Skin reflected spectral power distribution under various illuminants - after Williamson and Cummins*

1.1.2.2 Spectral Transmittance

The spectral transmittance at the boundary between two materials $T(\lambda)$ is the ratio of the transmitted light and incident light intensities $I(\lambda)$ and $I_0(\lambda)$ [15] :

$$T(\lambda) = \frac{I(\lambda)}{I_0(\lambda)} \tag{1.5}$$

$T(\lambda)$ can also be derived from the spectral reflectance $R(\lambda)$ at the boundary between the two material:

$$T(\lambda) = 1 - (\lambda) \tag{1.6}$$

Devices which selectively transmit light of different wavelengths are called optical filters. In photography filters are widely used to obtain color images, to eliminate IR contribution, or in general to modify the incident light spectrum. Color filters will be discussed at the end of this chapter. IR filters (or hot mirrors) are always introduced in the optical system unless the device is specifically required to measure IR. In fact while the human eye is not sensible to wavelengths over 750nm, Silicon is also sensible in the near Infra Red radiations (until 1100nm). Hence, removing the hot filter would introduce high background noise.

1.1.2.3 Spectral Absorptance: Working Principle of Quantum Photo-detectors

The working principle of quantum photo-detectors is based on light absorption. Transmitted photons are absorbed, creating electron-hole pairs (EHPs). The photon absorption process for photo-generation requires the photon energy to be at least equal to the band-gap energy E_g of the semiconductor material to excite an electron from the valence band to the conduction band. The upper cut-of wavelength λ_g is therefore:

$$\lambda_g(um) = \frac{1.24}{E_g(eV)} \tag{1.7}$$

Incident photons with wavelengths shorter than λ_g become absorbed (if the material thickness is sufficient) as they travel in the semiconductor. The light intensity, which is proportional to the number of photons, decays exponentially with distance in the semiconductor. For an homogeneous material, the light intensity $I(\lambda)$ at a

distance x from the semiconductor surface is given by Beer's law:

$$I(\lambda, x) = I_0(\lambda)e^{-\alpha(\lambda)x} \tag{1.8}$$

where $I_0(\lambda)$ is the intensity of the transmitted radiation and $\alpha(\lambda)$ is the absorption coefficient (or spectral absorbtance), that depends on the photon energy or wavelength λ, and is defined as the percentage of light energy absorbed by a material within a unit path length of light propagation.

$$\alpha(\lambda) = -\frac{1}{I(\lambda)}\frac{dI(\lambda)}{dx} \tag{1.9}$$

63% of the absorption occurs over a distance $\frac{1}{\alpha}$, also called penetration depth γ [15] [16]. Figure 1.7 shows the α vs λ charachteristics of various semiconductors, where it is apparent that α strongly depends on the material. The absorption coefficient of Silicon strongly decreases with the wavelenght within the visible spectrum. This means that blue rays will be absorbed within few hundreds nanometers, while rays at longer wavelength (i.e red light) will need around $5\mu m - 10\mu m$ to be completely absorbed.

1.1.2.4 Quantum efficiency of a Photodetector

Not all the incident photons are absorbed to create free EHPs that can be collected and create photo-current. The efficiency of conversion is called Quantum Efficiency η of the detector, and is defined as the ratio between the number of photo-generated and collected carriers and the incident number of photons. For the carriers to be collected, the photo-generation must occur in the depletion layer, or at least at a distance from it smaller than the diffusion length. In particular , being $T(\lambda)$ the transmittance of the filter (i.e. a hot mirror or a color filter or a combination of both) in front of the detector, $R(\lambda)$ the spectral reflectance of the detector surface, $\alpha(\lambda)$ the absorption coefficient of the material, x_p and x_d the depths at which the depletion layer begins and ends respectively, the quantum efficiency can be calculated as:

$$\eta(\lambda) = T(\lambda)(1 - R(\lambda))e^{-x_p\alpha(\lambda)}(1 - e^{-x_d\alpha(\lambda)}) \tag{1.10}$$

Thus the QE can be increased by reducing the reflections at the semiconductor surface, increasing absorption within the depletion layer and preventing the recombination of generated carriers before they are collected [16]. One of the main drawback

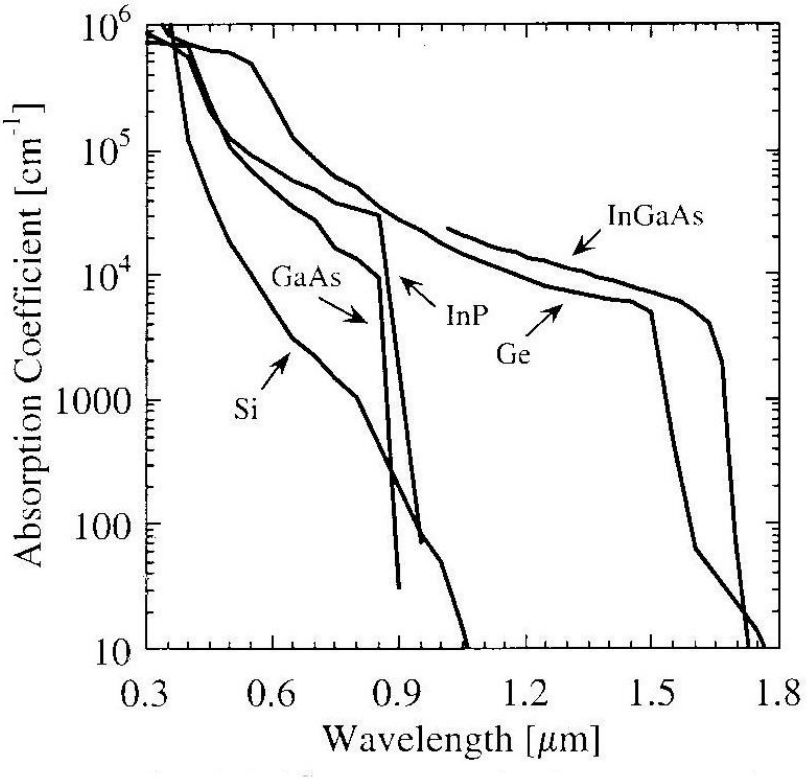

Figure 1.7 *Absorption coefficient (α) vs the wavelength (λ) for various semiconductor from the Handbook of Optical Constant Solids, edited by Edward D. Palik (1985), Academic Press NY*

of color imaging today is the presence of color filters, which obviously drastically reduce the quantum efficiency of the sensors. The solution proposed in this work avoid the use of color filters, obtaining a higher QE.

1.2 Colors: From a Psychophysical to a Mathematical Matter

"Color"is used with many different meanings, often inappropriate. Cherries are said to be "red", trees "green", coal "black"... as if color was an intrinsic property of the object. But the same object, if observed under another illuminant, will have a different apparent color. Furthermore two individuals will never have the same color perception. The Thesaurus dictionary defines color as :

> A property that becomes apparent when light falls on an object and by which things that are identical in form can be distinguished.

This definition clearly shows how hard it is to describe something which depends both on the physical properties of the incident ray, on the reflective material and on the sensation that is generated into our brain. Thus there is no color without an observer or a light source. Color is a psychophysical matter.

> "The rays, to speak properly, are not coloured. In them there is nothing else than a certain power and disposition to stir up a sensation of this or that colour".
> Isaac Newton.

> "I think that tastes, odors, colors, and so on are no more than mere names so far as the objects in which we locate them are concerned, and that they reside in consciousness. Hence if the living creature were removed, all these qualities would be wiped away and annihilated"
> Galileo Galilei, The Assayer

Color is a psychophysical concept, since every individual has a different visual system and a different brain. Being able to give a quantitative description of colors is nevertheless fundamental, especially in industries such as the automotive or the textile industry. The problem has become even more important with the diffusion

of color imaging. Cameras have to mimic the human eye, capturing enough information to reproduce images as we perceive them. Thus we need a mathematical and quantitative description of colors: this is the object of Color Science.

To describe the concept of color in a synthetic way, this section will start with the fundamentals of the human eye and will then introduce the concept of Metamerism. Finally color spaces will be described. Despite colorimetry is the subject of a vast and impressive body of empirical research and theory, color scientists, philosophers, and other cognitive scientist still strongly disagree on many points of the topic [17].

1.2.1 Fundamentals of the Human Eye

Human vision relies on the stimulation of receptors in the retina of the eye. Incident light is focused by the cornea and lens to form an image of the object being viewed on the retina. There are two types of receptors, rods and cones, names according to their shape. Rods detect low levels of illumination and give monochromatic vision, also known as "scotoptic vision". As the amount of light increases, the rods become desensitized and hibernated, and the second class of receptors, cones, begins working. Cones are insensitive to weak incident light. There are three types of cones, which work together and give color vision under normal levels of illumination ("photopic" vision). Color sensation arises when electromagnetic radiation with wavelengths of between approximately 380nm and 780nm is incident on these receptors and this stimulation is processed and interpreted by the human visual system. Stimuli that cause different colors generate different cone signals. The symbols L, M and S are used to represent the three cones with their peak sensitivities in the long, middle and short wavelength regions which correspond to blue, green, and yellow-green light respectively.[18][19][15]

Human visual system can be thought to work in a three dimensional space, since the cones integrate light (with their specific sensitivity), reducing the information of the entire spectrum of the incident light to three signals, one for each type of cone, resulting in trichromacy [18]. The sensitivity curves of the three cones and the rods are represented in figure 1.9. Since the peaks of the three curves correspond approximately to 420nm for the L cones, 534nm for the M cones and 564nm for the S cones, the receptors are also called blue, green and red receptors, respectively.

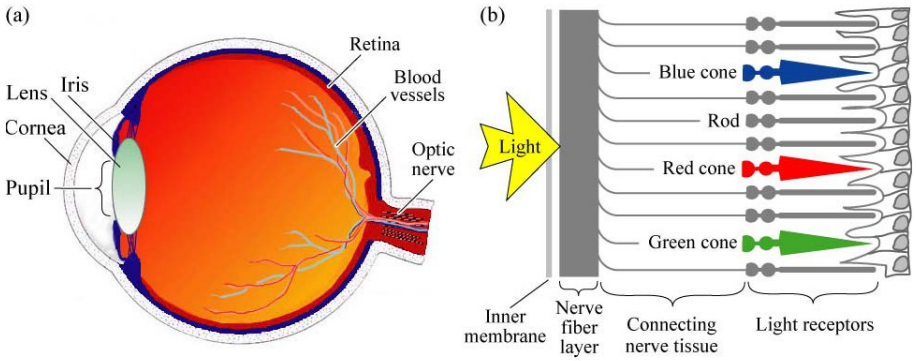

Figure 1.8 *(a) Cross section of a human eye. (b) Schematic view of the retina including rod and cone light receptors (adapted from Enciclopedia Britannica (1994) by E. F. Schubert, Light-Emitting Diodes, Cambridge Univ. Press)*

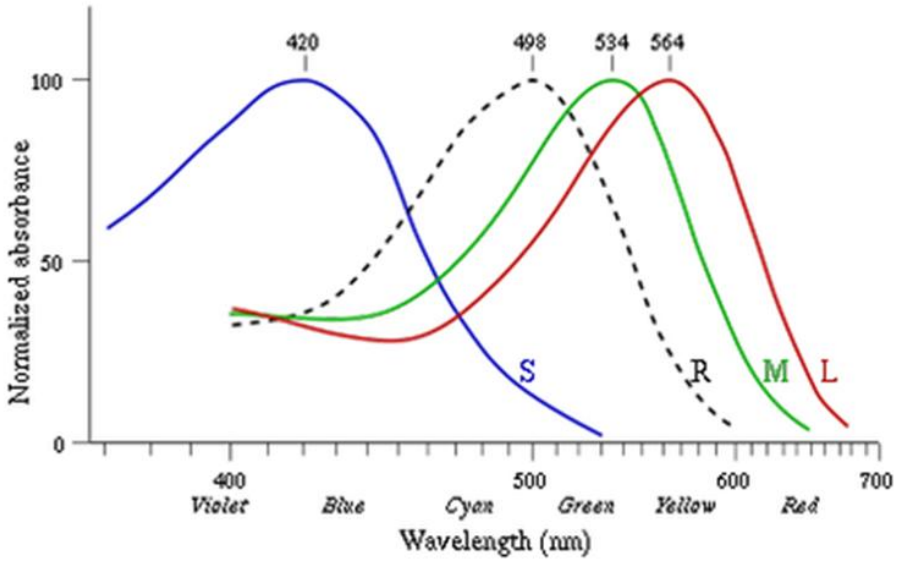

Figure 1.9 *Cones and Rods Normalized Spectral Sensitivities: the coordinates of the cones functions form the so-called LMS color space*

1.2.2 Metamerism

Two objects with a different spectral reflectance have the same apparent color under a certain illuminant if the resulting three signals of the cones are the same. This phenomenon is called metamerism. Two coloured materials are metamers, or form a metameric pair, when they match in colour, but the light they reflect differs in spectral composition. Let the $N \times 3$ matrix $\mathbf{S} = [s_1, s_2, s_3]$ represent the response of the eye, where the N vectors, s_i, correspond to the response of the i^{th} type of sensor (cone), sampled at N different wavelength (Figure 1.9). A given visible spectrum can be represented by an N vector, $\mathbf{f}$, a function whose value is radiant energy. Hence, the response of the sensors to the input spectrum is a vector $\mathbf{c}$, obtained by

$$\mathbf{c} = \mathbf{S}^T\mathbf{f} \tag{1.11}$$

Being $\mathbf{r}_1$ and $\mathbf{r}_1$ the spectral reflectances of two surfaces, $\mathbf{r}_1$ an $\mathbf{r}_1$ are said to be metamers if, under the spectrum of a certain illuminant $\mathbf{i}$ they have the same apparent color:

$$\mathbf{S}^T\mathbf{i} \cdot \mathbf{r}_1 = \mathbf{S}^T\mathbf{i} \cdot \mathbf{r}_2. \tag{1.12}$$

The two surfaces might a different color under another illuminant. Figure 1.10 shows three metamers, which appear to be identical middle gray surfaces when viewed under illuminant C. Metamerism is basically color aliasing, and its level varies across various observers, dependent on their individual cone sensitivities [19].

1.2.3 The Color Matching Experiment and the Tristimulus Functions

Since it is not practical to characterize the spectral sensitivity of all observers, the color community, in the form of the CIE, has tabulated a standard set of color matching functions that represent the response of a "standard observer" to matching monochromatic light at various wavelengths with varying intensities of three primary lights [19]. In practice, a panel of observers determines the amount of selected primary colors which must be linearly combined to match the color of a given monochromatic radiation. For example adding two monochromatic radiations at 540nm (green) and 620nm (red), of certain intensity, the resulting color matches the yellow of a monochromatic 580nm radiation [20]. The linear combination consists

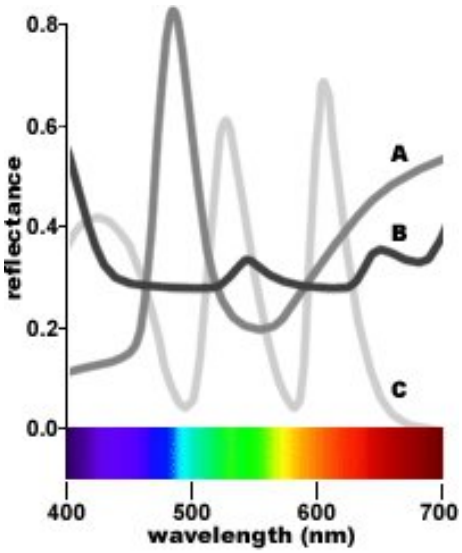

Figure 1.10 *Reflectance profiles for three metameric grays: these appear to be identical middle gray surfaces when viewed under illuminant C - after Wyszecki & Stiles (1982)*

both on the addition and on the subtraction of the primaries: the subtraction is obtained by adding one of the primaries to the target. The obtained functions depend on the chosen primaries. Figure 1.12 represents the matching functions referring to the following three primaries: $\lambda_r = 700.0$ $\lambda_g = 546.1$ $\lambda_b = 435.8$

If we let the matrix $\mathbf{A}_{RGB}$ represent the relative amount of each of the primaries required to match a standard intensity of monochromatic light, then it can be shown that $\mathbf{S}$ can be obtained by a linear transformation of the color matching matrix, $\mathbf{A}_{RGB}$. Indeed, any matrix that can be obtained by a linear transformation from $\mathbf{A}_{RGB}$ or $\mathbf{S}$ can be utilized for color matching. [19]

1.2.4 CIE 1931 XYZ Color Space

In practice, it is desirable to have a matrix of color matching functions that are nonnegative, so they can be physically realized as optical filters. This problem was addressed by the CIE, in 1931, yielding the XYZ color matching functions, also called tristimulus functions shown in Figure 1.13. Hence, the matrix $\mathbf{A}$ can now be used to represent these functions. Among all the possible linear combinations, Y was chosen to correspond to the luminous efficiency function.[19]

The coordinates corresponding to the CIE XYZ color space are referred to as tristimulus values and can be calculated as:

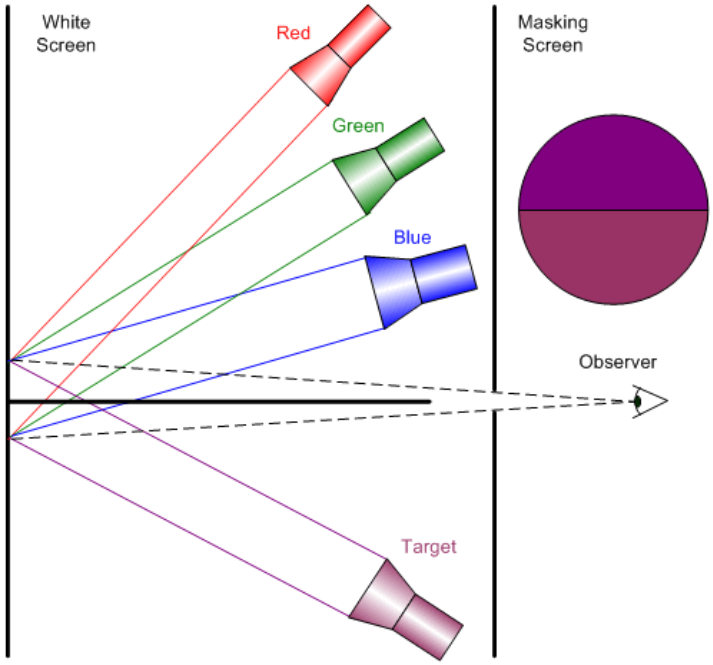

Figure 1.11 *Color Matching Experiment set-up: the observer is asked to linearly combined the three primaries to match the target monochromatic radiation*

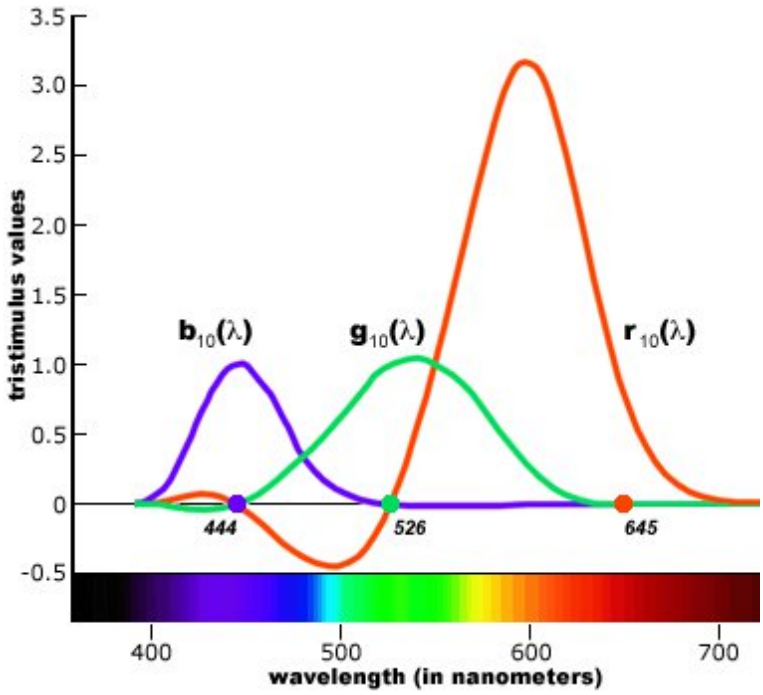

Figure 1.12 *RGB CIE 1931 matching functions*

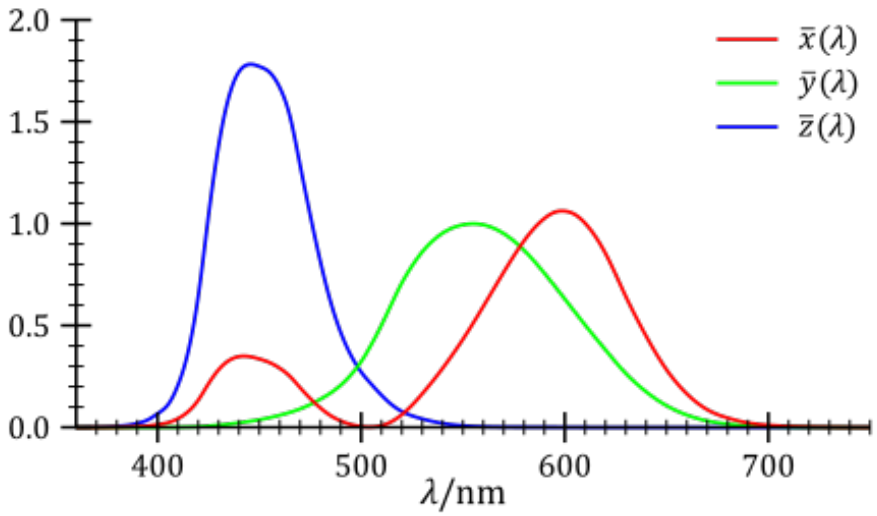

Figure 1.13 *XYZ CIE 1931 Color matching functions*

$$X = \int_{380}^{780} L(\lambda)x(\lambda)d\lambda \qquad Y = \int_{380}^{780} L(\lambda)y(\lambda)d\lambda \qquad Z = \int_{380}^{780} L(\lambda)z(\lambda)d\lambda \quad (1.13)$$

where $L(\lambda)$ is the incident SPD resulting from the product of the light source SPD and the object spectral reflectance:

$$L(\lambda) = S(\lambda)R(\lambda) \quad (1.14)$$

If we normalize X,Y we obtain the so called chromaticity coordinates:

$$x = \frac{X}{X+Y+Z} \qquad y = \frac{Y}{X+Y+Z} \quad (1.15)$$

and since:

$$z + x + y = 1 \quad (1.16)$$

The 3D color space can be fully represented by Y, x and y. A chromaticity diagram constructed from x and y, (as shown in figure 1.14) is often employed to describe the possible range of colors that can be produced by a color output device.

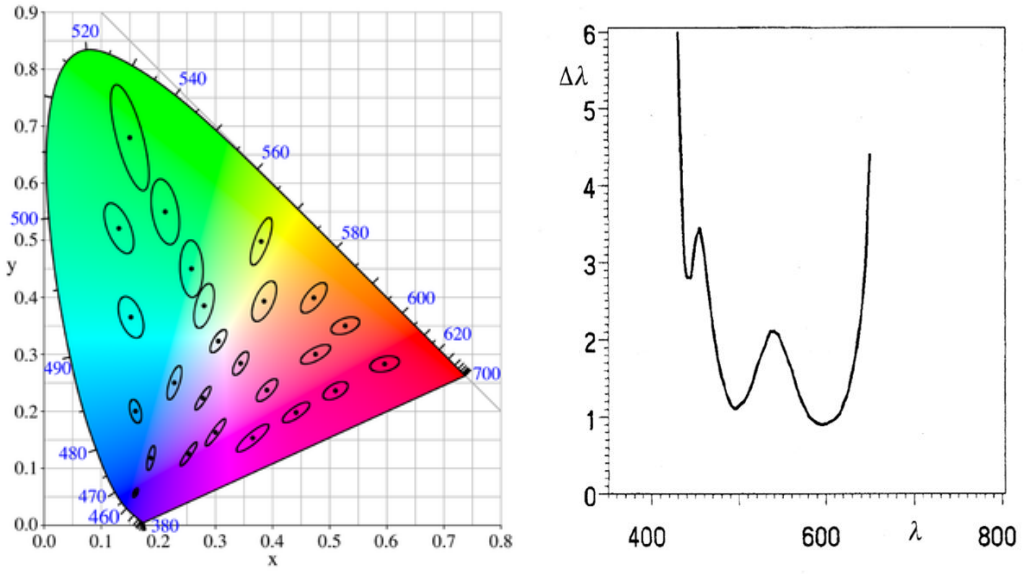

Figure 1.14 *(left)Human eye capability of evaluating color difference vs wavelength. (right)MacAdam ellipses for one of MacAdam's test participants, plotted on the CIE 1931 xy chromaticity diagram. The ellipses are ten times their actual size, as described in MacAdam's paper. The outer curved boundary is called spectral locus, and represents the coordinates of monochromatic radiations (here in nanometers)*

1.2.5 Perceptually Uniform Color Spaces

CIE 1931 XYZ color space has a drawback which strongly limits its use when it comes to evaluate color errors: it is not a perceptually uniform color space. The capability of the human eye to evaluate color difference strongly depends on the wavelength and has a peak in green and orange as it is shown in the right image of figure 1.14. This means that equal euclidean distances between points in various parts of the color space represent different perceptual color differences. Color perception difference is characterized by the Just Noticeable Difference, which is the minimum difference required between two stimuli that will elicit a perceived difference. If the Euclidean distance between two locations in a color space is proportional to the color perception difference, the color space is a perceptually uniform color space [15]. The ellipses in the xy chromaticity diagram in figure 1.14 contain all colors which are indistinguishable, to the average human eye, from the color at the center of the ellipse. The size of these ellipses is evidently not uniform over the space. Hence XYZ color space is not suitable for defining tolerances in color reproduction systems.

Other color spaces have been introduced with the intention to create a space

which can be computed via simple formulas from the XYZ space, but which is more perceptually uniform than XYZ. CIE has recommended two uniform color spaces for practical applications: the CIE 1976 L*u*v* (CIELUV) space and the CIE 1976 L*a*b* (CIELAB) space [21].

1.2.5.1 CIE 1976 L*a*b* space

In the CIE L*a*b* space a color is defined by the coordinate values L*, a* and b*, which are transformations of the CIE tristimulus values X, Y and Z:

$$
\begin{aligned}
L^* &= 116 f(Y/Y_0) - 16 \\
a^* &= 500[f(X/X_0 - f(Y/Y_0)] \\
b^* &= 200[f(Y/Y_0 - f(Z/Z_0)]
\end{aligned}
$$

where function f is defined as:

$$
\begin{aligned}
f(x) &= x^{1/3} && \text{for} && x \geq 0.008856 \\
f(x) &= 7.787x + 16/116 && \text{for} && x \leq 0.008856
\end{aligned}
$$

and X_0, Y_0 and Z_0 are the CIE XYZ tristimulus values of the reference white point.

These three coordinates represent the lightness of the color (L*=0 black and L*=100 diffuse white), its position between red/magenta and green (a* coordinate) and its position between yellow and blue (b* coordinate).

Color difference can be calculated as the euclidean distance between two colors coordinates:

$$\Delta E^*{}_{Lab} = \sqrt{(\Delta L^*)^2 + (\Delta a^*)^2 + (\Delta b^*)^2} \tag{1.17}$$

while chromaticity difference is obtained from:

$$\Delta E^*{}_{ab} = \sqrt{(\Delta a^*)^2 + (\Delta b^*)^2} \tag{1.18}$$

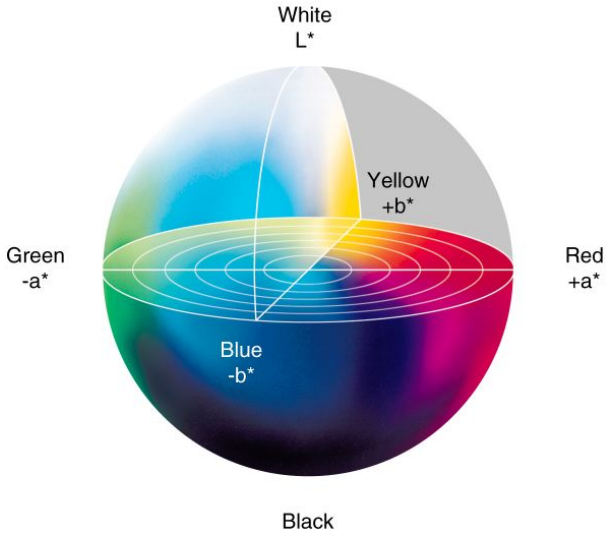

Figure 1.15 *CIE 1976 L*a*b* color space.*

1.2.5.2 Color Correction Matrix

A color space is defined to be Device Independent if there exists a nonsingular transformation between the color space and the CIE XYZ color space. For color fidelity, during the design of a color detector, the Luther-Ives condition should be respected: a color capturing device with light detectors of three types returns perfect color reproduction if and only if the sensitivities of the system are linear combinations of Cone Fundamentals (LMS color space, figure 1.9). In practice implementing physical detectors that respect such criterion would result far too expensive and complicated. Hence all physical sensors are "non colorimetric", which means that their spectral sensitivities are not linear combinations of the tristimulus functions. Thus to go from the native sensor space to an unrendered color space a non linear transformation is needed. To reduce computational costs, a linear transformation, by means of a Color Correction Matrix (CCM), is used instead.

$$\begin{bmatrix} R \\ G \\ B \end{bmatrix} = \begin{bmatrix} X_R & X_G & X_B \\ Y_R & Y_G & Y_B \\ Z_R & Z_G & Z_B \end{bmatrix} = \begin{bmatrix} X \\ Y \\ Z \end{bmatrix}$$

This simpler approach introduces an error in the color reconstruction, which depends on the chosen matrix. To minimize this error, a widely used criterion for the choice of the CCM $\mathbf{B}$ is to minimize the color reconstruction error. Given the vector of the detector sensitivities $\hat{s}(\lambda) = [r(\lambda); g(\lambda); b(\lambda)]$ and the tristimulus vector

$\bar{t}(\lambda) = [x(\lambda); y(\lambda); z(\lambda)]$, $\mathbf{B}$ is the particular matrix such that $\hat{t}$ is the best obtainable approximation of $\bar{t}$:

$$\hat{t} = \mathbf{B} \cdot \bar{s} \tag{1.19}$$

This method, named the maximum ignorance approach, is based on the minimization of the rms error $\sum(\hat{t} - \bar{t})^2$ for the overall color space. A better calculation method can be derived by observing that the colors present in a typical urban or country scene are restrained to a smaller color sub-space, as shown in figure 1.16.

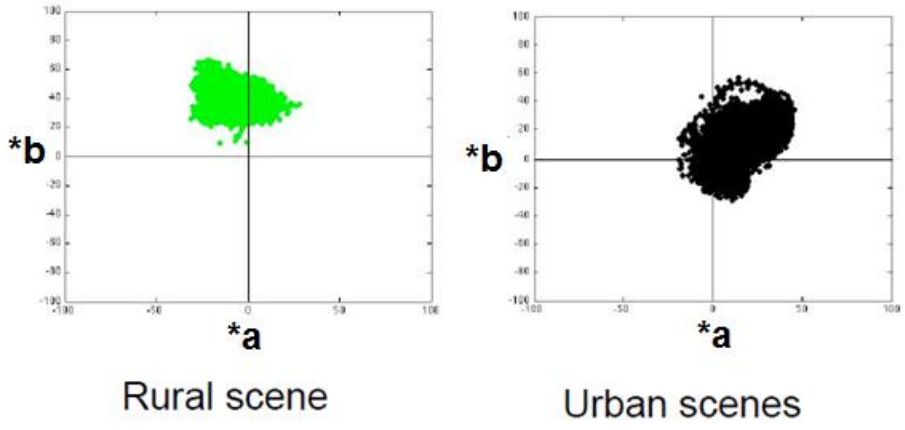

Figure 1.16 *a^*b^* chromaticity coordinates of typical urban or country scenes colors: colors appear to be not highly saturated and are restrained to a smaller sub-space*

Hence the CCM can be optimized on a reduced set of colors, resulting in a smaller color reconstruction error. In this work the CCM is calculated with ISET program, which minimizes the color error over the 24 patches of the Macbeth Color Checker (MCC) under the D_{65} illuminant shown in figure 1.17. In the same figure are represented the a^*b^* chromaticity coordinates of the MCC 24 colors: it can be observed that they define a sub-space which includes both urban and country scenes typical colors. The 24×3 matrix v_2, corresponding to the ideal RGB coordinates (derived from the tristimulus functions) of the 24 patches of the MMC , can be calculated as:

$$v_2 = \mathbf{B} \cdot v_1 \tag{1.20}$$

where v_1 is the 24×3 matrix containing the RGB color coordinates, measured in the sensor color space, of the 24 MMC patches.

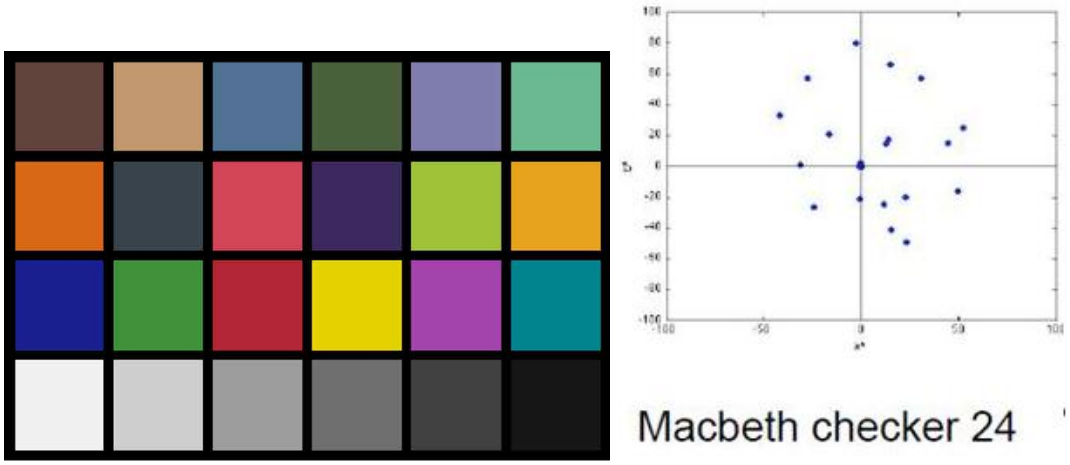

Figure 1.17 *24 patches of the Macbeth Color Checker under D_{65} illuminant (left) and their corresponding a^*b^* chromaticity coordinates (right): the color sub-space contains both the sub-spaces defined by colors in typical urban and country scenes (figure 1.16)*

1.2.6 Colorimetry and Multi-spectral imaging

Colorimetry and Multi-spectral imaging are two different ways of measuring the spectral reflectance of an object. The first is based on the human eye trichromacy and is subsequently subject to metamerism. The aim of colorimetry is to faithfully reproduce color as the human eye would perceive it, but no information is acquired about the overall spectral reflectance. On the contrary multi-spectral acquisition aims at capturing and estimating the spectral reflectance properties of the imaged scene, giving information that is independent on the illuminant spectrum. This approach is relevant for several domains and applications, including analyses of art paintings or museological objects, medicine, biomedical analysis of teeth and skin, computer graphics, multimedia, hyperspectra remote sensing, and other fields where critical color matching is important [22].

1.2.6.1 Multi-spectral imaging

There are two main approach to evaluate the spectral reflectance of an object: measuring it or estimating it. Measuring spectral reflectances is the object of Spectrography, where the spectrum is densely sampled at constant bandpass and wavelength interval by means of sharp filters. According to the CIE, tristimulus errors will not be introduced when measuring materials if a 5 nm wavelength increment and bandpass are used, hence at least 61 different channels are required. However, one should

be able to decrease the sampling increment without a significant loss of spectral information, because of the absorption characteristics of both man-made and natural colorants [23]. This second approach is based on an *a priori* spectral analysis of the sampled data, applying Principal Component Analysis (PCA), which results in data reduction and hence lower computational costs. In [24] Tzeng reviewed the main applications of PCA to color science, describing how this technique can be used to reduce the dimensionality from a large number of sampling wavelengths to a small number of eigenfunctions, typically 5 to 8. In fact, since spectral characteristics, of both man-made and natural colored surfaces are often smooth, a set of 5 to 8 sampling channel is usually sufficient for a good spectral reflectance estimation [22] [25] [24]. In [25] Parkkinen measured a set of 1257 reflectance spectra from the Munsell color chips [26], individuating eight eigenfunctions $b_k(\lambda)$ by applying the PCA through a correlation matrix to the sampled data. The seventh eighth and greater eigenvectors were found to be almost parallel to the spectra of the representative set, thus good color reconstruction can be obtained using a six dimensionality, $K_s = 6$ (indeed with more than six eigenvectors, the changes in the reconstruction would have been minimal). In the following the mathematical approach to the estimation of the spectral reflectance of a set of analyzed objects will be given as described in [22] and [27].

Let us consider the following physical quantities and coefficients, with λ being a 1×31 vector containing radiation wavelengths between 400 nm and 700 nm sampled every 10nm:

$e(\lambda)$: spectral density of the scene illuminant (in quanta);

$b_k(\lambda)$: *k-th* eigenfunction of the selected basis for spectral estimation, $k \in [1, K_S]$;

$c_m(\lambda)$: spectral response of the *m-th* sampling channel of the imaging device, $m \in [1, M]$;

$s_n(\lambda)$: spectral reflectance of the *n-th* analyzed object, $n \in [1, N]$;

$s'_n(\lambda)$: estimated spectral reflectance of the *n-th* analyzed object;

$\sigma_{k,n}$: relative weighting coefficient of the *k-th* eigenfunctions for the *n-th* analyzed object;

$I_{m,n}$: response of the *m-th* camera channel acquiring the *n-th* analyzed object.

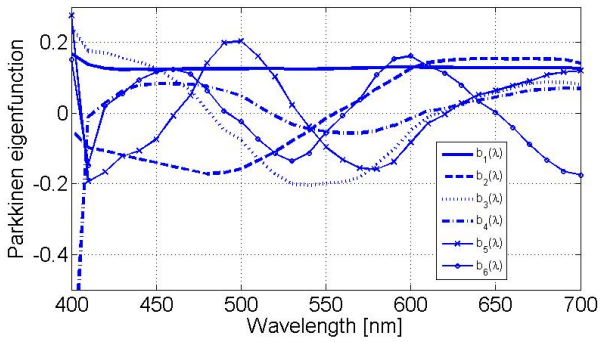

Figure 1.18 *First to sixth eigenfunctions found by Parkkinen through PCA and used as the basis for the reflectance spectra estimation in this Master Thesis work. The curves are sampled every 10 nm between 400 and 700 nm.*

Denoting with $s_n(\lambda)$ the spectral reflectance of an object, its approximation found through PCA can be expressed as:

$$s'_n(\lambda) = \sum_{k=1}^{K_s} \sigma_{k,n} \cdot b_k(\lambda) \tag{1.21}$$

where each $\sigma_{k,n}$ is the weighting coefficient for the *k-th* basis for the target object. These coefficients need to be calculated from experimental data as follow:

Consider an acquisition system characterized by M spectrally different acquisition channels. For each sampling channel m the number $I_{m,n}$ of photo-carriers generated by an object with a reflectance $s_n(\lambda)$ and illuminated by a light source $e(\lambda)$, can be expressed as:

$$I_{m,n}(\lambda) = \int e(\lambda) \cdot s_n(\lambda) \cdot c_m(\lambda) d\lambda \tag{1.22}$$

where the integral is taken over the visible spectrum and $c_m(\lambda)$ represents the spectral response of the *m-th* camera channel. Substituting Eq. 1.21 into Eq. 1.22 the following approximated formula can be written:

$$I_{m,n}(\lambda) \approx \int \sum_{k=1}^{K_s} \sigma_{k,n} \cdot b_k(\lambda) \cdot e(\lambda) \cdot c_m(\lambda) d\lambda = \sum_{k=1}^{K_s} \sigma_{k,n} \int b_k(\lambda) \cdot e(\lambda) \cdot c_m(\lambda) d\lambda \tag{1.23}$$

It is here assumed that the spectrum of the illuminant is known with good approximation. As a consequence, given a specific camera with known spectral responses and chosen a basis of eigenfunctions, the integral includes no unknowns,

and is thus a constant term, $f_{m,k}$. The equation above can be rewritten as:

$$I_{m,n}(\lambda) \approx \sum_{k=1}^{K_s} \sigma_{k,n} \cdot f_{m,k} \tag{1.24}$$

where the only unknowns are the weighting coefficients $\sigma_{k,n}$. Denoting with $\mathbf{I}_n$ the vector of the m camera responses $I_{m,n}$, with $\boldsymbol{\sigma}_n$ the vector of the k weighting coefficients, and with $\mathbf{F}$ the $m \cdot k$ matrix formed by the $f_{m,k}$ elements, we can write the equation above in a matrix form:

$$\mathbf{I}_n = \mathbf{F} \cdot \boldsymbol{\sigma}_n \tag{1.25}$$

The best solution can be found using the pseudo-inverse matrix $\mathbf{X} = (\mathbf{F}^T \cdot \mathbf{F})^{-1}\mathbf{F}^T$ as $\boldsymbol{\sigma}_n = \mathbf{X} \cdot \mathbf{I}_n$

In alternative to PCA, the authors of [23] also proposed the use of 7 optical filters with a similar shape an shifted one respect to the other to cover the whole visible spectrum. It can be seen as a spectral filtering followed by a sampling operation $\delta\lambda = 50nm$. This allows spectral reconstruction via interpolation schemes such as cubic-spline interpolation. This technique gave poorer result in respect to PCA.

Available Technology for Multi-spectral Imaging and the solution proposed in this Master's Thesis work will be discussed in Chapter 2.

1.3 Digital Color Imaging Today

Digital Still Cameras have gained importance in the last decades. Every new computer and mobile phone has integrated digital cameras, and both commercial and professional cameras are sold in great quantities all around the world. There is a continuous technological race to bring the newest and cheapest technology to market. In this section the digital imaging pipeline will be described, followed by a brief overview of the main technologies and solutions today available for digital color sensors. Their pro & cons will be discussed, in order to understand the potential advantages of the solution proposed in this Thesis.

1.3.1 The Digital Color Imaging Pipeline

Figure 1.19 shows the digital imaging pipeline. The image of the scene is focused on the sensor by a system of lenses which can be more or less complex depending on

the camera. In standard CMOS color imaging, a Color Filter Array (CFA, described later in this section) is interposed between the optical system and the sensor. The pixels forming the matrix of the sensor integrate light and give an electric output proportional to the incident light intensity at each point. The next step consists in color interpolation (or demosaicking), where raw data are converted into the RGB Device Dependent color space coordinates. Further signal processing is implemented before converting data into Device Indipendent color space coordinates by means of the CCM **B**. The image is then compressed and ready to be saved.

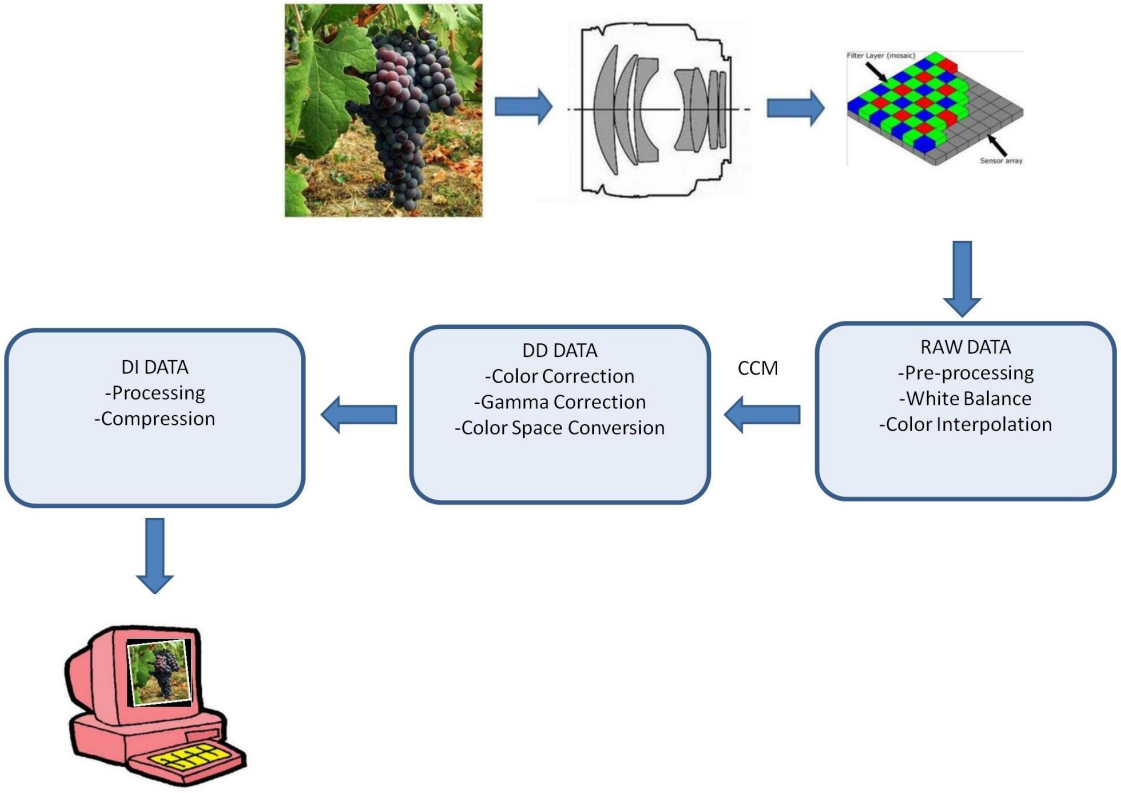

Figure 1.19 *Digital Imaging Pipeline*

1.3.2 Sensors for Digital Color Imaging

A solid state image sensor is a semiconductor device that converts an optical image that is formed by an imaging lens into an electronic signal. In quantum photodetectors this conversion is achieved through the creation of free electron-hole pairs by the absorption of photons (as described in section 1.1). To obtain an image, the scene must be spatially sampled, hence the image sensor is formed by a matrix of

photo-detectors, which need to be individually readout. Since light is integrated regardless to the incident wavelength, color information is usually obtained by placing a mosaic of tiny color filters on top of the sensor (called Color Filter Array). Pixel readout is typically performed in integration mode: the incident light generates charges (photo-charge) which are stored on the photodiode depletion capacitance; the integrated charge is then converted into an output voltage (before or during the readout, depending on the device). At the end of the readout phase, the voltage across the detector is reset to the starting conditions, and the camera is ready to acquire another image.

The main parameters to be considered for the evaluation of an image sensor are the Quantum Efficiency (QE), the Fill Factor (FF) and the Dynamic Range (DR). Quantum efficiency has already been defined in equation 1.10 and gives information about how many photons incident on the active area are converted into useful photo-charges. The quantum efficiency of Silicon solid state detectors is usually increased by adding anti-reflection coating at the surface of the sensor.

The Fill Factor is defined as the ratio between the active area and the overall sensor area

$$FF = \frac{A_{active}}{A_{tot}} \times 100[\%] \tag{1.26}$$

The higher the FF, the larger the electrical signal corresponding to the photon flux. Depending on the readout topology, larger or smaller FF can be obtained.

The Dynamic Range is defined as the ratio between the maximum and minimum detectable signals. The maximum detectable signal is the maximum amount of charge q_{max} (C) that causes pixel saturation:

$$q_{max} = Q_{s,max} - t_{int} I_{dark} \approx Q_{s,max} \tag{1.27}$$

where t_{int} is the integration time and $Q_{s,max}$ is the maximum charge that can be stored on the depletion capacitance C_{dep}. Being V_{reset} the voltage at which the capacitance is reset after each integration, $Q_{s,max}$ can be calculated as:

$$Q_{s,max} = V_{reset} \cdot C_{dep} \tag{1.28}$$

In the approximation it is assumed that for a well designed photodetector the maximum signal is much larger than the noise current. If we consider that the minimum acceptable Signal to Noise ratio is $(S/N) = 1$, then the minimum detectable

signal in terms of charge (C) is equal to the rms readout noise:

$$q_{min} = \sqrt{\sigma^2_{Q,noise}} \tag{1.29}$$

Thus the Dinamic Range can be calculated as:

$$DR = 20log_{10}\frac{Q_{max}}{\sqrt{\sigma^2{}_{Q,noise}}} \tag{1.30}$$

The main noise contributions are the shot noise of the dark and photo currents, the KTC noise (also called reset noise) and the Fixed Pattern Noise (FPN). The two main current contributions to shot noise are the photocurrent and the dark current. The latest is due to the collection at the anode of randomly thermal generated charges within the depletion region of the device. The rms contribution of the shot current in terms of charge current (A) over a band B can be calculated as:

$$\sqrt{\sigma^2_{Q,shot}} = \sqrt{2qi_{tot}B} = \sqrt{2q(i_{dark} + i_{ph})Bt_{int}{}^2} \tag{1.31}$$

During the calculation of the Dynamic Range, the shot noise of the signal is usually neglected. In fact, when evaluating the minimum detectable signal, we can suppose that the photogenerated current is much smaller than the dark current. In this specific case:

$$\sqrt{\sigma^2_{Q,shot}} \approx \sqrt{2qi_{dark}Bt_{int}{}^2} \tag{1.32}$$

KTC noise is related to fluctuations of the voltage across the device capacitance during the periodical reset. Hence the reset voltage is not constant over the different integrations, which results in output voltage uncertainty. Its rms noise contribution in terms of charge can be calculated as:

$$\sqrt{\sigma^2_{Q,reset}} = \sqrt{kTC_{dep}} \tag{1.33}$$

where k is the Boltzmann constant and T is the temperature in K. Fixed Pattern Noise is a general term to identify a temporally constant non uniformity among the pixels of an imaging systems. It is characterized by a fixed pattern of higher and lower output signals of the different pixels (also referred to as ”hot’ and ”cold” pixels) under the same illumination conditions. This phenomenon is due to the small difference in the individual responsivities of the photodetectors and of the

preamplification stages. The overall rms noise contribution in terms of charge can hence be expressed as:

$$\sigma^2_{Q,noise} = 2qi_{dark}t_{int} + kTC_{dep} + \sigma^2{}_{Q,FPN} \tag{1.34}$$

The cost of production is also a critical issue, and is one of the driving forces for the development of new technologies. Low cost, low power, and the enormous technological improvements in the direction of dedicated processes for optical applications, together with the possibility of producing Active Pixel Sensors, made the fortune of CMOS technology for digital imaging.

1.3.2.1 CMOS sensors: APS and PPS

CMOS sensors include a more or less elaborate photo-diode and one ore more transistors for the readout. The two main readout topologies are the Passive Pixel Sensor (PPS) and the Active Pixel Sensor (APS)

In PPS each pixel is simply connected to rows and columns by means of select switches (e.g. a MOS transistor). In this configuration, a row- and column-selecting multiplexer sequentially scan the matrix, connecting each pixel to a single readout electronics, designed aside of the matrix of photo-diodes. It is called Passive Pixel Sensor (PPS) since for each pixel there is no function other than photons collection and conversion into electron-hole pairs. This structure has a really large active area, thus the FF approaches 100%. PPS were used for CCD, for which no integrated electroncis could be implemented.

In CMOS sensors, Active Pixels can be implemented. In this second readout solution, the signal is amplified at pixel level and every element can be individually addressed. Figure 1.20(a) shows the schematic of a typical 3 transistors APS. The working principle of active pixels is as follows:

After each integration the reset transistor resets the anode voltage to

$$V_{ref} - V_T \approx V_{ref} \tag{1.35}$$

Where V_T is the threshold voltage of the reset transistor. The light is then integrated on the depletion capacitance of the device, so that:

$$\Delta V_{anode} = \frac{(i_{ph} + i_d)t_{int}}{C_{dep}} \tag{1.36}$$

Finally, the follower transistor is biased through the closure of the switch transistor RS so that the voltage at the follower gate is transferred to the pixel output. This AP topology has two main advantages: the pre-amplification lowers problems related to the large parasitic capacitances of the connections to the external amplifier, while the individual pixel addressing leads to a faster readout. On the other hand, the charge to voltage conversion is made on the sensor capacitance, whose value can't be precisely controlled, and is voltage dependent. Thus the integration is not completely linear and the amplification gain is not well defined.

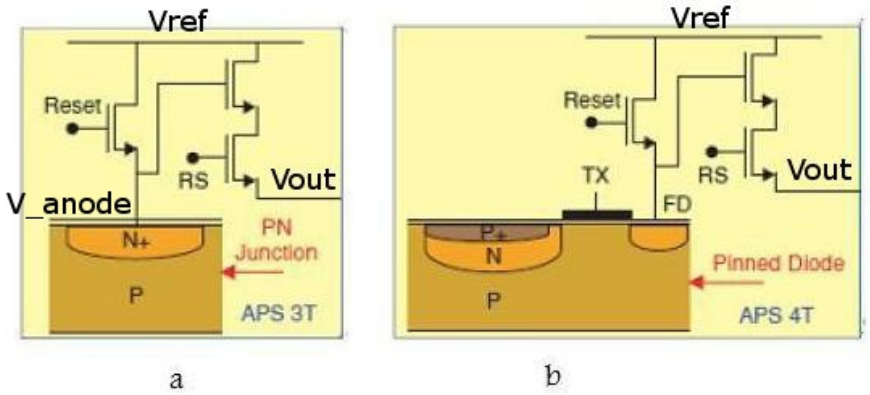

Figure 1.20 *A schematic of a 3T (a) and 4T (b) active pixel sensor*

A possible solution to this problem is given by the 4 transistors topology shown in figure 1.20(b) ([28]): where photocharges are is generated and collected in a pinned photodiode floating diffusion. The transfer gate TX, when activated high, transfers the charge from the pinned region to a sense node. The pinned region is fully depleted of majority carriers without an n+ connecting region, hence complete charge transfer is possible. For this configuration, like for 3T Active Pixels, signal pre-amplification is performed at pixel level. but it has the advantage of using an integration capacitance which is not signal dependent. Furthermore the pinning shallow P-type implant has also a positive effect on the dark current with respect to standard photo-diodes. In fact, the surface generated charges are no more within the N-type region and typically recombine before reaching it. Hence the surface generated current can be almost neglected, decreasing the overall dark current. However, the pinned diode pixel has a higher cost with respect to standard photodiodes, since it requires dedicated technological processes, as two custom implants are needed to establish the diode's potential so that charge coupling can take place. APS have a lower FF respect to PPS, but this problem is partially solved by introducing micro-

lenses that increase the light collection efficiency by focusing light on a smaller area (figure 1.21). CMOS APS are widely used for commercial cameras since standard CMOS is a really mature and low cost technology.

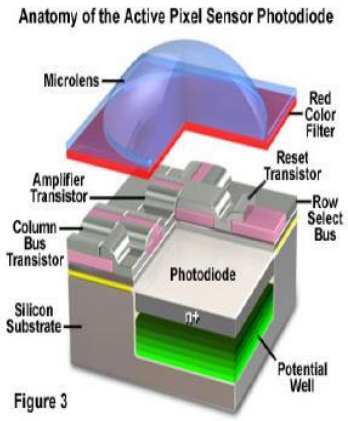

Figure 1.21 *DCanon reduced gap microlenses*

1.3.3 Color Filter Arrays

Photodiodes integrate light from the whole visible spectrum, without selecting any specific wavelength range. Hence filters (or equivalent filters solutions) must be introduced to reconstruct color information. As discussed in previous sections, color sensors mimic the trichromatic behavior of the human eye. Hence color images are obtained by using three (or sometimes more) different sensitivities to sample the scene spectral properties, attributing to each image point its color coordinates in the device native color space. From this coordinates, Device Independent color coordinates are then estimated with a linear transformation by means of a Color Conversion Matrix.

The most widespread technology for digital color imaging are Color Filter Arrays (CFA). The idea is to interpose between the micro-lens and the photo-diode a color filter with a specific spectral transmittance. Thus the light incident on each pixel will have a spectrum which is the product of the incident light spectrum and the filter spectral transmittance corresponding to $c_m(\lambda)$ in eq 1.22. A color image requires at least three colors information at each pixel location: digital images often use red (R), green (G), and blue (B). Hence a camera would need three separate sensors to completely measure the chromatic properties of the scene. This is the case for

three-chips color cameras, where the light entering the camera is split and projected on three sensors, each cover with a filter with a different spectral transmittance (red, green and blue filters in the example in figure 1.22). Each sensor requires its proper driving electronics, and has to be registered precisely. These additional requirements add a large expense to the system.

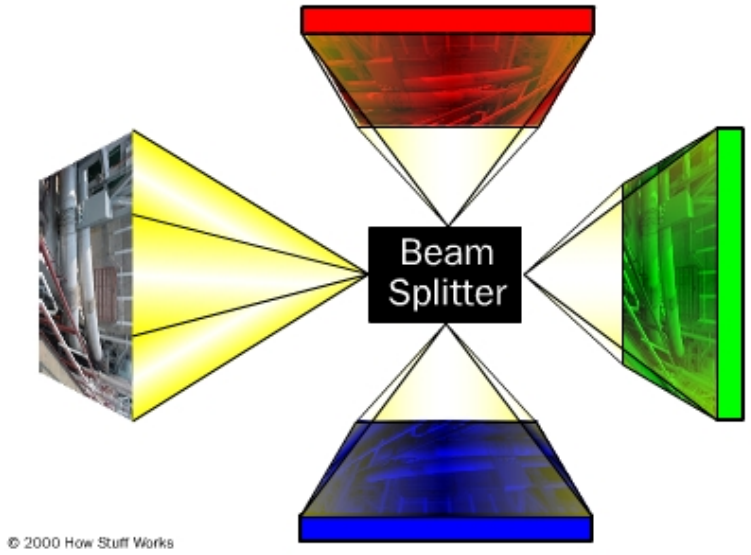

Figure 1.22 *3 Detector Color Imaging: Light is splited on three separate sensors to obtain colored images without demosaicing*

Many cameras exploit human eye spatial resolution limits by using a single sensor covered with a Color Filter Array (CFA). The CFA allows only one color to be measured at each pixel; this means that the camera must estimate the missing two color values at each pixel. This estimation process is known as demosaicing [29]. Many CFA patterns can be used, but the most common is the Bayer Filter Array shown in figure 1.23, where red, green and blue filters are used. Green is sampled twice respect to the other two, since the human eye sensitivity has a peak in the middle wavelengths (around 555nm).

The problem of demosaicing is a typical interpolation problem, hence standard interpolation techniques can be used. The more elaborate the technique, the better the result and the higher the computational cost. Simple techniques treat the three signals as uncorrelated signals, while more advanced algorithms take into account the high correlation between the three colored images. For a survey of the main demosaicing algorithms, together with their pro & cons refer to [30].

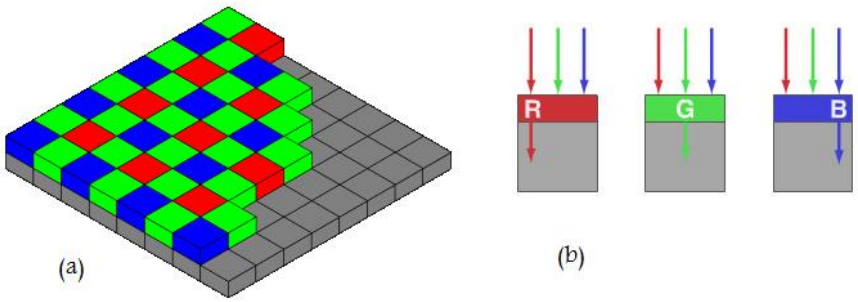

Figure 1.23 *Bayer Pattern Color Filter Array: (a) Bayer Pattern; (b) CFA working principle*

1.3.4 Toward Filter-less and Tunable Color Imaging Devices: The Foveon and the TFA

Regardless of the complexity and the goodness of the interpolation algorithm, CFAs lower the signal (since only less than one third of the light is transmitted) and have a reduced color resolution with respect to a three sensors system (due to interpolation). Furthermore CFAs require additional dedicated processes steps , and once the color pattern has been defined, the sensitivity of the color channels is fixed. For these reasons, more and more effort is being put in the development of standard CMOS filter-less color sensor. This section will describe two devices which tried to answer these problematics: the first is the filter-less color sensor Foveon X3, while the second device is called TFA, and is one of the few examples of color sensors with an electrically tunable sensitivity. Both sensors are based on the dependence of the absorption coefficient from the wavelength.

1.3.4.1 The Foveon X3

Foveon X3 has been developed in 2002 by the image sensor producer Foveon Inc. It is a direct color image sensor, which means that it directly captures red, green, and blue light at each point of the image during a single exposure. Its working principle is the same as the one used to realize color images on film, where three emulsion layers are used to separately capture red, green and blue light, obtaining full color information for each point of the image. In the Foveon X3 the trichromatic information is obtained by separating charges photogenerated at different depths. In fact, as it has been introduced at the beginning of this chapter, silicon absorption

coefficient strongly depends on the wavelength of the incident light, thus the higher energy photons (at the blue end of the spectrum) are absorbed at the surface, whereas the lower energy photons penetrate deeper into the silicon substrate before being absorbed. Three separate PN junctions are buried at different depths inside the silicon surface and used to separate the electron-hole pairs. The three junctions are reversely biased with three separated anodes, generating three different depletion regions: depending on the wavelength, photons are absorbed at different depths, generating photocharges which will be collected at a different anode. The depths of these junctions are the key variables that determine the spectral sensitivities of such a device [1].

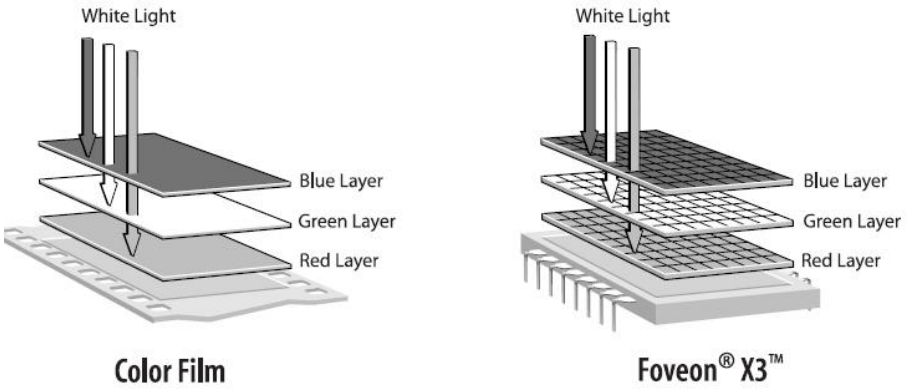

Figure 1.24 *Foveon X3 technology achieved for solid-state sensors what Kodachrome did for color film in 1935 [1]*

.

Figure 1.25 shows the structure of a three stacked layers silicon sensor based on a triple well CMOS standard technology. During the design, the thickness of the stacked junctions has been defined in function of the required sensitivities (within technological limits). Figure 1.26 shows the obtained sensitivities presented in [1].

This sensor has two main advantages with respect to mosaic sensors: the signal is not lowered by filters' transmittance and no demosaicing algorithms are required, since each pixel is alone-standing. As a consequences images have a better resolution and a better color reproduction, strongly reducing color artifacts (figure 1.27).

However this sensor also has some limitations. Dark current cannot be reduced by using a pinned diode, hence the increasing in signal is matched with an increasing in noise. Furthermore, once the technology has been set, the sensor sensitivity is defined too, and no more than three color channels can be obtained, since three is

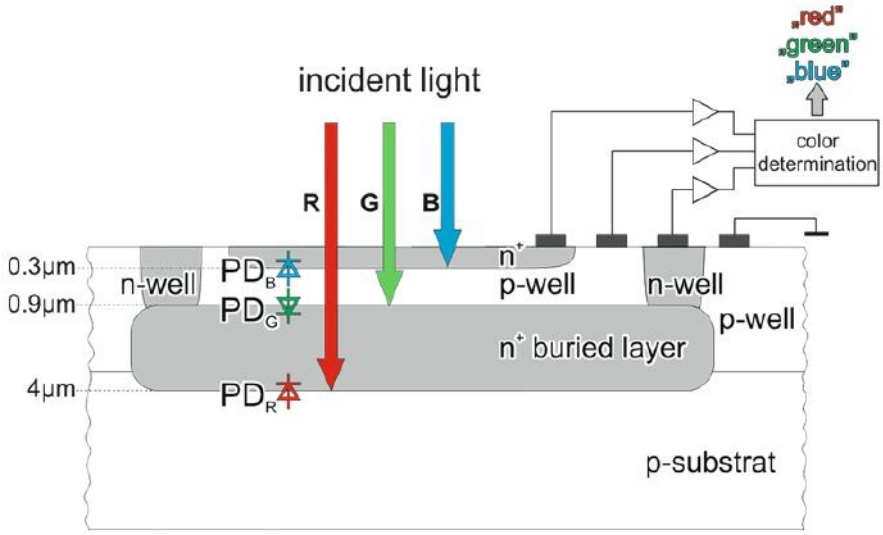

Figure 1.25 *A schematic drawing of a sensor stack that captures all of the incident photons, filtering the color components by the wavelength-dependent absorption of silicon. [1]*

the maximum number of wells available in standard CMOS technology.

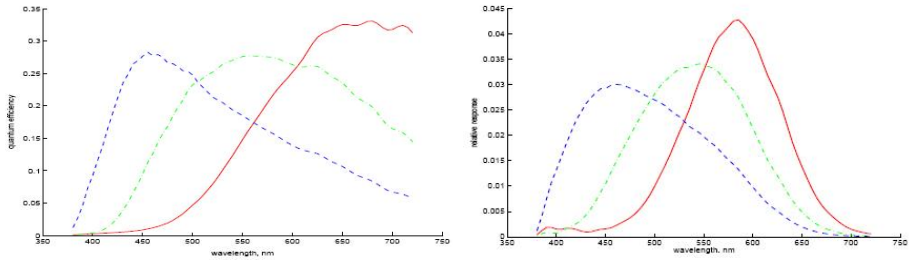

Figure 1.26 *Wavelength vs Spectral Sensitivity of a Foveon X3 Sensor with (right) and without (left) a 2 mm cm500 IR filter [1].*

1.3.4.2 The TFA

The TFA (Thin Film on ASIC), described in [2], is a color sensor with an electrically tunable spectral sensitivity. The device is a a-Si:H pi^3n type diode with a heterogeneous structure (figure 1.28), where the thickness and optical properties of the individual layers are adjusted to obtain an optimized generation profile.

Since the band gap decreases and the dielectric constant increases from the front to bottom i-layer, the electric field distribution is inhomogeneous [2]. Depending on the bias, the high electric field (where photogenerated EHP are collected) extends to

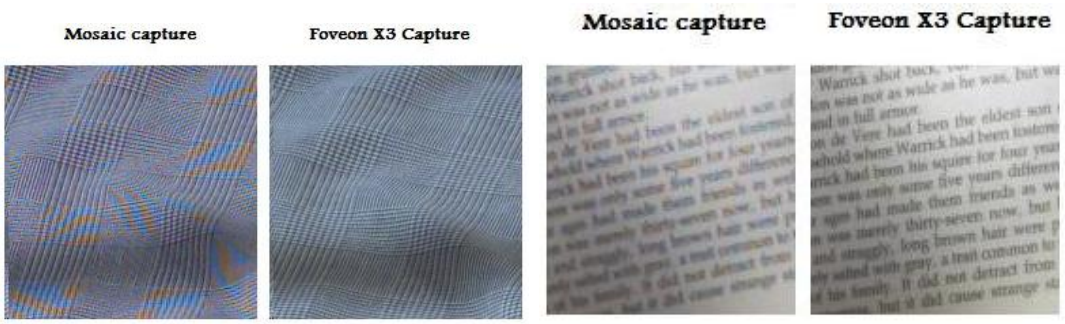

Figure 1.27 *Comparison between the images obtained with a Foveon X3 and a mosaic sensor of the same size. The figure on the right shows the reduction of color artifacts, while the figure on the left shows the improvement in resolution.*

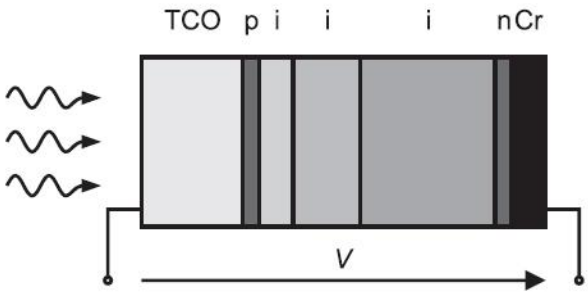

Figure 1.28 *Schematic layer sequence of an a-Si:H based pi3n three color detector.[2]*

a different depth from the surface, thus by switching the reverse bias between three different voltages, a trichromatic operation is obtained. This device bases its working principle on the correlation between the wavelength and the absorption depth like the Foveon X3, but is has the big advantages of having an electrically tunable color space. The left image of figure 1.29 shows the spectral response at three different reverse bias. Since the photo-current at -5V is due to both "red","green" and "blue" photons, the one at -2V to "green" and "blue" photons and the one at 0V only to "blue" photons, the RGB response (left image in figure 1.29) is obtained with decoupling the three mixed color signals with a linear transformation. The device showed bad linearity, hence the matrix for the conversion from the photo-currents to the RGB curves is different depending on the light intensity. This device is really innovative from may points of view, though is not implemented in standard CMOS technology, and the trichromatic signal needs three different acquisitions, resulting in high technological cost and reduced speed. The authors didn't present any data concerning the range of tunability of the sensor.

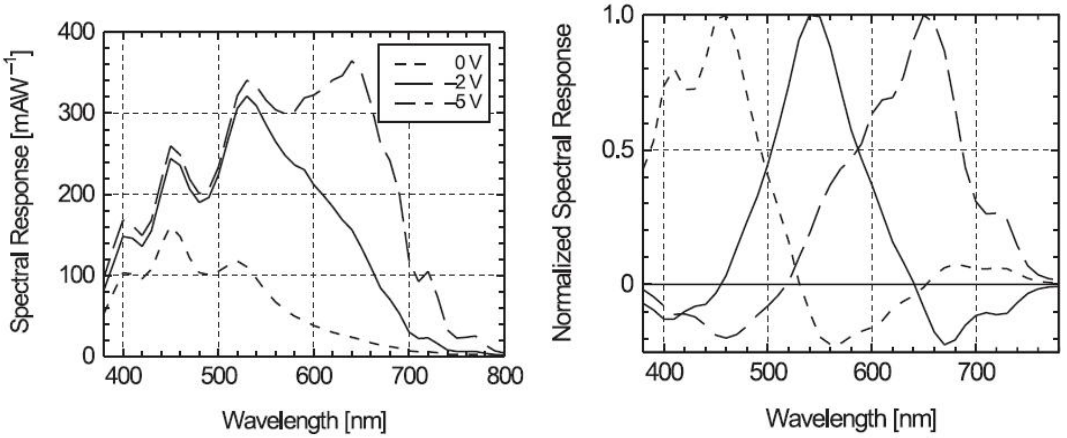

Figure 1.29 *Voltage dependent spectral response curves of the optimized pi^{3}n trichromatic sensor (left) and normalized spectral response curves including an optimized linear color correction (right) [2].*

Chapter 2

A Tunable Sensor:The Transverse Field Detector (TFD)

The Transverse Field Detector (TFD) is an innovative color sensitive pixel that incorporates both the advantages of the Foveon X3 and the TFA: it is a filterless, standard CMOS, electrically tunable color detector. With a single sensor, both standard RGB imaging and additional features such as High Color Accuracy Imaging and Multi-spectral Imaging can be implemented, hence it is in-line with the trend of these last years toward "smart" pixels, which can integrate different functionalities. During this work the detector has been first simulated and then implemented to target new applications. This chapter will focus on the working principle of the device and on the design flow for its optimization in terms of color performance, Fill Factor and tunability.

2.1 TFD Working Principle

The TFD bases its working principle on the idea of separating colors within a single acquisition by exploiting the physical law that describes the absorption of photons in Silicon within the visible spectrum. Figure 2.1 represents a simplified scheme of the device working principle.

A single depletion region with a diagonal electric field profile is generated by superimposing to the depletion electric field, perpendicular to the surface, a horizontal electric field, engendered by a suitable biasing scheme of surface anodes. The photogenerated charges will drift perpendicularly to the iso-potential lines toward

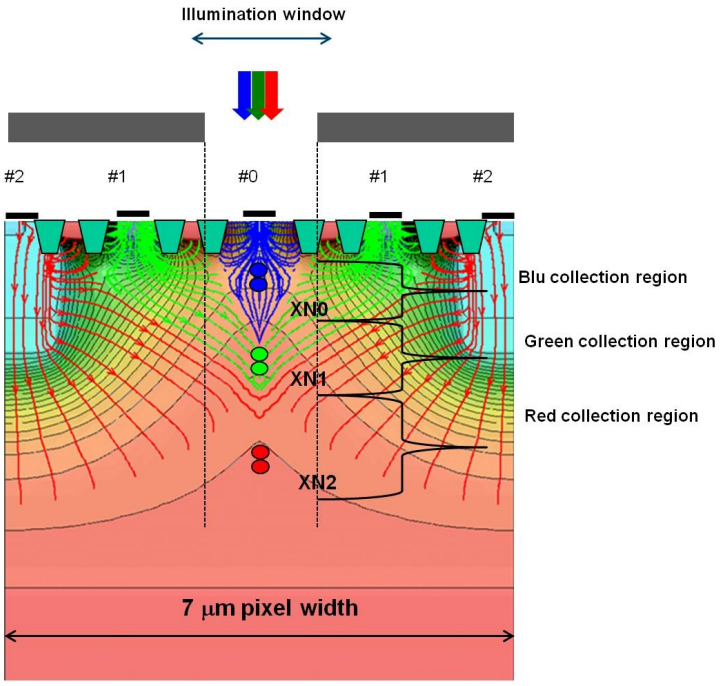

Figure 2.1 *TFD working principle: color separation is obtained by means of transverse electric fields.[3]*

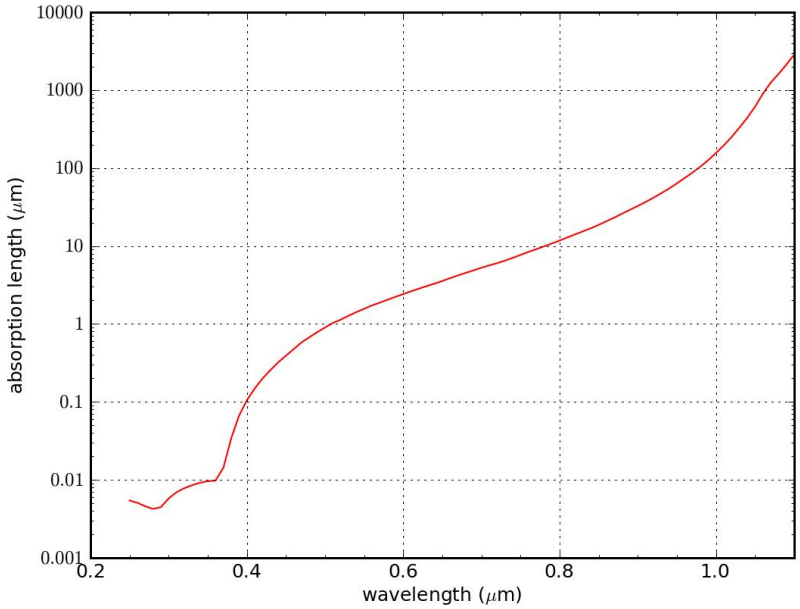

Figure 2.2 *Wavelength dependence of the Silicon absorption length*

a different anode, depending on the absorption depth of the photon. Under the simplified hypothesis that the light beam is concentrated in the central region of the device, neglecting surface reflections and photons absorption in undepleted regions, the quantum efficiency of the three color channels can be calculated as:

$$\begin{aligned} QE_{N0}(\lambda) &= 1 - exp^{-\frac{x_{N0}}{L_{abs}(\lambda)}} \\ QE_{N1}(\lambda) &= exp^{-\frac{x_{N0}}{L_{abs}(\lambda)}} - exp^{-\frac{x_{N1}}{L_{abs}(\lambda)}} \\ QE_{N2}(\lambda) &= exp^{-\frac{x_{N1}}{L_{abs}(\lambda)}} - exp^{-\frac{x_{N2}}{L_{abs}(\lambda)}} \end{aligned} \tag{2.1}$$

Where x_{N0}, x_{N1} and x_{N2} are the avarage depths that delimit the collecting region of each anode. Figure 2.2 shows the wavelength dependence of the silicon absorption length (inverse of the absorption coefficient). Blue photons are absorbed within the first hundreds nanometers, hence for $x_{N0} \approx 100nm - 500nm$ all the corresponding photogenerated charges will be dragged by the electric field toward N_0. The absorption length of photons with wavelength around 500-600nm (green photons) is $1\mu m - 1.5\mu m$, hence by applying a suitable biasing scheme, the depth x_{N1} can be set so that the majority of the charges photogenerated by green photons are collected by anode N_1. For the same principle the charges photogenerated by red photons will drift toward N_2. Part of the red photons are absorbed outside of the depletion region, but most of the photogenerated charges diffuse until the border of the depletion region and then drift toward N_2. The same working principle can be obtained using an asymmetrical structure, which will be described in the next section.

In this simplified explanation it has been supposed that the light beam is concentrated in the central region of the device. In practice, the width of the incoming light beam is set by an optical window, as shown in figure 2.1, and the anodes don't have a well defined collection depth, but more a collection region, in which the electric field stream lines drag photons toward a specific anode. As it will be discussed later in this chapter, the illumination window must be carefully chosen by finding a good trade-off between an acceptable fill factor, well balanced and non-overlapped spectral sensitivities and good spectral tunability.

2.1.1 Advantages and Disadvantages of the TFD compared with other color sensors

This device shares with the Foveon X3 the advantage, with respect to CFA sensors, of being a direct sensor: this means that no demosaicing algorithm is required, avoiding the related color artifacts. Furthermore since no filters are added on top of the sensor, a higher quantum efficiency is obtained.

As described in the previous paragraph, the quantum efficiency of each color channel depends on their collection region. The electric field profile, and hence the anodes collection region can be changed by applying a different biasing scheme. Thus the device has an electrically tunable spectral sensitivity. Figure 2.3 shows an example of two different electric field profiles that can be obtained by changing the anodes voltages. The TFD can be designed to have more than three color channels, which can be useful to improve color reconstruction or to use Infra Red Information.

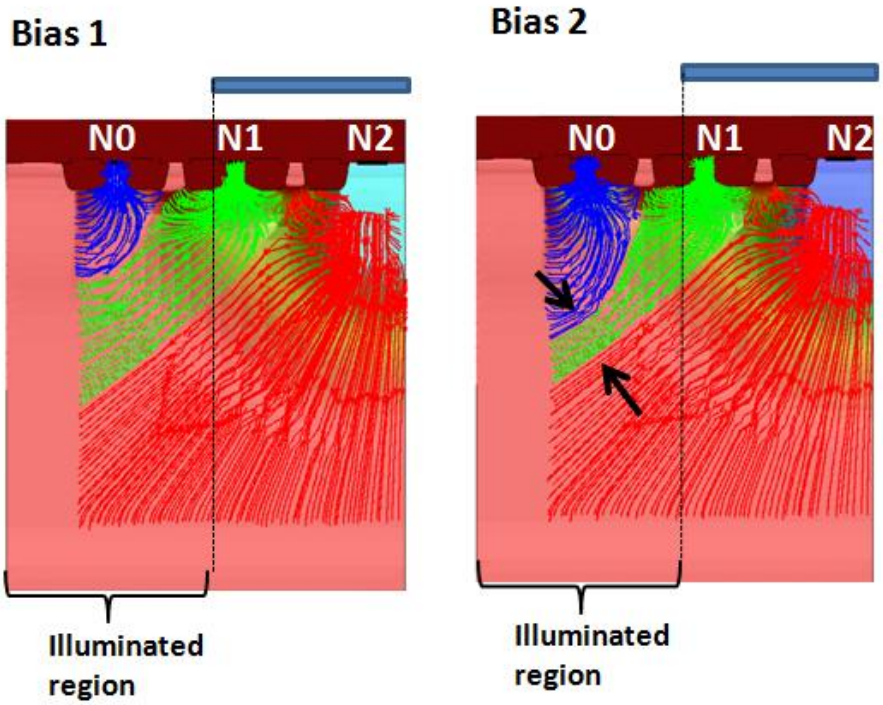

Figure 2.3 *Example of two electric field profiles that can be obtained by changing the biasing conditions*

There are also some limitations with respect to CFA sensors. First of all, standard APS readout electronics cannot be used, since for the correct operation of the

device the electric potential of the surface anodes must be constant during the integretion. Hence new readout schemes must be implemented. Moreover, as it will be shown later, the obtained spectral sensitivities are never as sharp as the ones obtained with color filters, and present overlap, which can be an issue during color conversion.

2.1.2 Technological Requirements

From a technological point of view, the TFD can be implemented in standard CMOS technology. Referring again to figure 2.2 a depleted region of $3\mu m$ is sufficient for a good functioning of the device. Under the hypothesis of a unilateral junction, the width of the depletetion region can be calculated as:

$$W_{dep} = \sqrt{\frac{2\epsilon_{Si}(V_{bi} + V_{rev})}{qN_a}} \tag{2.2}$$

Hence, for a 10V reverse bias, the substrate doping to obtain a $3\mu m$ wide depleted region is:

$$N_a = \frac{2\epsilon_{Si}(V_{bi} + V_{rev})}{q{W_{dep}}^2} \approx \frac{2 \cdot 1.03594 \cdot 10^{-12} F/cm \cdot 10V}{1.6 \cdot 10^{-19} C \cdot (3\mu m)^2} \approx 1.5 \cdot 10^{15} cm^{-3} \tag{2.3}$$

A further technological requirement is the possibility to implement an efficient isolation between the anode, to avoid punch-trough leakage current to flow between the electrodes. Both requirements can be met by standard CMOS technology, making the TFD possibly competitive with standard CMOS sensors.

Three runs were previously done on this sensor, during which the technological feasibility has been tested and device working principle has been demonstrated. Different geometries have already been implemented. The run corresponding to this work started in September 2010, and, for the first time, working active and passive mini-matrices, together with more complex readout circuits, have been implemented, putting the basis for the development of a future full TFD sensor.

2.2 Tunable Sensors: Digital Color Imaging Tomorrow?

Before starting to describe the sensor design flow, a few words are here spent on the concept of tunability of a color sensor, and how this feature can be utilized to create a "smart" pixel, able to adapt to the scene and to integrate different functionalities.

As it has been introduced in the first Chapter, each color sensor is characterized by three (or rarely more) color channels, which integrate light, each one with its spectral sensitivity. Since each sensor has its own color space, the Device Dependent color information must be transformed into a Device Independent color information, that can be processed and displayed. For example the color coordinates can be transformed into CIE 1931 XYZ color coordinates by means of a linear transformation (a non linear transformation would request a far too high computational cost) with a Color Conversion Matrix. Since physical sensors color spaces can't respect the Luther-Ives condition, reconstruction errors are introduced during the linear transformation. The CCM is usually found by minimizing the color reconstruction error on a finite set of colors (such as the Macbeth Color Checker in figure 1.17). In Color Filter Arrays, the spectral sensitivity, and hence the CCM, are fixed, regardless of the scene chromaticity content. On the contrary, the TFD color space can be electrically tuned and adapted to the colors present in the scene. In [4] the authors identified and demonstrated two simple applications of the TFD that couldn't be implemented in standard sensors: intentional enhancement or decrease of color saturation without reducing the overall quantum efficiency, and White Balance (adaptation to the illuminant) by tunable spectral responsivities. An example of the first application is presented in figure 2.4, which shows a scene acquisition simulated using two experimental TFD set of responses obtained at two different tunings and the same CCM.

The sensors developed in this work were designed to target two other innovative applications of the device tunability: High Color Accuracy Imaging and Multispectral Imaging. Both applications are based on the possibility of using more than three spectral sensitivities with a single sensor. In CFA this requires a 4 to 6 colors Bayer pattern (or other more complex systems), while with the TFD it can be simply implemented either by adding additional electrodes to the structure (4-5 colors TFD), or by rapidly capturing more images with a different set of spectral

sensitivities. In both cases the QE is not reduced and no demosaicing algorithms are required.

2.2.1 Two Promising Applications of the TFD: HCA Imaging and Multi-Spectral Analysis

2.2.1.1 High Color Accuracy Imaging

In many industrial and scientific applications, such as cultural heritage, computer graphics and the textile industry, an accurate color reconstruction is required. By introducing additional colors channels, redundant data can be used to reduce the color reconstruction error introduced during the linear transformation from the sensor native color space to the DI color space, obtaining a higher color accuracy. This concept has already been used in CFA with 4 colors [31]: in this case better color reconstruction is obtained at the expenses of color resolution, since more complex demosaicing algorithms are required. Instead of increasing the number of fixed color channels, High Color Accuracy can be implemented by sequentially acquiring the same scene with different sets of spectral sensitivities. The larger the number of consecutive shots, the better is the approximation of the standard observer responses that can be obtained using a linear conversion algorithm. With CFAs this last approach can't be implemented, since physical filters have fixed spectral properties.

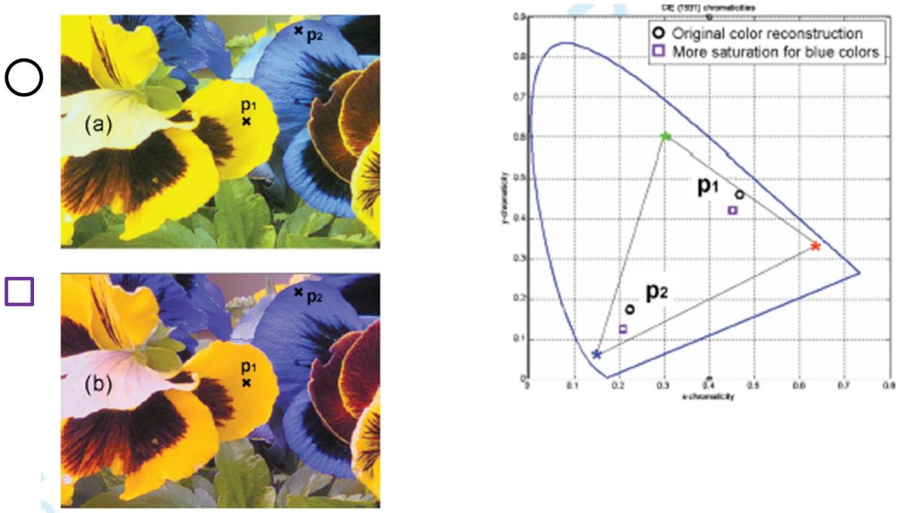

Figure 2.4 *Scene acquisition simulated using two experimental TFD set of responses obtained at two different tunings and the same CCM. [4]*

The TFD color space, on the contrary, can be electrically re-tuned, thus a single sensor is sufficient to implement more than three channels.

2.2.1.2 Multi-spectral Imaging

While color science requires only three color channels to calculate the color coordinates of an image point, this is not sufficient to evaluate the scene spectral reflectance. Two main approaches can be chosen to recover the spectral information of the incident light. The first solves the problem by increasing the number of samples: this technique gives really accurate results but requires expensive instrumentation and long a acquisition time. Hence it is not suitable for moving scenes or objects. This can be a limitation if for example one requires to measure the spectral reflectance of items on a production line (i.e. for quality control purposes). The second approach exploit Principal Components Analysis, by using the correlation in the data to scale the dimensionality. The spectral reflectance can be estimated with PCA as in equation 1.25, where $\boldsymbol{\sigma_k}$ is the vector of the weighting coefficient of the Parkkinen bases shown in figure 1.18. If we use the Macbeth Color Checker as set of spectral reflectances, previous works have shown that 6 eigenfunctions are sufficient for a good spectral estimation ([25] [24]). Figure 2.5 shows the simulation of the reconstruction of the spectral reflectance of the MCC with 5 color channel responses of a TFD, as presented in [22].

It is not a trivial problem to create a system, capable of acquiring the image with 6 different and linearly indipendent spectral sensitivities, which is at the same time simple, compact and cheap. In literature many different techniques have been proposed: in 1993 K. Martinez used 6 external filters to acquire multiband information of art paintings at the London National Gallery for digital archiving [32]. In 1999 F. Imai and R. S. Berns proposed the subsequent use of seven different filters in front of a BW camera [23] and alternatively the use of an RGB camera [33] making only three consecutive shots (camera uncovered, use of a light blue filter, use of a light green filter). M. Parmar from Stanford University proposed the acquisition of multiple images using a BW camera and different spectral illuminants. Park and Nayar proposed in 2007 the acquisition of two images only using an RGB camera and two suitably generated illuminants[34]. Yasuma in 2010 proposed the use of a CFA with seven different transmittances [35] [22].

It appears clear why the TFD seems so promising for multi-spectral applications:

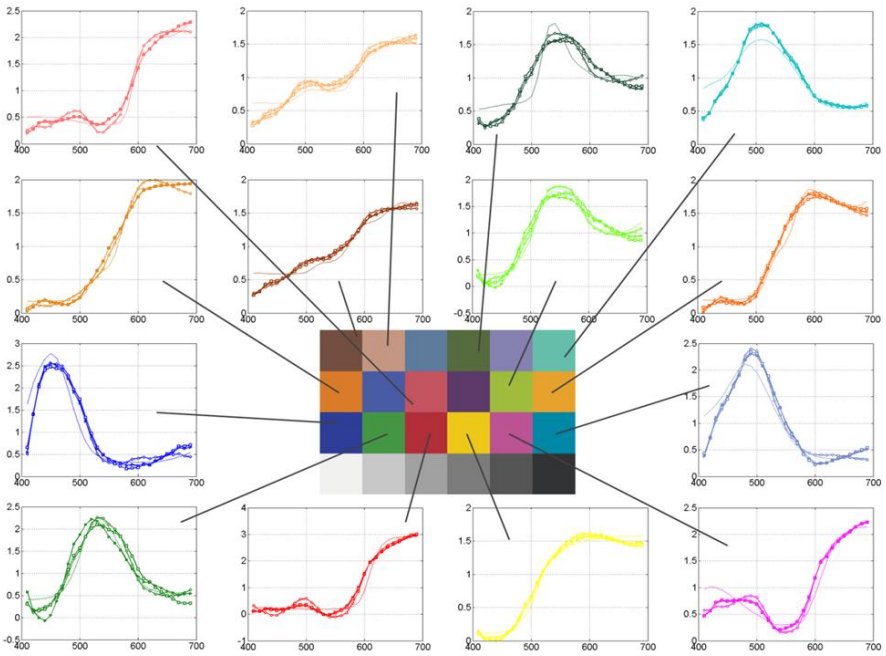

Figure 2.5 *scene acquisition simulated using two experimental TFD set of responses obtained at two different tunings and the same CCM. Comparison between some true reflectance of the MCC (light curves, data taken from the ISET software) and the estimated spectra using the algorithm presented in section 1.2.6.1. All spectral responses are normalized to their peak value [4].*

it is simple, inexpensive and compact. Furthermore the same device can be used for standard RGB imaging and spectral reflectance estimation.

In the following section the geometrical design will be described: the focus has been on maximizing the sensor spectral tunability range, which is necessary both for HCA and multi-spectral imaging.

2.3 The TFD geometrical Design

In this run the device has been implemented in LF150 technology which is a modular $15nm$ RF CMOS process, with up to 6 levels of Al plus thick metal, polymide passivation and $3\mu m$ thick lowly doped ($\approx 1.6 \cdot 10^{15} cm^{-3}$) P-type epitaxial layer, triple well and I/0 voltages of 1.8 V, 3.3 V and 5.0 V. Only 1.8 V core transistors have been used because pf their reduced size. No optical feature (microlenses, antireflection coating ...) was available at the time of the design.

The basic structure and doping profile of a symmetrical 3 color TFD pixel is shown in the left image in figure 2.6. The right image shows the electric potential profile for typical biasing conditions. The black lines represent the electric field streamlines, which are perpendicular to the iso-potential lines. The Finite Element simulations of the device have been implemented with ISE-TCAD Dessis electron device simulator, respecting all the design rules of LF150 technology.

The 5 anodes, which are used both to bias the device and to collect photo-charges, are realized by means of $n+$ implants/n-type wells on a low doped p-type epitaxial layer with $N_a \approx 1.6 \cdot 10^{15}\ cm^{-3}$. There are 5 implants (in red): the three central $n+$ implants have a peak doping of $N_d \approx 3 \cdot 10^{20}\ cm^{-3}$ at $0.3\mu m - 0.4\mu m$ depth; while the two external contacts are realized with n+ implants on deeper ($1\mu m$-$1.5\mu m$) n-type wells, with a peak doping of $N_{d_{Well}} \approx 2 \cdot 10^{17}\ cm^{-3}$. The central anode N_0 collects the carriers photo-generated close to the surface, the two N_1 anodes collect the ones photo-generated at an intermediate depth, while the external anodes N_2 collect photo-charges created by low energy photons, which are absorbed deeper in the device. For this reason N_0, N_1 and N_2 are referred to as "blue", "green" and "red" channels respectively. The choice of using n-wells for the external anodes is due to the fact that they can collect deep red photo-charges both by drift and diffusion, and they guarantee a better electric field profile for color-separation at lower voltages with respect to a device with only n+ implants. In the simulation

the epitaxial layer and the substrate are represented with an equivalent "active" layer, which is the equivalent collecting region estimated from the technological information provided by the foundry. The n-type implants are isolated one from the other with p+ implants (in blue) and Shallow Trench Isolations (STIs). Since the goal of this run was to test the technology in order to implement new TFD structures and new read-out topologies, and not to realize really scaled pixels, the device hasn't been designed with minimum dimensions to avoid problems related to technological parameter fluctuations: the $p+$ and $n+$ implants are 350nm wide, while STIs are 390nm wide.

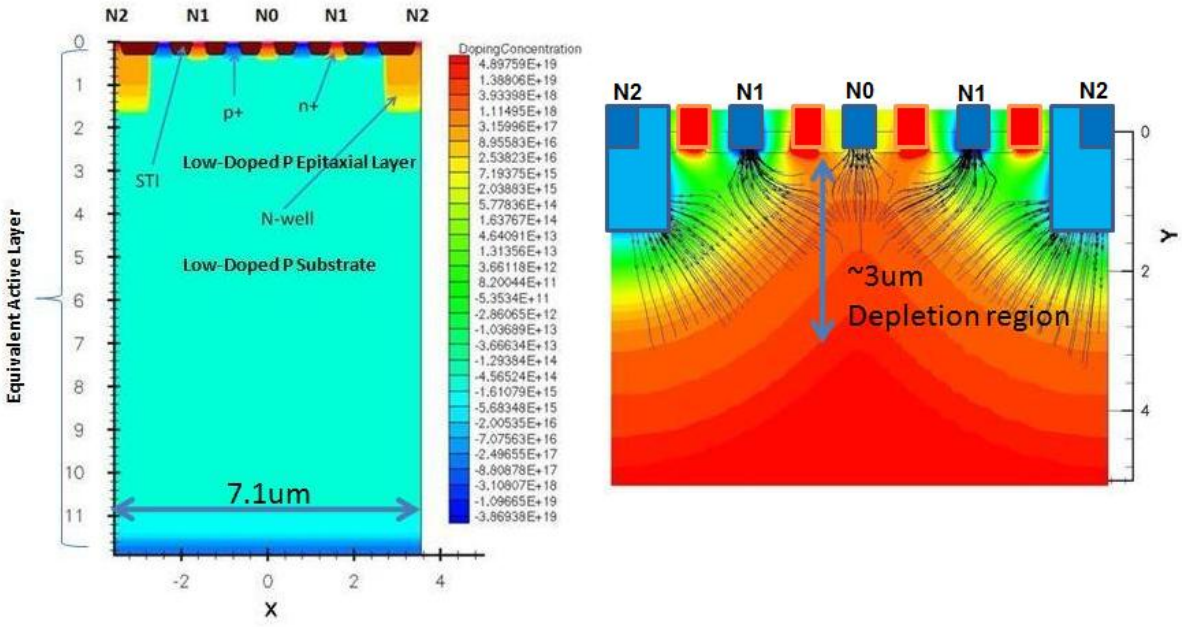

Figure 2.6 *Symmetrical 3 colors TFD: doping concentration profile (left) and conduction band energy profile for typical biasing conditions with electric field lines (right). The depleted region is on avarage* $3\mu m$ *deep. Because of the carrier life time in the p-type epitaxial layer and in the substrate, an equivalent carrier collection region of* $10\mu m$ *to* $12\mu m$ *is here simulated.*

Figure 2.7 represents the structure of an asymmetrical TFD. Only three implants are used and the pixel is closed with a deep p-well. In this alternative pixel geometry, diagonal collection trajectories can still be obtained by applying a suitable biasing scheme. This structure has the advantage of being smaller and of having a potentially higher fill factor than the symmetrical pixel. It has not yet been investigated if more than three color channels can be implemented.

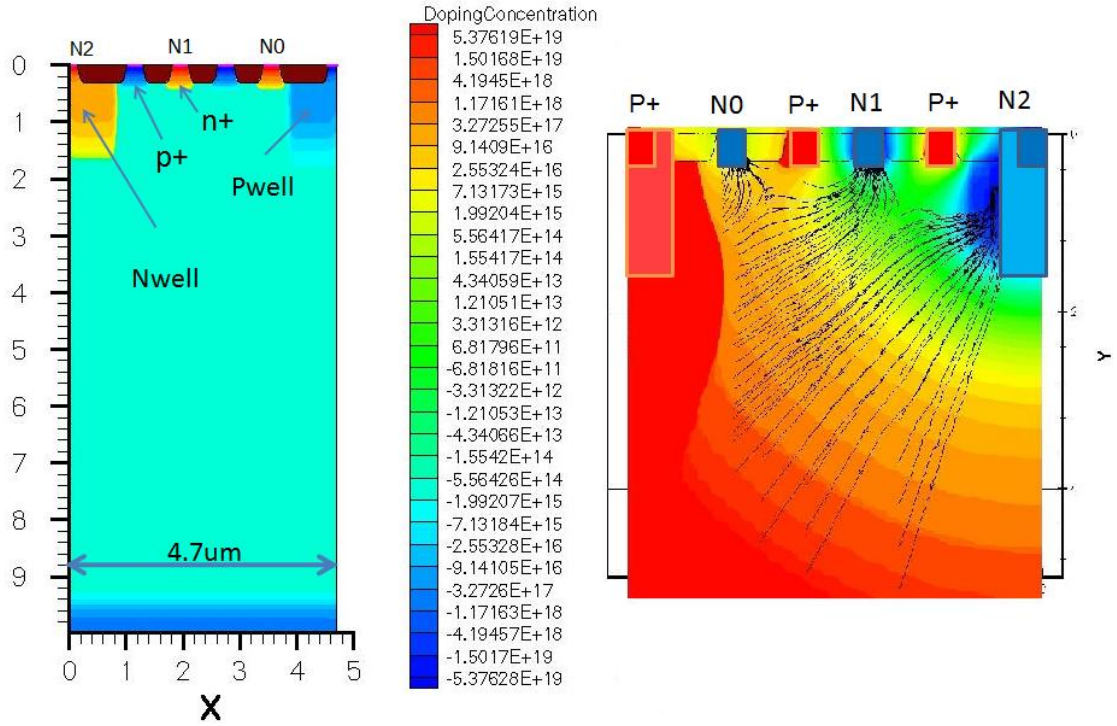

Figure 2.7 *Asymmetrical 3 colors TFD: doping concentration profile (left) and conduction band energy profile with electric field lines for typical biasing conditions (right).*

2.3.0.3 LF150 Technology Characterization: Breakdown, Punch-trough and Anodes Isolation Solutions

During the previous run, isolation problems between adjacent pixels in mini-matrices were found. For this reason and because this was the first time LF150 technology was used, much effort has been put in verifying the breakdown voltage and the biasing conditions which lead to current punch-trough between $n+$ implants or band-to-band tunneling in highly doped p-n junctions. The structure on which non ideal behaviors have been simulated is represented in figure 2.8, which corresponds to the solution proposed in [36] for the isolation between highly doped implants, here implemented in LF150 technology. For these first simulations approximated rectangular STIs have been used.

The fist simulation consisted in increasing the voltage difference between anodes N_A and N_B, with N_B kept at 0V (same potential as the active layer). The resulting currents at the two anodes are represented in right image of figure 2.9: a small increase in V_{N_A} immediately results in a punch-through leakage current (I_{N_B} is neg-

ative). The same simulation has been repeated with N_B kept at 0.5V: both currents are positive from the first simulation step, hence there is no punch-through until 17V-18V voltage difference between the two anodes (right image in figure2.9). This phenomenon has been discussed by Langfelder in [36], where it has been shown that, given the same voltage difference $V_{NA} - V_{NB}$, current punch-through is significantly lower when the n+ implants have a positive average voltage $\frac{V_{NA}-V_{NB}}{2}$ with respect to the epitaxial layer. The same isolation structure has been proved to work between n+ implants and n-wells anodes. Though this is less problematic, since red and the green anode have usually low voltage difference and are polarized at a higher voltage than N_0.

The breakdown voltage has been simulated by short-circuiting the two anodes and rising their potential: a break-down voltage of around 17-18V (figure 2.10) has

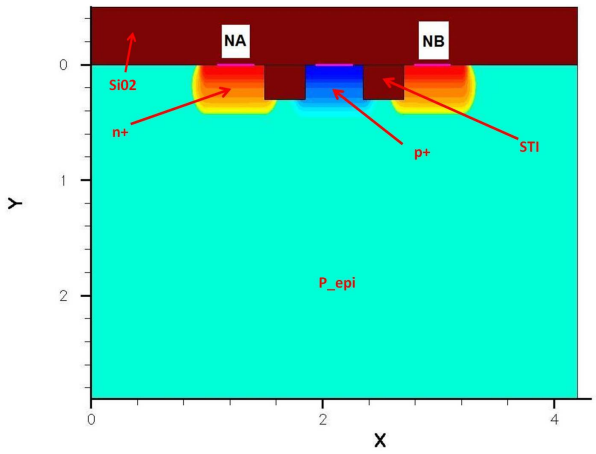

Figure 2.8 *n-p-n with STI structure for punchthrough current evaluation*

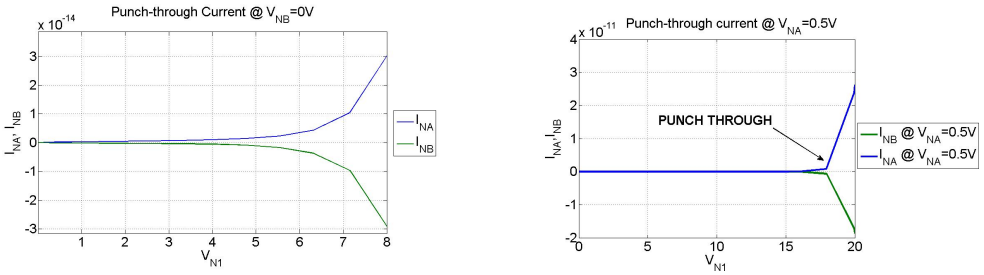

Figure 2.9 *Punch-through current evaluation: In the left image the currents at the two anodes are plotted in function of V_{N_1} with $N_{V_2} = 0V$ while in the lower image N_{V_2} is kept at 0.5 V. In this second biasing condition no punchtrough current is observed before 17V-18V voltage difference*

been found, which is largely higher than the biasing voltages commonly used for the TFD.

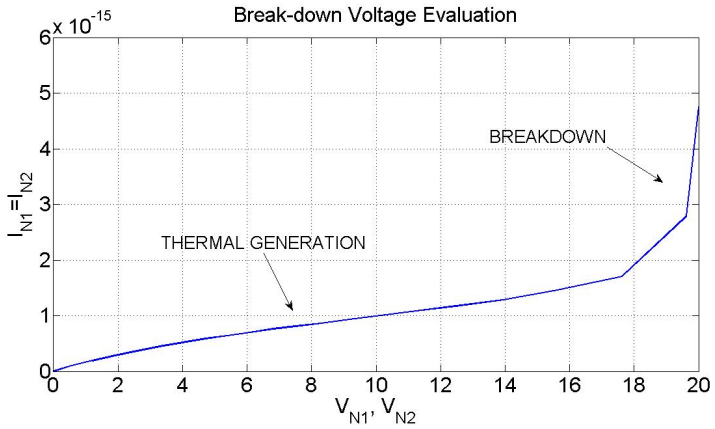

Figure 2.10 *Breakdown Voltage for the structure in fig 2.8*

2.3.1 Optimization for RGB Applications in Terms of Biasing Conditions and Optical Window

The structure of the 3 colors symmetrical and asymmetrical TFD pixels was adapted for the new technology. Most of the design effort has been focused on the optimization of the illumination window to obtain good tunability of the sensor color space, without overly reduce the Fill Factor. The goal was to understand how the illumination window and the biasing conditions impact on the minimum obtainable color reconstruction error, color space tunability and fill factor. Since both biasing and illumination window have a strong impact in the device spectral sensibility, the work-flow wasn't linear, but implied many attempts and loops to find a good starting point which to begin the optimization from.

2.3.1.1 Optical Window Dimensions for maximum tunability

Since the optical window is a fixed parameter, while the biasing voltages can be changed to tune the pixel spectral response, its optimization was the first step of our design. The range of electrical tunability was evaluated for different windows, by simulating the spectral response for many different biasing conditions.

A trade off had to be found between good tunability and an acceptable Fill Factor. The choice of the optical window has also a strong impact on the sensitivity

curves shape, and hence on the device color performances. The optimum shape of the spectral sensitivities has been discussed in many different works by Vora and Trussel [37], and later Sharma [38] and is still an open topic. As a general rule, for good color reconstruction, the signal must be as high as possible and the sensitivity curves should be well balanced and have a small overlap. Referring to the TFD, it has been observed that by choosing a small optical window the curves tend to be less overlapped, however the signal to noise ratio is small, and the blue signal is higher than the other two (unbalanced curves). On the other hand, for a large optical window the signal is higher, but the sensitivity curves tend to overlap and to be unbalanced, with a dominance of the red signal. During our design flow these effects on color performances had been taken into account, but the priority had been on maximizing the spectral tunability range.

Figure 2.11 shows the normalized photo-currents for the three color channels simulated for three different biasing conditions and three different illumination windows. It has been observed that the larger the window, the less tunable the device. For the symmetrical TFD a central optical window large $2.2\mu m$ (corresponding to a FF of approximately 31%) was chosen. The simulated spectral shift is around 80nm for the green channel and 50nm and 55nm for the red and the blue channels respectively.

The same analysis has been done on the asymmetrical TFD structure (figure 2.12): the chosen window is large $2.3\mu m$ (going approximately from the pixel border on the pwell side until the green anode), which corresponds to a FF of around 49%.

2.3.1.2 Optimum biasing for Minimum Color Error Reconstruction

Once the window was set, different biasing conditions have been simulated to evaluate the smallest color reconstruction error that could be obtained. For CFA the color performance depends on the set of filters that is used. To compare the TFD to CFAs, "equivalent filters" are derived by normalizing each photocurrent to the sum of the three photo-currents. The "equivalent filters" give an information about the device color performances which is independent from the technology and from the illuminant spectrum. To correctly evaluate the goodness of the TFD equivalent color filters, the color error has been calculated in the a^*b^* perceptual chromaticity diagram. For this purpose ISET software [5] has been used. This software, developed by Imageval Consulting LLC, is a Matlab tool designed to evaluate how

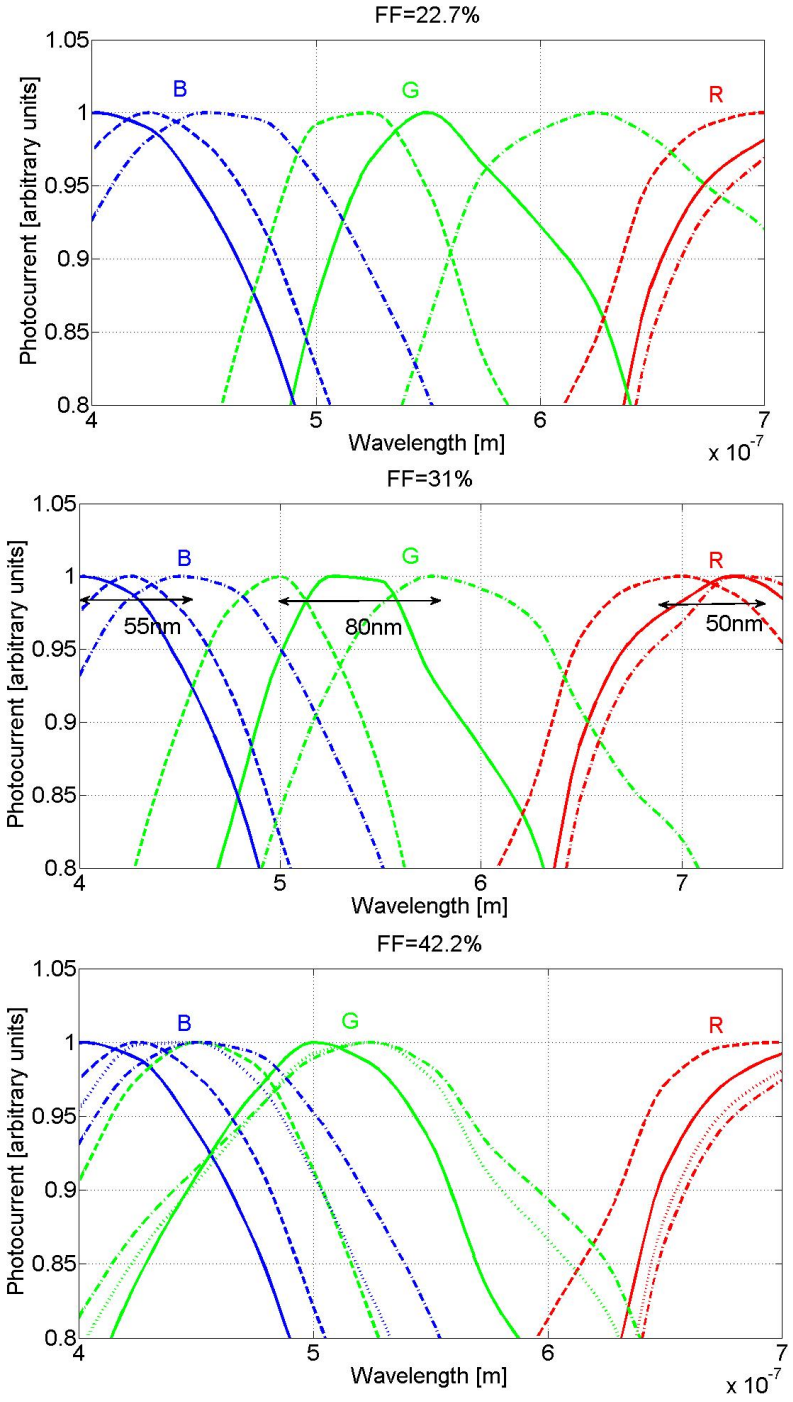

Figure 2.11 *Symmetrical TFD normalized photo-currents at the three color channels for different illumination windows and biasing conditions: The smaller the window the more tunable the device. The solid lines correspond to* $N_0 = 2V$ $N_1 = 6V$ $N_2 = 4V$*, the dashed lines to* $N_0 = 1V$ $N_1 = 9V$ $N_2 = 9V$ *and the dotted-dashed lines to* $N_0 = 3V$ $N_1 = 6V$ $N_2 = 3V$*.*

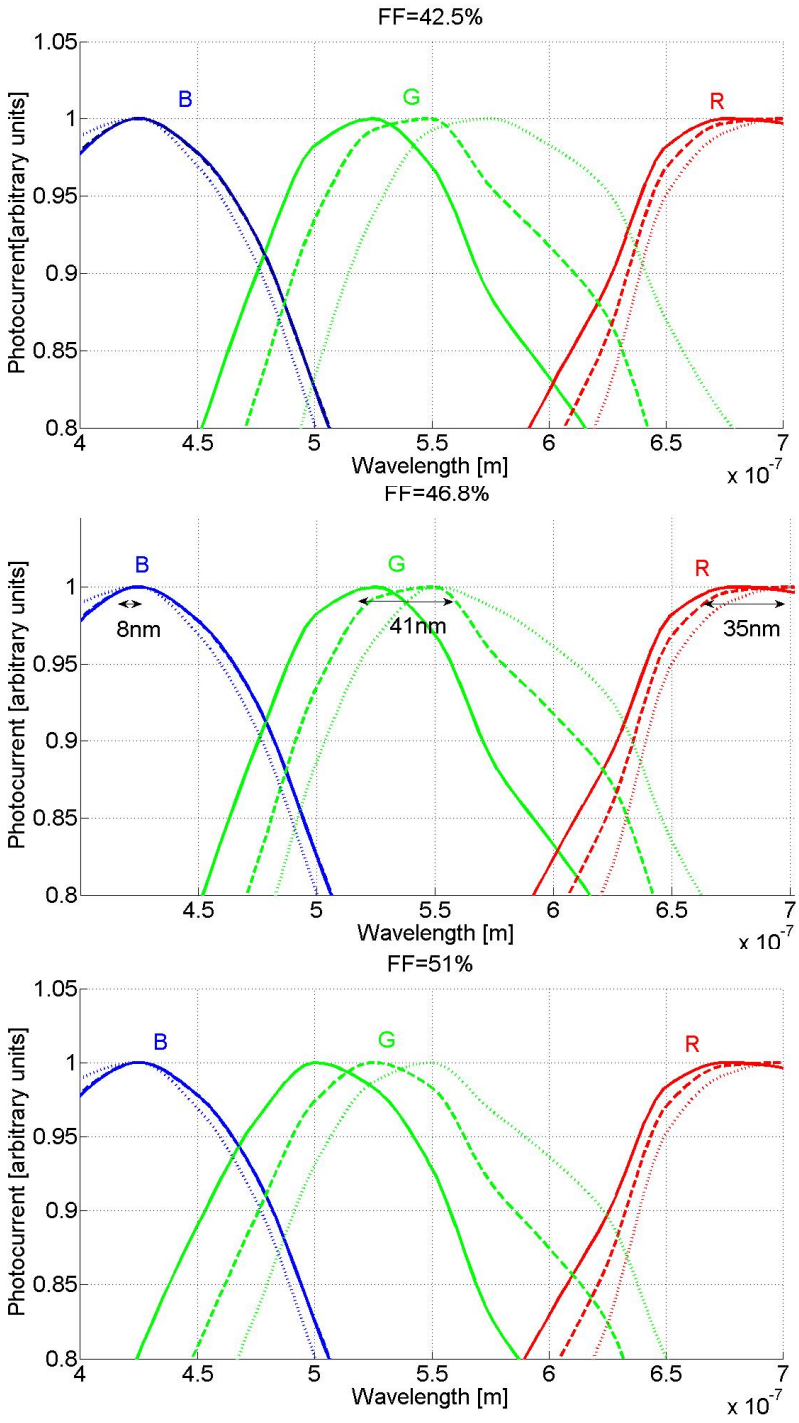

Figure 2.12 *Normalized photo-currents at the three color channels of an asymmetrical TFD (figure 2.7) for different FF: The smaller the window the more tunable the device. Solid lines refer to* $N_0 = 0.4V$ $N_1 = 8V$ $N_2 = 7V$*, dotted lines to* $N_0 = 0.5V$ $N_1 = 6V$ $N_2 = 8Vs$ *to and dashed lines* $N_0 = 0.5V$ $N_1 = 5V$ $N_2 = 10V$

the characteristics of the imaging optics and of the sensor influence image quality. This software includes general test charts for standard image quality testing. In this work, the evaluation of color reconstruction has been based on simulating the color channels response, under illuminant D_{65}, to a Macbeth Color Checker as scene. The simulated sensor responses are used to derive the optimum 3x3 linear Color Correction Matrix. Once the optimum CCM calculated, the corresponding ΔE_{ab} is derived.

Figure 2.13 shows the equivalent filters of hte symmetrical TFD pixel simulated for different biasing conditions with the chosen illumination window. The corresponding CCM and ΔE_{ab} have been calculated with ISET and compared. The bold solid curves represent the set of equivalent filters for the optimum biasing condition ($N_0 = 1V\ N_1 = 9V\ N_2 = 9V$). The goodness of these equivalent filters can be appreciated even before calculating the color error, since they are balanced, and well distributed in the visible spectrum. The corresponding CCM is:

$$\begin{bmatrix} -0.6306 & -2.1752 & 3.0775 \\ 0.3727 & 3.1908 & -2.2233 \\ 1.1435 & -1.9379 & 0.7785 \end{bmatrix}$$

and the obtained color error is $\Delta E_{ab} = 3.02$ (figure 2.14).

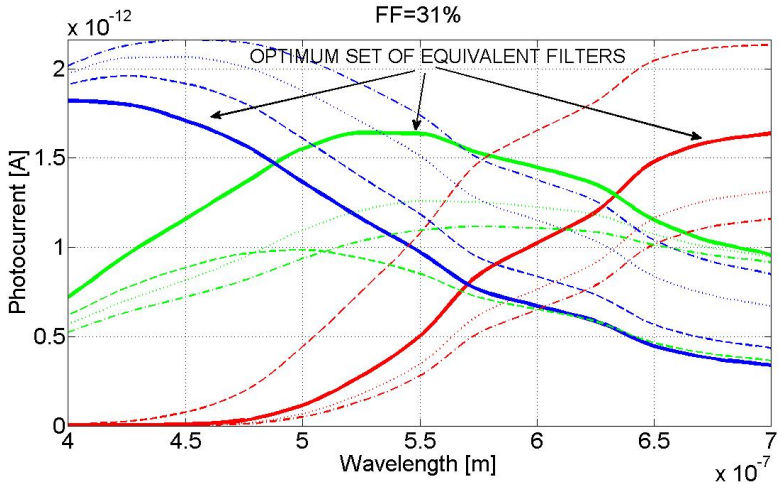

Figure 2.13 *Equivalent filters for different biasing conditions for the symmetrical TFD structure with a FF=31%. Solid lines refer to $N_0 = 1V\ N_1 = 9V\ N_2 = 9V$, dotted lines to $N_0 = 2V\ N_1 = 6V\ N_2 = 4Vs$, dashed lines to $N_0 = 0.5V\ N_1 = 35V\ N_2 = 9.5V$ and the dotted-dashed lines to $N_0 = 3V\ N_1 = 6V\ N_2 = 3V$. The three solid bold lines are the most balanced and represent the optimum equivalent filters*

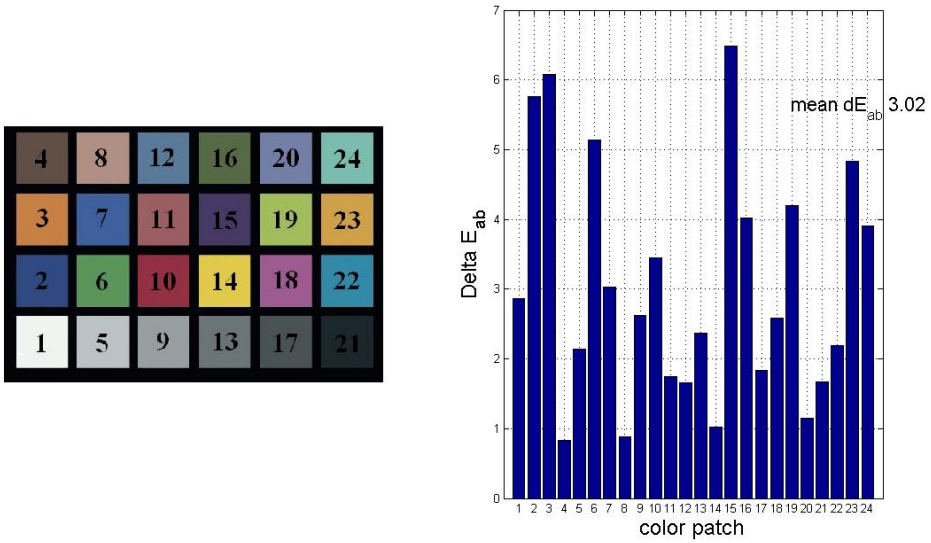

Figure 2.14 *Color reconstruction error in the L^*_{ab} color space calculated with ISET software for the optimum polarization*

The same evaluations have been done on the asymmetrical TFD structure. The optimum biasing condition ($N_0 = 0.4V$ $N_1 = 8.0V$ $N_0 = 7.0V$) corresponds to the photocurrents in solid bold lines in figure 2.15. The corresponding optimum CCM calculated with ISET is:

$$\begin{bmatrix} 1.2747 & -3.0744 & 1.4674 \\ 0.02290 & 4.1426 & -2.8872 \\ -0.5001 & -1.7320 & 2.4869 \end{bmatrix}$$

and the obtained $\Delta E_{ab} = 2.95$ (figure 2.16)

In conclusion, the spectral sensitivity of the TFD color channels showed an important dependence both on the biasing conditions and on the optical window. To obtain sharp and tunable responses a narrow aperture would be preferable (as long as the blue signal doesn't become dominant), but it would reduce the Fill Factor, and hence the signal. During the design a good compromise between the two aspects has been found. The symmetrical structure shows a better tunability than the asymmetrical one, which in exchange is smaller and has a better Fill Factor. From this first analysis, we can already see the enormous improvement given by this new design with respect to the old one, where the color error was around 3, but the CCM most negative coefficient was -11.60. As a reference, figure 2.17 shows

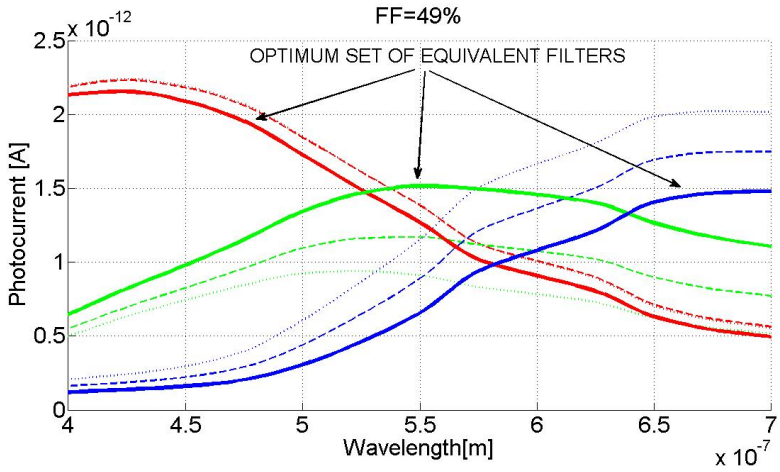

Figure 2.15 *Equivalent filters for different biasing conditions for the asymmetrical TFD structure with a FF=46.8%. Solid lines refer to* $N_0 = 0.4V$ $N_1 = 8V$ $N_2 = 7V$*, dotted lines to* $N_0 = 0.5V$ $N_1 = 6V$ $N_2 = 8Vs$ *to and dashed lines* $N_0 = 0.5V$ $N_1 = 5V$ $N_2 = 10V$*. The three solid bold lines are the most balanced and represent the optimum equivalent filters*

the CCM and the color reconstruction error calculated with ISET for a Nikon D70 under a D65 light, using the Macbeth Color Checker as a scene [5]. The color error is of the same order of the one obtained with the TFD, but the negative values of

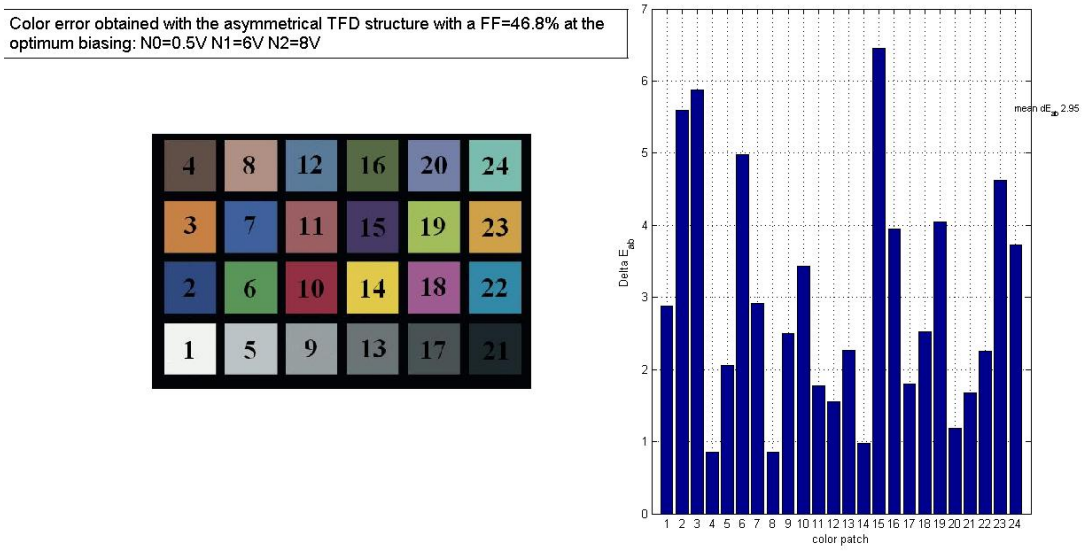

Figure 2.16 *Color reconstruction error in the* L^*_{ab} *color space calculated with ISET software for the optimum polarization for the asymmetrical TFD structure*

the corresponding CCM are smaller. For the equivalent filters of this sensor refer to figure 4.9. Even if the TFD is not yet at the same level of CFAs in terms of color performances, the obtained values are promising in the optics of the development of a device, not only capable to acquire color images, but also to implement many other new features.

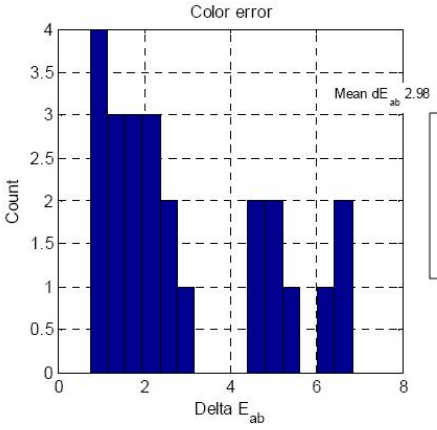

1.6206	-0.1760	0.0366
-0.2283	0.9763	-0.3084
-0.3916	-0.4610	2.3294

Figure 2.17 *Color Correction Matrix and Color Reconstruction Error of a Nikon D70 under a D65 light, using as an image the Macbeth Color Checker and estimated with ISET [5]*

2.4 Isolation in Mini-matrices

In the previous run, the red and the green channels of TFD mini-matrices didn't work, preventing from obtaining any experimental results for these structures. Among the possible causes of this phenomenon, the most probable was a bad isolation between adjacent pixels. Figure 2.18 shows the schematic top view of the half of two 3 colors symmetrical pixels facing each others in a minimatrix.

The two N_{wells} of anodes N_{2A} and N_{2B} are isolated by means of a P_{well}, which only extends for the width of the N_{wells}. Hence the hypothesis was that a punchthrough current was flowing between the anodes of the two pixels. Since the problem was observed also when all the anodes where biased at the same potential, it was supposed that a small voltage difference between anodes due to threshold voltage fluctuation of the gain transistor of the readout-stage was always present. The foundry estimates this ΔV to be around 20mV. The hypothesis of bad isolation was first checked by means of 3D simulations in Dessis, and then confirmed through experimental measurements. Figure 2.19 shows the 3D structure of two adjacent symmetrical

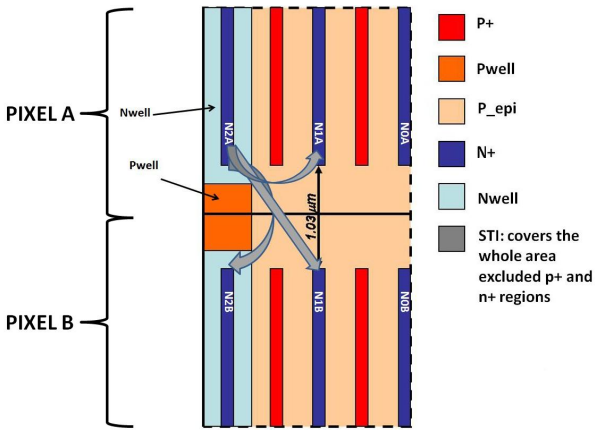

Figure 2.18 *Layout of the structure of two adjacent pixels in the mini-matrices implemented in the previous run. The only isolation consists in a Pwell between the two Nwells of two facing red anodes of the two pixels. The blue arrows indicate the possible punch-through current flows among one ref anode and other anodes due to bad isolation.*

TFDs. For symmetry and computational reasons only the half of the two pixels structure has been simulated. To understand which channels were interfering with each-others, two different simulations have been made. In the first simulation the anodes of each pixel were short circuited, and an increasing voltage difference was been applied between two pixels. Already for ΔV of 50mV-100mV a punch-through current started to flow between the two red anodes N_{2A} and N_{2B}. No current was exchanged between the green anodes of the two pixels. In the second simulation the green anode N_{1A} was biased at 0.7 V, while all the other anodes of the two pixels were short circuited and biased at 1V. For this particular condition a punch-through current was flowing between N_{1A} and the two red channels. Figure 2.20 shows the current density profile at a depth of $0.3\mu m$, $0.5\mu m$ and $1\mu m$ respectively. While almost no punchtrough current is observed underneath the surface, the current density is higher at $1\mu m$. The arrows indicate the current flowing between the anodes at $1\mu m$ from the surface. Thus the dysfunction of the green channels was not due to a punch-through current between the two green channels N_{2A} and N_{2B}, but between the two red channels of the two pixels and between the green channels and the two red channels.

In this run a more efficient isolation solution has been implemented. The isolating P_{well} has been extended for the whole width of the pixel, and kept at the substrate potential. Figure 2.21 shows the simulated 3D structure. The oxide that covers the whole structures except for the n+ and p+ implants and the STI are not visible

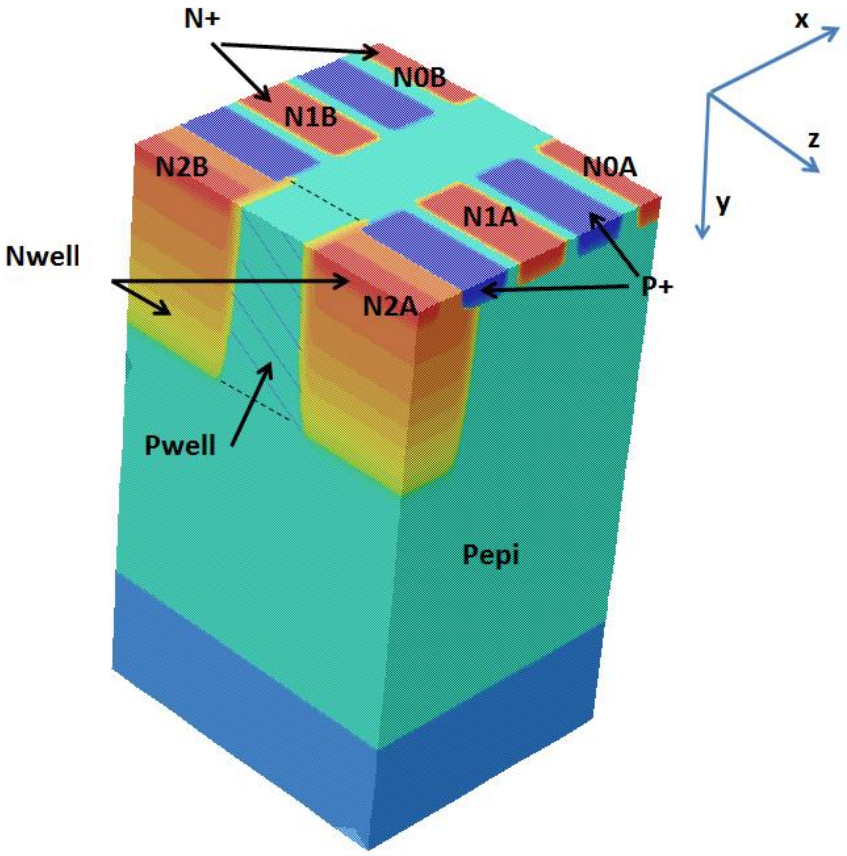

Figure 2.19 *3D simulated structure of adjacent pixels in mini-matrices implemented in the previous run.*

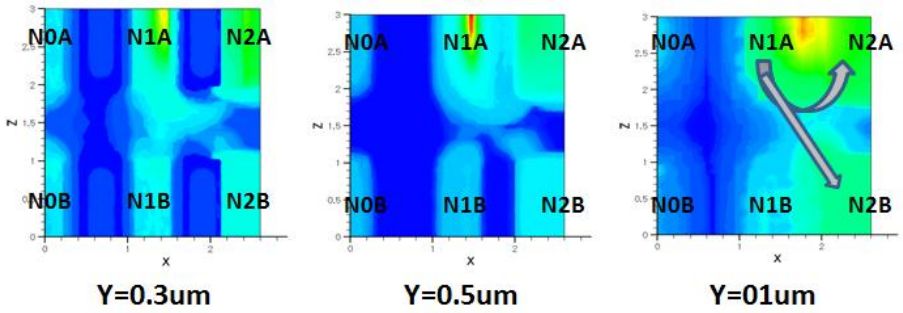

Figure 2.20 *Current density at 0.3um, 0.5um and 1um depth for N_{1A} biased at 0.7V and all the other anodes at 1V. There is a punch-through current between anode N_{1A} and N_{2A}, but also between N_{1A} and N_{2B}. The current density is higher in deeper regions, since the N_{wells} extend deep in the device.*

for image's clarity reasons. The 3D simulations have been repeated for this last structures, and no punch-through current was exchanged between any anode, even for voltage differences of many Volts.

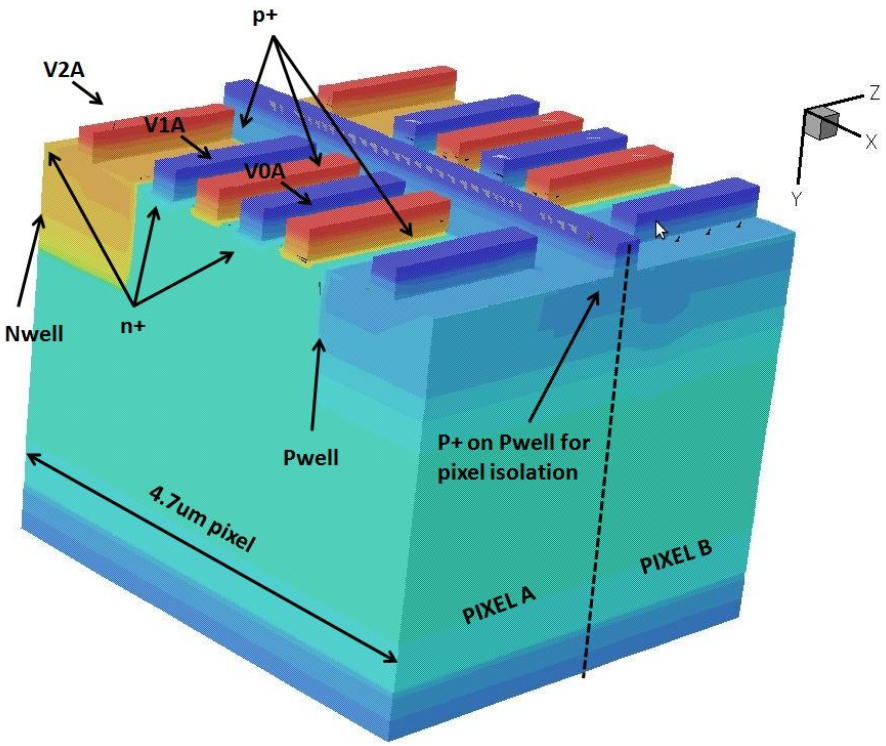

Figure 2.21 *3D simulated structure of two adjacent asymmtrical TFD pixels a mini-matrix implemented in this run.*

Chapter 3

VLSI design of the device and the integrated readout electronics

In this section the VLSI design of the passive TFD pixel and of the active mini-matrices will be described. The design and layout of the integrated circuit has been realized with CADENCE software. After giving a brief overview of the structures on chip, the discussion will focus on the VLSI design of the symmetrical and asymmetrical TFD pixel structures described in Chapter 2, and on the VLSI design of active mini-matrix and their readout electronics.

3.1 Designed TFD Structures on Chip

The layout of all the structures on chip is shown in figure 3.1. The passive structures implemented in this run were symmetrical and asymmetrical 3 colors TFD pixels. One asymmetrical TFD passive pixel for standard 3 colors acquisition, and two different symmetrical TFD passive pixels, one for standard 3 colors acquisition, and the other with the 5 anodes that can be individually biased (in the figure indicated as 5 colors symmetrical passive pixel) have been designed. Four different active mini-matrices formed by 3 colors 2×2 TFD pixels have been implemented. The four mini-matrices differ only in the readout electronics. In particular, two mini-matrices were designed with the readout electronics that is described later in this chapter: one has the reset voltage level shifters integrated on chip, while for the other the signal for the reset of the feedback capacitances is provided from outside. The other two mini-matrices structures are not the object of this work.

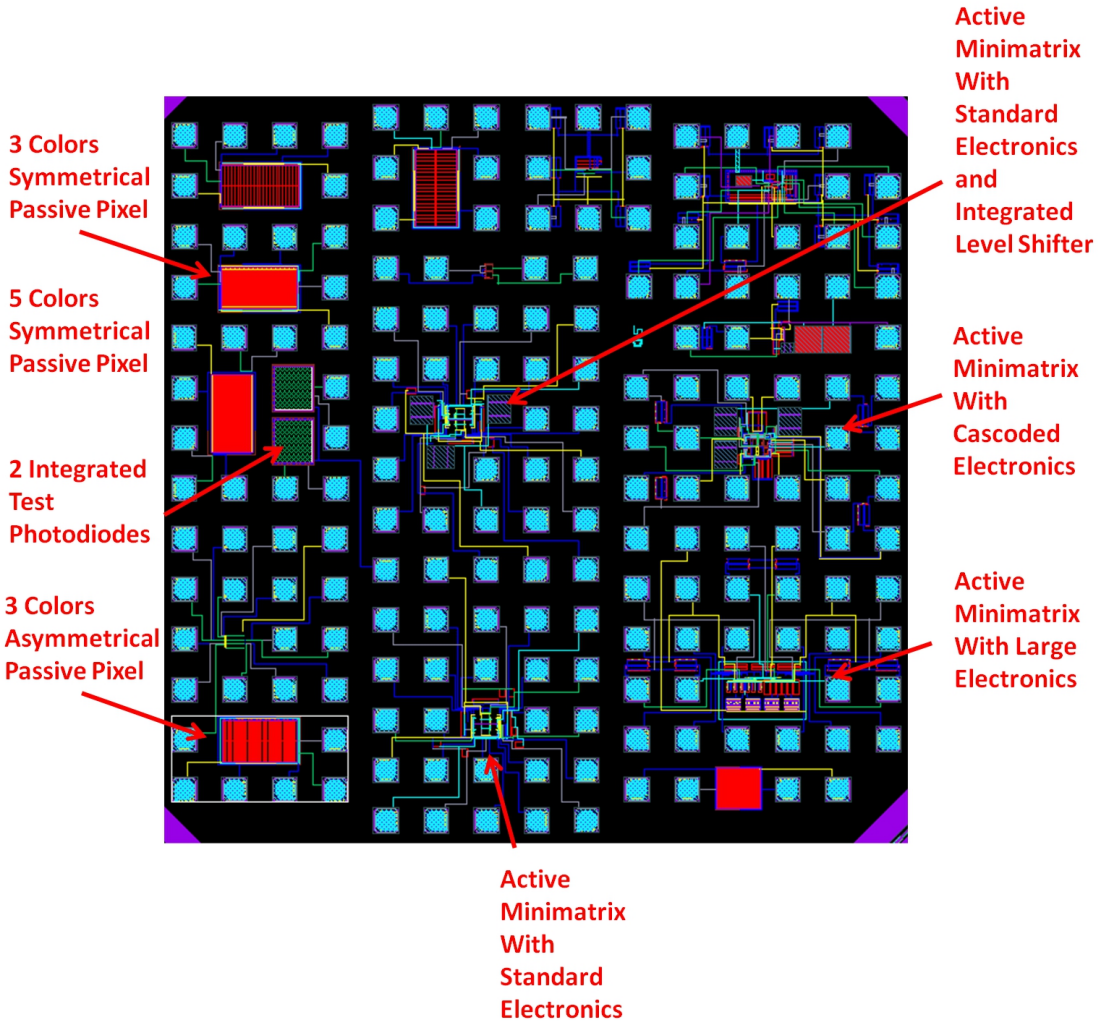

Figure 3.1 *Layout of the structures on chip*

3.2 VLSI Design of Symmetrical and Asymmetrical TFD Pixels

The layout of passive symmetrical and asymmetrical 3 colors TFD pixels is shown in figure 3.2 and 3.3 respectively. The symmetrical pixel is formed by 27 parallel TFD unit cells. Every unit is 7.1μm large and 95 μm long. Following the optimization described in chapter 2, the illumination window is large 2.2μm, which corresponds to a Fill Factor of 31%. The parallel arrangement guarantees a fairly high output signal, which allows to test the TFD working principle, color performances and tunability, without the need of any integrated electronics. The non-active areas in the pixel are covered with metals, to avoid photo-generation in the regions where the electric field has not a suitable profile for color separation. The borders of the optical window are implemented with vias of all metals. Following the same strategy, also the asymmetrical TFD pixel has been implemented by placing in parallel 40 asymmetrical TFD unit cells, which are 105μm long and 4.7μm large. In particular, the 40 strips have been coupled in pair, one facing the other (as shown in figure 3.3). There are 20 illumination windows (one every two pixels), with an aperture of 4.6μm, which is twice the width obtained from the optimization described in chapter 2. The corresponding FF is 49%.

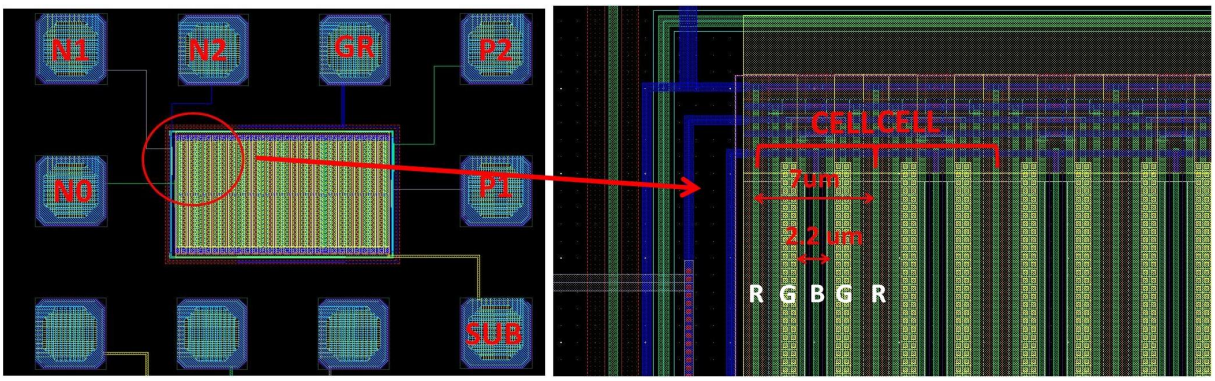

Figure 3.2 *Layout of the symmetrical 3 colors TFD*

3.3 VLSI Design of Active Mini-Matrices and the corresponding Readout Electronics

To develop a full CMOS sensor of TFD pixels, active readout topologies, which enable charge to voltage conversion and pre-amplification at pixel level, must be implemented.

Most of CMOS sensors are based on Active Pixel (AP) with 3 or 4 transistors (as described in section 1.3.2.1), where the photo-charge is directly integrated on the anode capacitance, which is the sum of the photo-diode depletion capacitance and of other parasitic capacitances affecting the anode. During the integration, the anode voltage decreases proportionally to the number of photons impinging on the photodiode.

Implementing an Active Pixel with a TFD is not trivial. In fact, unlike for photo-diodes, since the biasing scheme determines the electric field configuration and hence the color channel spectral sensitivity, the voltage of the collecting/biasing anodes must be constant during the integration time. An alternative readout electronics must be implemented. In the solution proposed in this work, the photo-charge is integrated on the feedback capacitance of a single transistor charge preamplifier. During the integration time the anode voltage is maintained stable as it is the virtual ground of a feedback circuit. This readout topology requires three other transistors: one for the biasing of the preamplifier, one for the reset of the feedback capacitance and a third to implement a source follower buffer, which guarantees a low output impedance. Hence the complexity is comparable with the one of a 3T AP.

Figure 3.4 shows one of the designed active mini-matrix made of 2×2 pixels, encircled by its readout electronics. For space saving the capacitances were designed on top of the transistors. For the isolation between adjacent pixels the solution

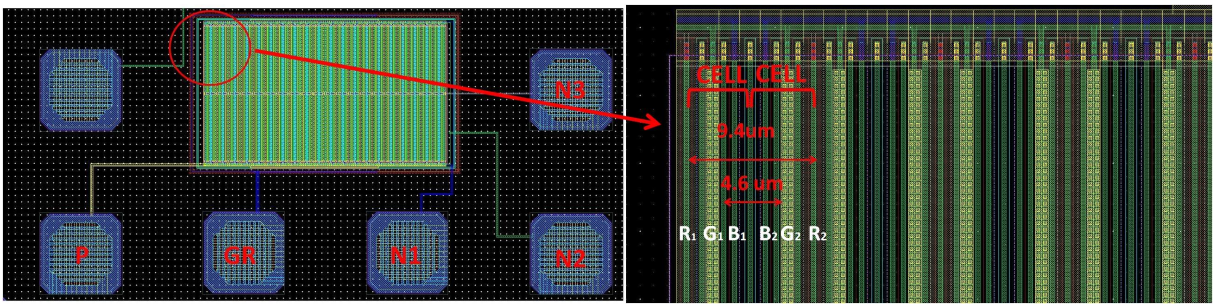

Figure 3.3 *Layout of the asymmetrical 3 colors TFD*

described in Chapter 2 was implemented. Each pixel is $10\mu m \times 10\mu m$, and, together with its readout electronics, it occupies an area (including dead areas) of $22\mu m \times 22\mu m$. Hence the overall area occupied by the mini-matrix is $44\mu m \times 44\mu m$, with a Fill Factor of 20%.

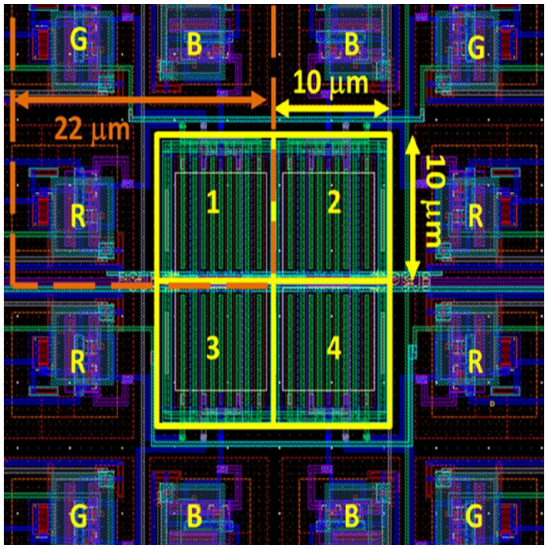

Figure 3.4 *4×4 pixels mini-matrix. The active area of each pixel is $10\mu m \times 10\mu m$, while the overall area, including the readout electronics is $22\mu m \times 22\mu m$.*

3.3.1 Standard Readout Topology

Figure 3.5 shows the schematic of the readout circuit for one color-channel. The readout flow is as follow:

1. Reset Phase: After each integration time the voltage across the feedback capacitance is zeroed by the reset transistor. The circuit output is thus set to the anode voltage.

2. Light Integration: the photocharges, which are generated by photons in the anode collecting region, drift toward the electrodes and are integrated on the feedback capacitance. Since the negative feedback loop stabilizes the anode voltage during the integration time, the output voltage of the charge preamplifier increases of the same amount of the voltage across the capacitance, which is directly proportional to the number of collected photo-charges. The output of the preamplifier is connected to a unity gain buffer, implemented by means

of a transistor in source follower configuration, which allows a low impedance readout of the output voltage.

3. Reset Phase: The voltage across the feedback capacitance is reset again, and a new light integration can start.

The overall circuit can be divided in 4 sub-circuits, whose characteristics are described in the next sections. The four pixels are identically biased, hence there are three reset signal generators, one for each color, which are shared by the pixels. Three current generators, which are also shared by the four pixel, are used to bias the pre-amplification stages by means of current mirrors. Each anode has its own charge preamplifier and its output source follower stage. The circuit has been simulated and designed with Cadence.

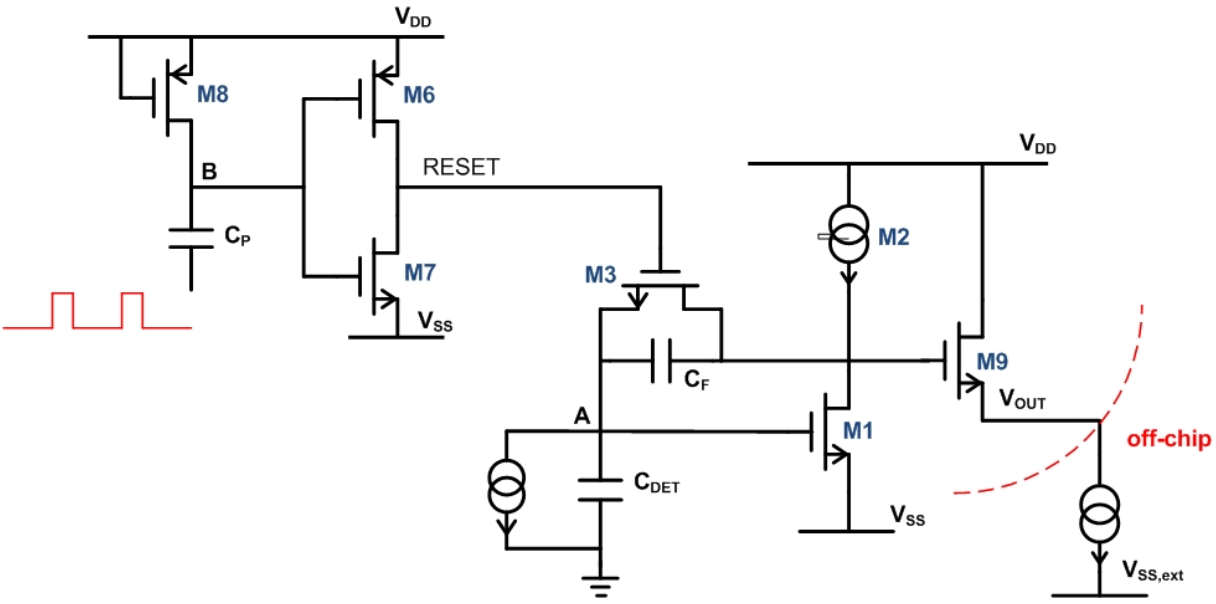

Figure 3.5 *Standard TFD readout electronics.*

3.3.1.1 Sensor Model

To model the TFD, a current generator in parallel with a capacitance have been used (figure 3.6). The device capacitance has been approximated to $\frac{1}{3}$ of the capacitance of a depletion region of 3um:

$$Cdep = \frac{A_{pix}\varepsilon_{Si}}{X_{dep}} \tag{3.1}$$

where:

$$Xdep = \sqrt{\frac{2\varepsilon_{Si}(V - V_{bi})}{qN_a}} \tag{3.2}$$

thus

$$Cdep = A_{pix}\sqrt{\frac{qN_a\varepsilon_{Si}}{2(V + V_{bi})}} \tag{3.3}$$

By using: $N_a = 1.6 \cdot 10^{15} cm^{-3} = 1.6 \cdot 10^{21} m^{-3}$, $q = 1.6 \cdot 10^{-}19C$, $\varepsilon_{Si} = 8.85 \cdot 10^{-12} \cdot 11.7F/m = 103.5 \cdot 10^{-12} F/m$, $A_{pix} = 100\mu m^2$ and $V + V_{bi} = 5V$; the obtained capacitance is $C_{dep} \approx 5fF$ and thus $C_{anode} \approx 1.7fF$. This is clearly an approximation, since the capacitance changes depending on the anode we are referring to. Furthermore the depleted region strongly depends on the biasing conditions. To take some margin it has been decided to use a capacitance of $10fF$.

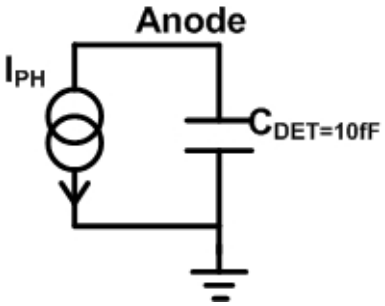

Figure 3.6 *TFD model schematic*

3.3.1.2 Charge Preamplifier

Figure 3.7 represents a schematic of the charge preamplifier. This stage has been designed to amplify and transform the photo-charge into a voltage signal, keeping the anode at a constant electrical potential. M_2 provides the biasing current for M_1, which represents the gain transistor of the amplifier. C_F is the feedback capacitance on which the photo-current is integrated, generating an output voltage:

$$V_X(t) = V_{GS1} + V_{CF}(t) = V_{GS1} + \frac{Q(t)}{C_F} = V_{GS1} + \frac{(i_{ph} + i_d) \cdot t}{C_F} \tag{3.4}$$

M_3 is the reset transistor, which zeros the voltage across the capacitance after each integration period. The power supply VSS is controlled from the outside, and VDD is always $VSS + 1.8V$ (since only 1.8 V core transistors are used).

The circuit has a negative feedback loop, which stabilizes the voltage V_{G1} of the

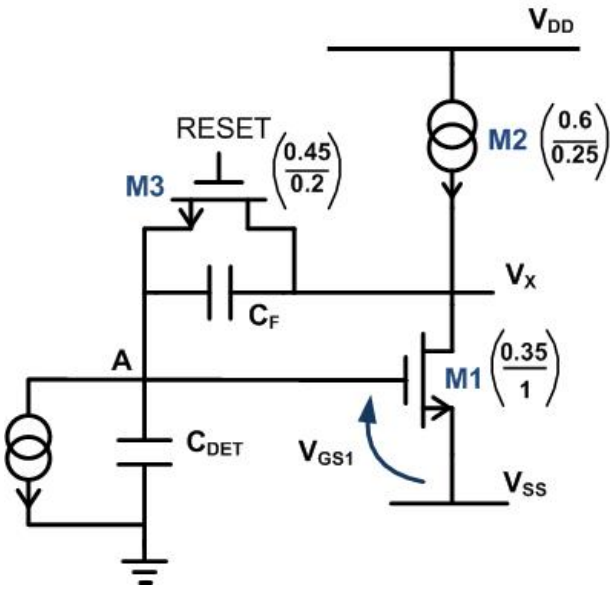

Figure 3.7 *Charge Preamplifier Schematic.*

TFD anode so that the whole current injected by M_2 in node X enters the drain of M_1. The open loop gain can be studied by opening the circuit at the gate of M_1 and by applying a small voltage signal v_T (figure 3.8). The Input voltage modulates the transistor current so that

$$i_1 = v_T g_{m1} \tag{3.5}$$

where g_m is the transconductance $\frac{\delta I_D}{\delta V_{GS}}$. The current changes the voltage across the output resistance according to Ohm's law:

$$v_X = -i_1 R_{out} \tag{3.6}$$

with

$$R_{out} = r_{01} // r_{02} \tag{3.7}$$

where r_{01} and r_{02} are the drain output resistances of transistors M_1 and M_2.

Hence:

$$v_T{}' = -v_T gm R_{out} \tag{3.8}$$

Thus, if M_2 is designed to have a higher output impedance than M_1:

$$G_{loop} = -\frac{v_T{}'}{v_T} = gm R_{out} \approx -gm r_{01} \tag{3.9}$$

To size M_1, the channel had to be designed long enough to obtain high output impedance, without resulting in a too small $\frac{W}{L}$ ratio. For this purpose L_1 was made $1\mu m$, and W_1 was chosen by maximizing the loop gain $g_m r_{01}$ at a certain inversion conditions for transistor M_1. The target is too obtain a loop gain high enough to guarantee that during the integration time the anode voltage changes of an amount ΔV_{anode} which is negligible with respect to the fluctuations of V_{GS1} determined by the technology. These fluctuations have been estimated by means of a Monte Carlo simulation to be around 30mV. It has been verified that such fluctuations do not influence the device spectral performances. Since the maximum voltage variation at the anode is 1.8 V:

$$1.8V/(1 - G_{loop}) \leq 30mV \tag{3.10}$$

Hence the loop gain must respect the following condition:

$$\|G_{loop}\|) \geq 1.8V/20mV - 1 = 59 \tag{3.11}$$

Figure 3.9 shows the results of a Cadence parametric simulation of the maximum gain, the output conductance and the overdrive voltage $(V_{GS} - V_T)$ of transistor M_1 depending on the biasing current and on the channel width. To avoid large transistors, which would reduce the Fill Factor, W_1 was designed with dimensions slightly larger than the minimum ones (350nm), and the bias current was chosen so that M_1 is in moderate inversion. The inversion coefficient can be calculated as:

$$IC = \frac{I_{DS1}}{2n\mu_n C'_{ox}(\frac{W_1}{L_1})(V_{TH})^2} \tag{3.12}$$

To be in moderate inversion IC must be between 1 and 10. For IC=3.7

$$I_{DS1} = IC2n\mu_n C'_{ox}(\frac{W_1}{L_1})(V_{TH})^2 \approx 1\mu A \tag{3.13}$$

For these width and bias current values the simulated maximum gain $g_m r_{01}$ is equal to 70. M_2 was sized to have a larger output impedance than M_1. Considering that in LF150 technology P_{MOS} have better performances than N_{MOS}, with $W_2 = 600nm$ and $L_2 = 250nm$ an output resistance $r_{02} = 12.24M\Omega$ is obtained. By considering the presence of r_{02}, the loop gain is around -50 (hence $\mid G_{loop} \mid \approx 34dB$).

To implement the feedback capacitance, a minimum dimension MIM (Metal Insulator Metal) capacitor has been used. Figure 3.10 shows a schematic of the

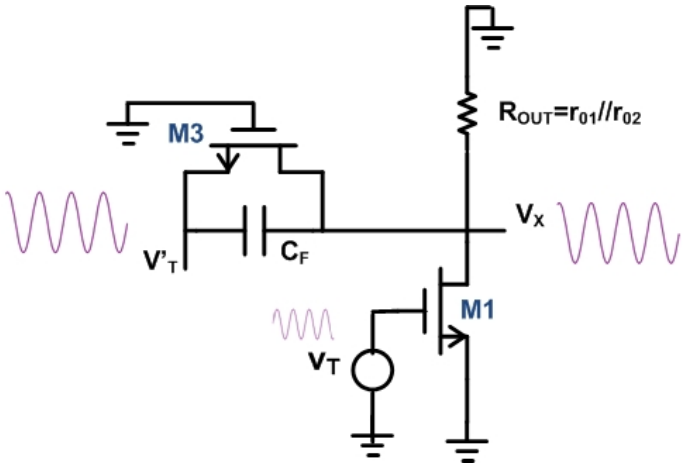

Figure 3.8 *TFD model schematic*

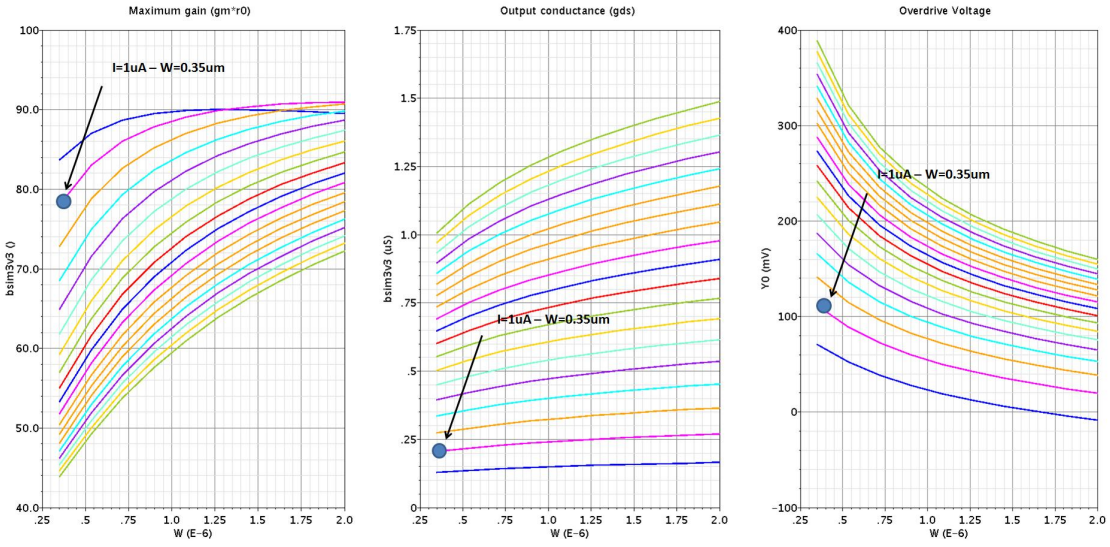

Figure 3.9 *Maximum gain gm_1r_{01}, output conductance gds_1 and Overdrive Voltage of MOS M1 for different biasing currents and channel width. The simulation evaluated the previous parameters for a current from $0.6\mu A$ (blu lines) to $10\mu A$ (light green lines)and for a channel width from $0.35\mu m$ to$2\mu m$*

layers in LF150 technology. MIM capacitances are implemented between Metal Final and Metal 5 and the minimum area is $5\mu m \times 5\mu m$, resulting in a minimum capacitance of 26.7fF. A smaller capacitance would be preferable to obtain a higher gain in the charge to voltage signal transduction. In fact

$$\Delta V_{CF} = \frac{I_{ph}}{C_F} \tag{3.14}$$

The last element of this stage that has been sized was the reset transistor M_3, which was designed with dimension slightly bigger than the minimum ones: $W_3 = 450nm$ and $L_3 = 200nm$.

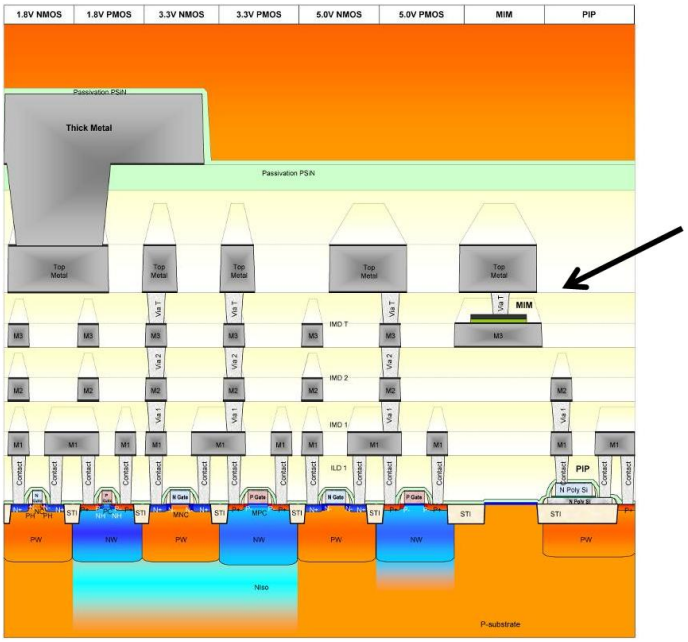

Figure 3.10 *Schematic of the layers in LF150 technology. MIM capacitances are implemented between Metal Final and Metal 5. [6]*

3.3.1.3 Source Follower Output Stage

The output stage consists in a buffer, implemented with a MOS transistor in the source-follower configuration (figure 3.11), which, thanks to its high input and low output impedances, decouples the readout circuit from the output load. The stage is biased from the outside with a current generator, stabilized with a negative feedback loop (which will be described in the next chapter together with the discrete component electronics of the readout-board), here represented with a current gen-

erator. The minimum current that doesn't affect the performances of the BJT of the discrete component current generator (shown in figure 4.17) is around $1\mu A$: the Slew Rate of the buffer circuit was calculated, in order to evaluate if such a small current introduces non-linearities.

$$SR = \frac{\Delta V_{outMAX}}{\Delta T} = \frac{I}{C_{MAX}} \tag{3.15}$$

Where ΔT is the integration time, and ΔV_{outMAX} is 1.8V. For a frequency of $10KH_z$ (corresponding to $\Delta T = 100\mu s$, which is smaller than the integration times normally used in for still cameras) the maximum output capacitance is $C_{MAX} = 55pF$, which is higher than the actual one. M_9 was sized in order for the buffer to transfer at least 90% of the signal.

$$\frac{v_{out}}{v_X} = \frac{R_{GEN}}{\frac{1}{gm_9} + R_{GEN}} \geq 0.9 \tag{3.16}$$

$$\frac{gmR_{GEN}}{1 + gmR_{GEN}} \geq 0.9 \tag{3.17}$$

$$gm \geq \frac{9}{R_{GEN}} \tag{3.18}$$

For a current of $1\mu A$ and an input resistance of the current generator of $500K\Omega$ the minimum acceptable transconductance gm would be $20\mu A/V$. Fixing $L_9 = 6L_{min}$ the resulting W_9 is $1.76\mu A$. In practice the current generator output impedance is of the order of $G\Omega$, thus the transfer coefficient will be approximately 1.

3.3.1.4 Biasing Current Generator Stage

Figure 3.12 shows the schematic of the circuit that implements the current generator for the biasing of the charge-preamplifier. There are three current generators for the whole matrix, one for each color. It is composed of a voltage divider and a current mirror. The voltage divider was implemented with two MOS transistors in trans-diode configuration and a resistor. It could have also been implemented with only one transistor plus a resistor with a resistance equal to $1/gm_5 + R_{pol}$, but this second solution would occupy a larger area, since integrated resistors have a low specific resistance. The biasing current is $1\mu A$, as discussed in the previous section. A mirror coefficient around 12 has been chosen, which lead, after final optimizations,

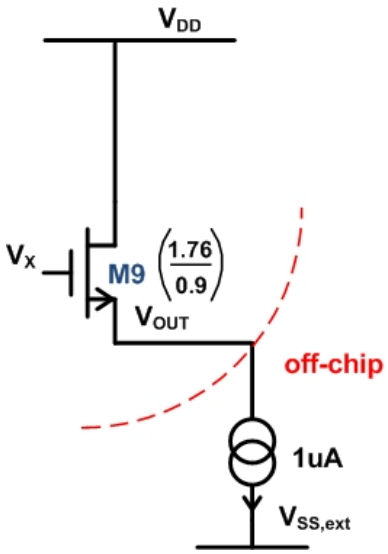

Figure 3.11 *Output buffer. The biasing current generator is off-chip.*

to size M_4 with $W_4 = 7.1\mu m$ and $L_4 = 200nm$. For the sizing of R_{POL} and M_5, some considerations concerning area occupation have been made. At first the circuit has been simulated by replacing R_{POL} with an ideal current generator, and the resulting V_{GS5} corresponding to different channel lengths of M_5 has been evaluated. The goal was to maximize V_{GS5}, in order to use a resistance as smal as possible. W_5 was designed with minimum dimensions (320nm), and L_5 was made $3\mu m$. With these values a resistance of $15.94K\Omega$ was sufficient to correctly bias the stage. Given the specific resistance, and the minimum technological dimensions, the resistor was made $5\mu m \times 62.4\mu m$.

3.3.1.5 Reset Signal Translator

The feedback capacitance of each color channel needs to be reset after each integration period. Only three reset signal translators are needed for the whole matrix, since the four pixels are biased with the same voltage scheme. This is implemented by putting a transistor in parallel with the capacitance. For the capacitance to be correctly reset, the signal at the gate of transistor M3 must go between V_{SS} and V_{DD}. Since V_{SS} and V_{DD} change depending on the required biasing conditions of the device, the reset signal must change as well. Hence a translator for the reset signal is needed. For 3 over 4 mini-matrices the reset signal translator has been designed embedded on chip. The reset signal is provided from outside and is a

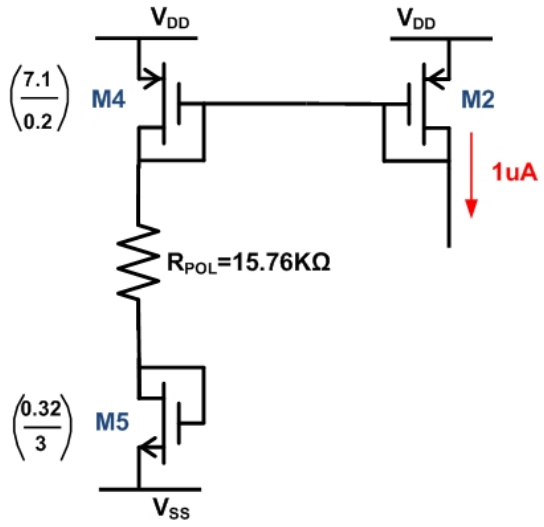

Figure 3.12 *Biasing Current Generator.*

rectangular wave of 1.8V of amplitude, whose frequency depends on the integration time. The circuit shown in figure 3.13 is made of three transistors: M_6 and M_7 form an inverter, whose output voltage goes between V_{SS} and V_{DD}, while M_8 is a off transistor used as a resistance. The reset rectangular signal is transfered to the input of the inverter by means of the capacitance C_P. M_8 and C_P are sized to have high output resistance, so that the RC discharge long enough for the input voltage to be approximately constant during the integration time. M_8 was sized to have $\frac{W_8}{L_8} = \frac{5\mu m}{0.17\mu m}$ the off resistance of the transistor is $113.6G\Omega$. For $C_p = 4pF$, the resulting RC time constant is $\tau = 113.6G\Omega \cdot 4pF \approx 450ms$ which is far longer than the integration times used for the pixel carachterization.

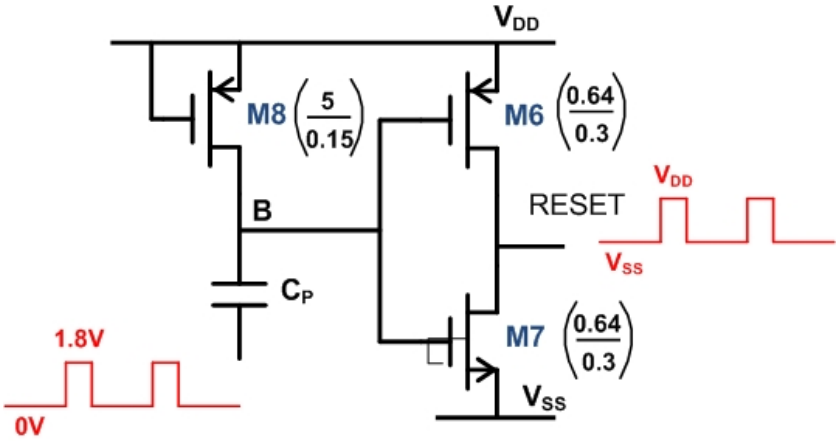

Figure 3.13 *Level Shifter for the Generation of the Reset Signal*

Chapter 4

Experimental Set-Up and Results

The designed passive pixels and mini-matrices have been tested and characterized in terms of dark current, fixed pattern noise, linearity, spectral responsivity and tunability, and finally compared with the state of the art. The chapter starts with an overview of the TFD experimental set-up, followed by the description of passive pixels spectral responses. The third section describes the design of the readout board for active mini-matrices and their experimental characterization. The design of the readout board for passive pixels is not described since it hasn't been the object of this work.

4.1 Overview of the experimental Set-Up

Figure 4.1 shows the schematics of the experimental set-up for the characterization of the designed TFD active mini-matrices and passive pixels. The light source is a Dolan Jenner Mi150 (CCT of 3200 K) with an internal infrared filter. Its broad spectrum emitted light enters a monochromator (a Czerny-Turner Digikrm DK240), which, thanks to its diffraction pattern, selects and transmits a specific wavelength. To solve the problem of the beam divergence, caused by the small slit aperture of the monochromator, a convergent lens in interposed between the monochromator and the sensor. This lens can be sub-millimetrically translated back and forward to correctly focus the beam on the sensor. A blue filter (80A Hoya's blue filter) is added to the optical chain to compensate the light source unbalance toward long wavelengths. This is necessary, during the monochromator sweep from 400nm to 700nm, to avoid the saturation of the red channel at long wavelengths while at short

wavelengths the blue channel signal is still really low (and hence noisy). The devices on chip are wire bonded to a board which reads the output signals, and whose discrete components provide the anodes biasing voltages and the reset reference signal.

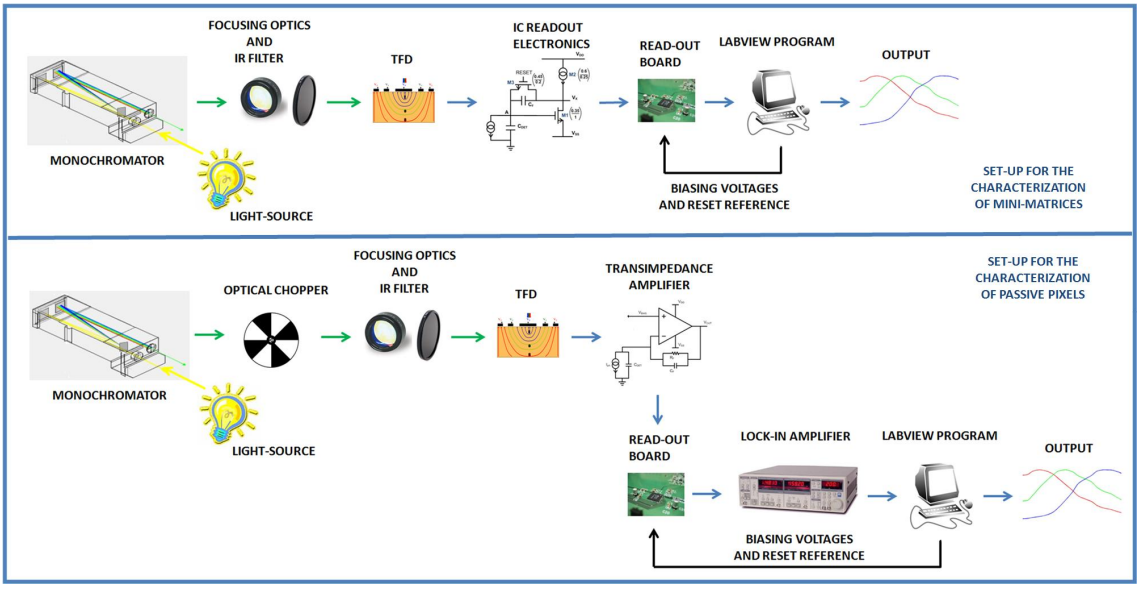

Figure 4.1 *Schematic of the Experimental Set-Up for the Characterization of Active Mini-matrices (upper image) and of Passive Pixels (lower image*

For the active pixels, the light incident on the TFD generates photocharges which are collected at the different anodes and amplified by the integrated charge preamplifier described in chapter 3 (figure 3.7). For the passive pixels the photocurrent is converted into an output voltage by means of the discrete components transimpedance amplifier in figure 4.2. The anode biasing is implemented by applying to the positive input of the operational amplifier the required biasing voltage, which is forced at the negative input by a negative feedback loop. Since for passive pixels no amplification is performed at pixel level, the 1/f noise can't be neglected. For this reason light is modulated with an optical chopper before being focused by the lens, and the signal at the output of the transimpedance amplifier is sent to a lock-in amplifier, which demodulates and recovers the signal, cleared from the pink noise.

For both active and passive pixels the measurements are automated through *Labview* routines, which set the TFD anode voltages through an analog voltage generator, drive the monochromator from 400nm to 700nm with 10nm steps, and

sample the output signals. In particular, for the characterization of mini-matrices, the analog voltage generator is a *Measurement Computing* USB 3105, while the DAQ acquisition board is a PCI DAS-4020 from *Measurement Computing*. The light source spectral power distribution has been initially characterized with a reference calibrated Silicon photodiode (*Thorlabs* FDS100).

Symmetrical and Asymmetrical 3 colors TFD passive pixels have been characterized in terms of their spectral sensitivity and tunability. To compare the TFD spectral response with CFA's, a spectral property which is independent from the

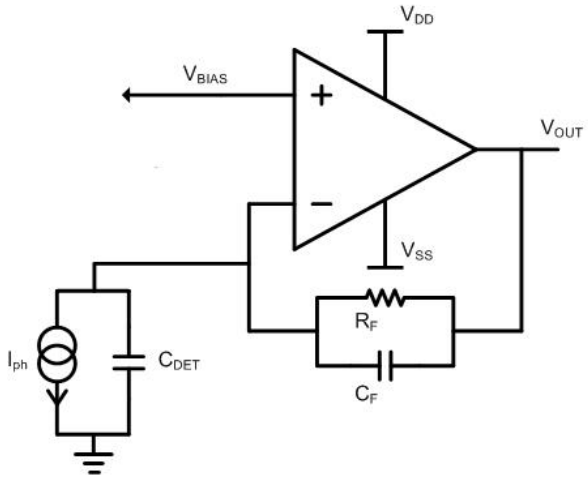

Figure 4.2 *Biasing/readout circuit for passive pixels: the photocurrent is converted into an output voltage by means of a discrete components transimpedance amplifier. The anode biasing is implemented by applying the required biasing voltage to the positive input of the operational amplifier, which is forced at the negative input by a negative feedback loop.*

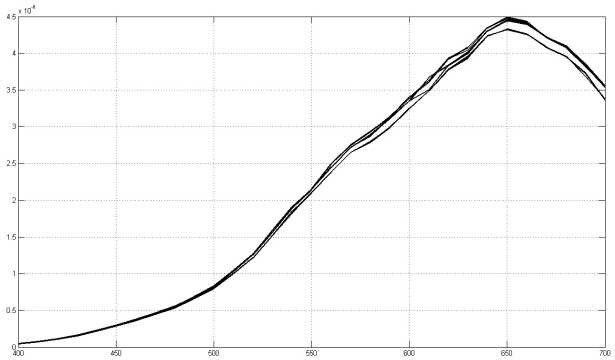

Figure 4.3 *Source spectral emittance in the visible spectrum measured by means of the calibrated silicon photodiode. The different curves refer to different subsequent acquisitions.*

illuminant and the technology is needed. For this purpose the spectral transmittance of the TFD "equivalent filters", which are defined as the ratio between the photocurrent measured at the correspondent anode at every wavelength and the total photocurrent that would be measured at the same wavelength on a white pixel, have been evaluated. The photocurrent at the output of each color channel has been measured for wavelengths between 400 nm and 700 nm with steps of 10 nm. To evaluate the detector spectral tunability, the equivalent filters have been measured for many different biasing conditions. For comparison, figure 4.4 shows the spectral responses obtained in the previous run for different tunings: due to the illumination of the whole pixel the three curves are highly unbalanced (note the vertical scale) and overlapped, with a strong prevalence of the red signal. As previously discussed, this usually results in high negative coefficients of the CCM and thus in bad color reconstruction due to a low signal to noise ratio.

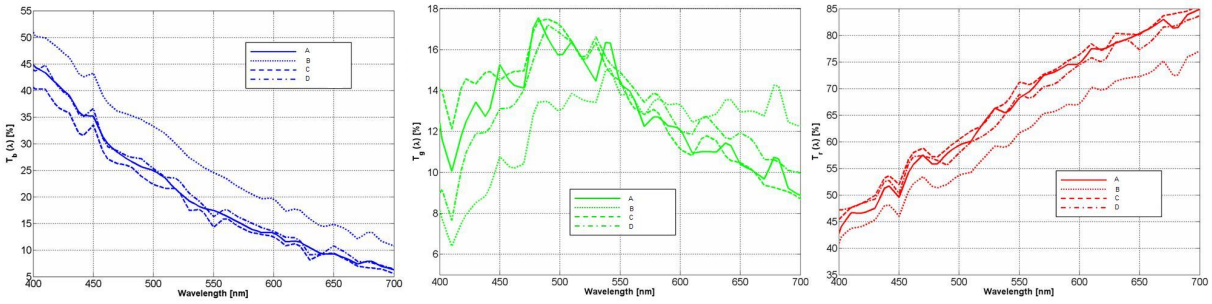

Figure 4.4 *Equivalent Filters obtained in the previous run for different tunings*

For this new design, to obtain sharper filters the illumination window has been optimized by finding a trade off between good color reconstruction, spectral tunability and Fill Factor (as described in 2.3.1.1). Figure 4.5 shows the experimental spectral responses of the new asymmetrical TFD pixel: they well match the equivalent filters simulated in Dessis for similar biasing conditions, and they are far sharper and more balanced than the ones obtained in the past run. The main difference with respect to the simulations is the level of the red anode response, which appears higher than expected (approximately %35). This mismatch can be well appreciated in the blue wavelength range, where the signal should be almost nul. The same problem has been encountered for passive symmetrical pixels and for mini-matrices. The possible explanations of this phenomenon are discussed in the next section.

To test the TFD performances in High Color Accuracy mode, the CCM and the color error have been evaluated using 5 and 6 spectral responses (figure 4.6). With

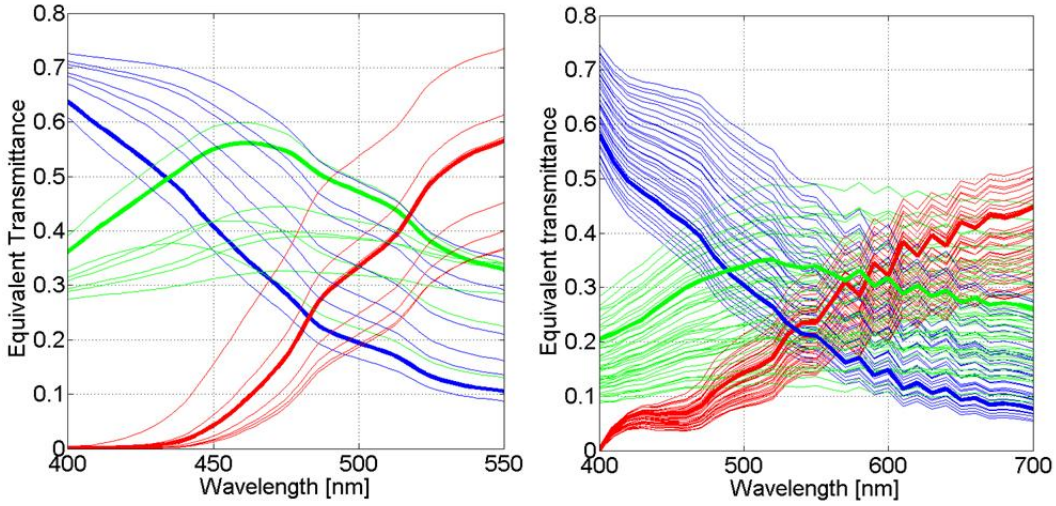

Figure 4.5 *Simulated (left) and Experimental (right) equivalent filters of the three color channels of a TFD passive pixel: the experimental results well match simulations, except for the red channel response at short wavelengths, which is higher than expected.*

six responses a potentially very good $\Delta E_{a^*,b^*}$ can be obtained (< 1.1). However the CCM negative coefficients are too high, resulting in a quite large noise propagation. On the other hand, using 5 spectral responses can give a similar tristimulus reconstruction (ΔEa^*b^*=1.8) with acceptable noise performances. Figure 4.7 shows a comparative analysis of the experimental color performances obtained with 3 (standard RGB mode with IR filter) and 5 (HCA mode) responses. The left images shows the coordinates of the colors of the scene in the xy chromaticity diagram, together with the reconstructed coordinates in RGB mode and HCA mode. The right image shows the reconstruction error for the different colors in the $L^*a^*b^*$ perceptual color space.

From a spectral tunability point of view, good results were obtained, matching the range of the simulations. Figure 4.5 shows an example of the equivalent filters obtained for different biasing conditions. The green channel is the one that showed the best tunability, and its spectral sensitivity peak could be shifted of more than 100nm. Figure 4.8 shows the comparison between the tunability obtained in this run and the one obtained in the previous run.

The CCM and the color reconstruction error relative to the different sets of experimental equivalent filters have been calculated with ISET. The best set of equivalent filters has been compared with the response of other color sensors on the market. The results of this comparative study are presented in figure 4.9

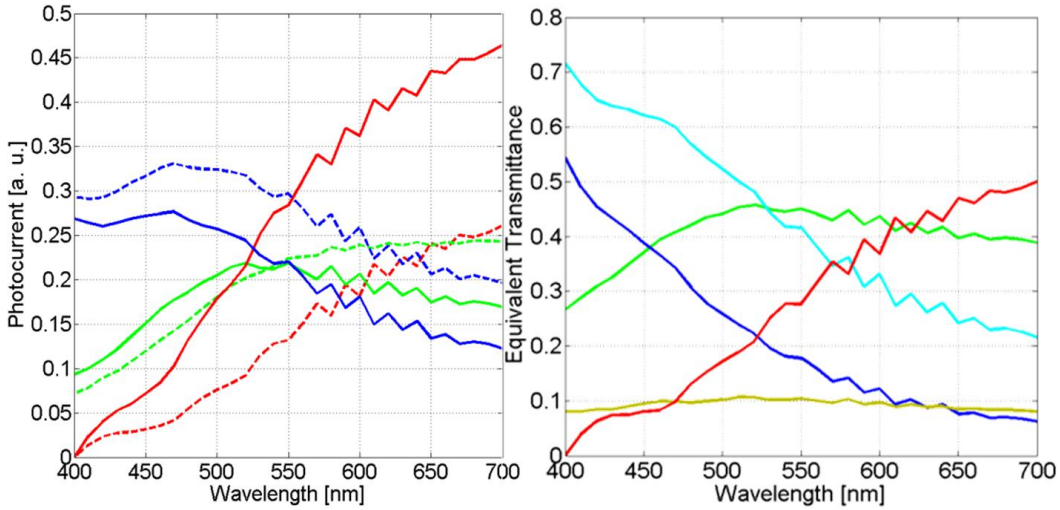

Figure 4.6 *Spectral responses used to evaluate the color performances in HCA mode using 6 (left) and 5 (right) spectral responses*

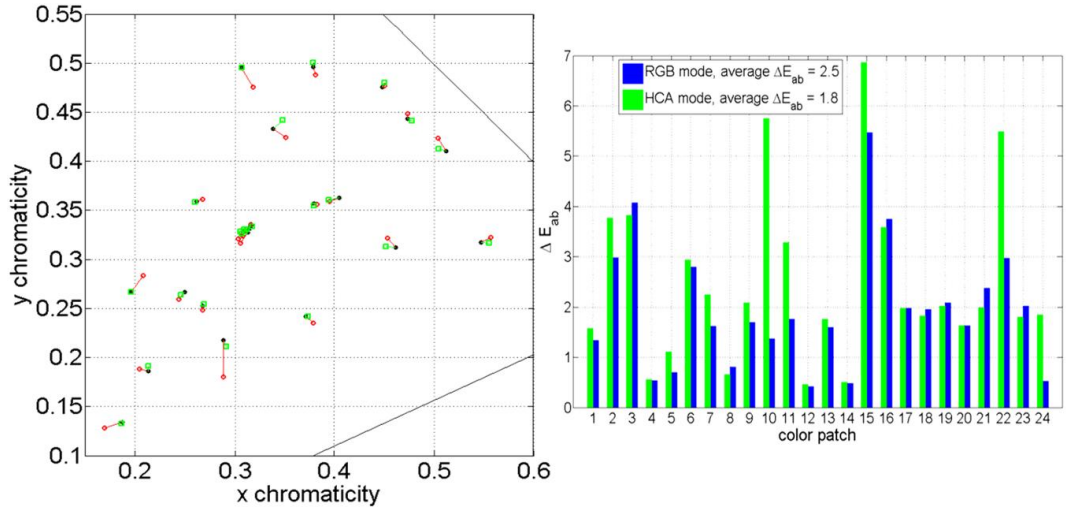

Figure 4.7 *Comparative study of the color performances in terms of the ΔEa^*b^* error for a MCC acquired in standard RGB mode + IR filter and HCA mode using 5 spectral responses. The left images shows the coordinates of the colors in the scene in the xy chromaticity diagram, together with the xy coordinates reconstructed in RGB mode and HCA mode. The right image shows the color reconstruction error, obtained for the different colors in the two acquisition modes, in the $L^*a^*b^*$ perceptual color space.*

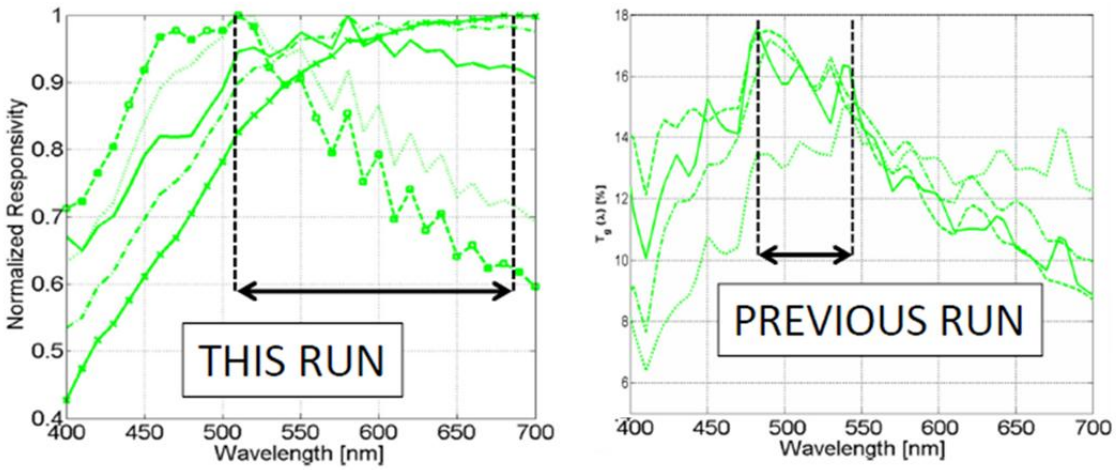

Figure 4.8 *Comparison between the experimental tuning of the equivalent filters obtained in this run and in the previous run. The maximum obtained tuning is more than 100nm, which is better than expected from the simulations.*

4.2 Possible explanations of the red channel offset

In all the tested devices, the red signal is higher than what expected from the simulations. Three possible explanations of this phenomenon are proposed in this section.

The first hypothesis is the presence of multiple reflections between the metals that cover the non active areas of the pixel (figure 4.10). These reflections result in a broader equivalent illumination window, which means that light is absorbed in those regions where the electric field profile doesn't enable good color separation. Hence, the red anodes, which collect from a larger volume, would also collect charges which are photogenerated by short wavelength photons, causing an increase of the red signal toward those wavelengths. However, for the red signal to be 35% higher than predicted, at least 1/3-1/2 of the light should reach the pixel with a certain angle, as shown in the figure, while in practice it is almost orthogonal to the pixel surface. A ray-tracing simulation should be implemented to obtain a more quantitative understanding of the impact of this hypothesis.

A second possible explanation could be the photogeneration of charges in a strip between the pixel border and the guard ring, in those areas which haven't been covered with any metal. In fact, unlike for the past run, metal filling wasn't available for this technology at the time of the design. The red anode is the one that delimits the majority of the pixel perimeter, hence it is the most likely to collect

SENSOR	Equivalent Filters Transmittance	?E_ab	Obtained with an IR filter	CCM Most Negative Coefficient
Nikon CFA	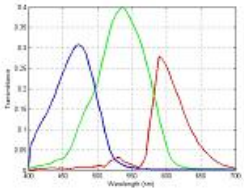	1.1	YES	-0.32
Foveon X3	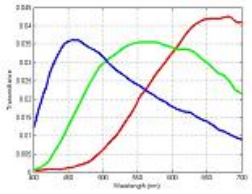	2.72	YES 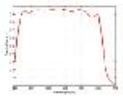	-2.45
Simulated symmetrical TFD	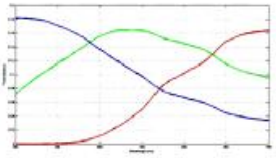	3.03	NO	-2.22
Simulated Asymmetrical TFD	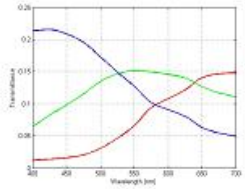	3	NO	-3.07
Symmetrical TFD	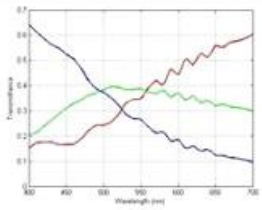	3.37	NO	-2.90
		2.6	YES 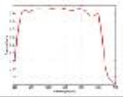	-2.86
TFA	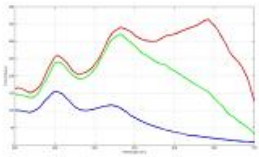	3.56	NO	-4.32
		2.92	YES 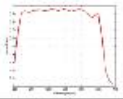	-4.19

Figure 4.9 *Comparison between the TFD and other color sensors characteristics in terms of the equivalent filters, the color error and the CCM. By adding an additional IR digital filter better color performances can be obtained for the TFD.*

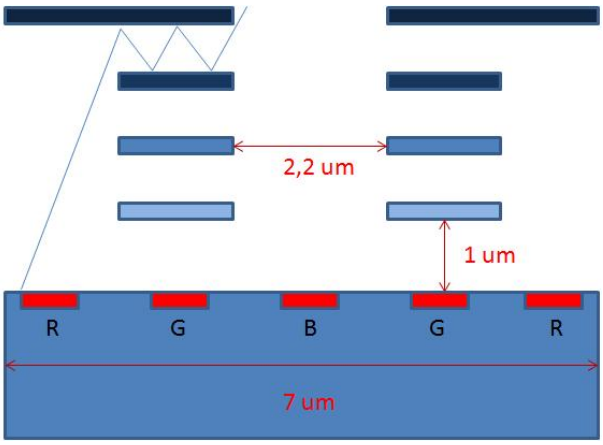

Figure 4.10 *Possible explanation of the blue offset of the red channel: multiple light refractions result in a larger optical window, and thus light is absorbed in a region where the electric field profile is not suitable for color separation.*

charges photogenerated outside of the pixel. Under the hypothesis that half of the photocharges generated in this strip is collected by the red anode and half by the guard ring, and since the ratio between half of the external area and the active area is around 9.1% for the symmetrical pixel and 9.3% for the asymmetrical pixel, the red signal should be 9% higher in the whole visible range than predicted (while it is almost 36% higher). This additional light contribute has been simulated in Dessis, maintaining the proportions between the active areas and the illuminated non active areas. The results are presented in figure 4.11: an increase of the red signal is indeed observed, even if the curves still differ from the experimental ones.

A third possible contribution could be due to charges photogenerated in the rest of the chip, which diffuse in the substrate and reach the pixel. The red anode collects more of these additional photocharges since it goes deeper in the device. From technological information given by the foundry, a diffusion length of roughly $170\mu m$ has been estimated. Hence this hypothesis seems to be the most plausible one.

To evaluate the well foundation of this last hypothesis, the output slit dimensions of the monochromator have been reduced, to illuminate the smallest area possible external to the pixel. The photocurrents measured for different slit dimensions are shown in figure 4.12. Figure 4.13 shows the measured quantum efficiencies (obtained by dividing the photocurrents by the source spectral emittance) correspondent to the smallest output slit: the channel responses are more balanced and the red signal is reduced, but not yet at the simulations level.

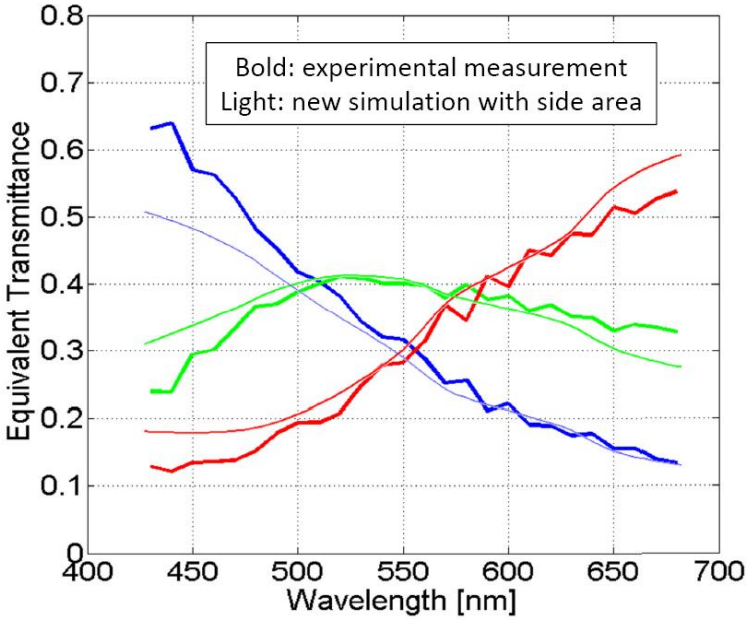

Figure 4.11 *Simulated equivalent filters including the illumination of side areas. As in the experimental measurements, an increased of the red signal toward short wavelength is observed.*

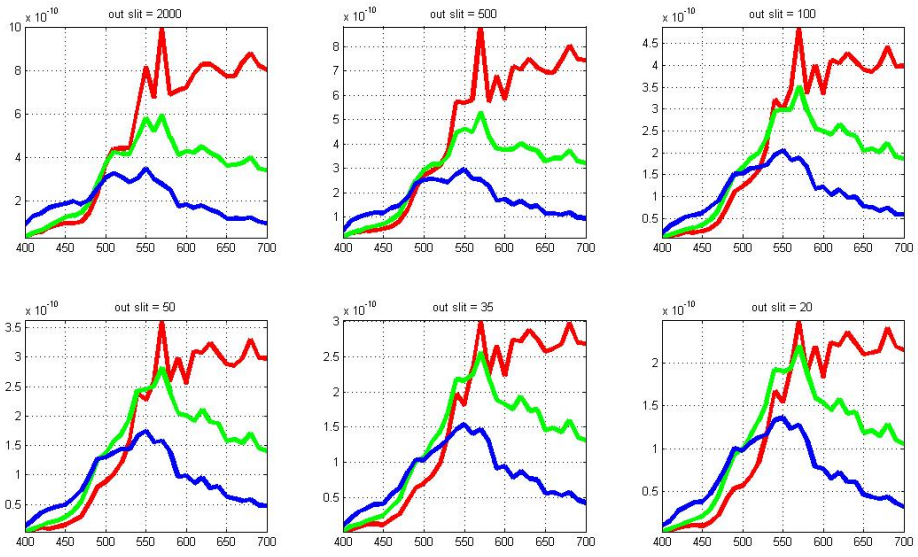

Figure 4.12 *Photocurrents of an asymmetrical TFD passive pixels obtained with the same biasing conditions and changing the monochromator output slit.*

As a last attempt to understand the phenomenon, the non active areas of the chip will be covered with gold film as shown in figure 4.14. Measurements are not yet available.

4.3 Active Mini-matrices Readout-Board Design and Characterization

For two out of the four designed mini-matrices, the output signals of the color channels are amplified and readout with the integrated electronics that has been described in section 3.3.1. For one of these two mini-matrix, the correct high and low voltage levels of the reset signals of the three color channels are provided by integrated voltage level translators (section 3.3.1.5), while for the other mini-matrix they are provided by discrete component circuits, which implement the same function, that have been designed on an external board to which the devices are wire bonded. This board is also used to readout the output signals and to provide the anodes biasing voltages. The 2×2 mini-matrices with integrated reset level translators have been tested and characterized. The design of the readout board will be described and afterwards experimental data will be presented and discussed.

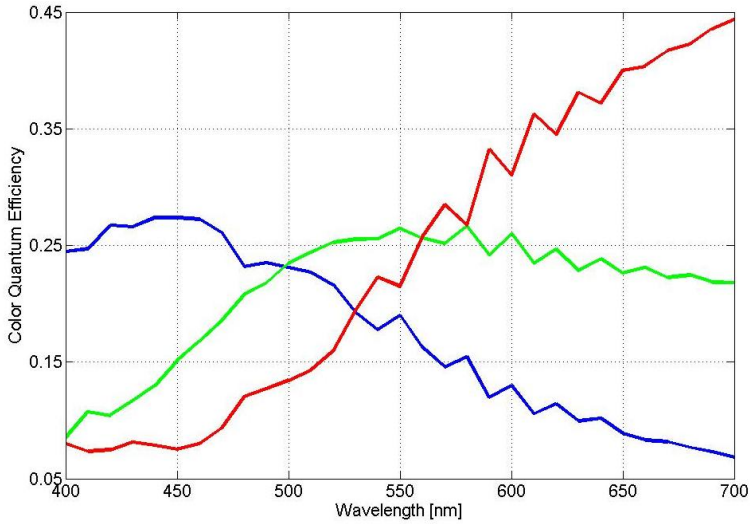

Figure 4.13 *Color channels quantum efficiency of an asymmetrical TFD measured with the smallest possible monochromator output slit.*

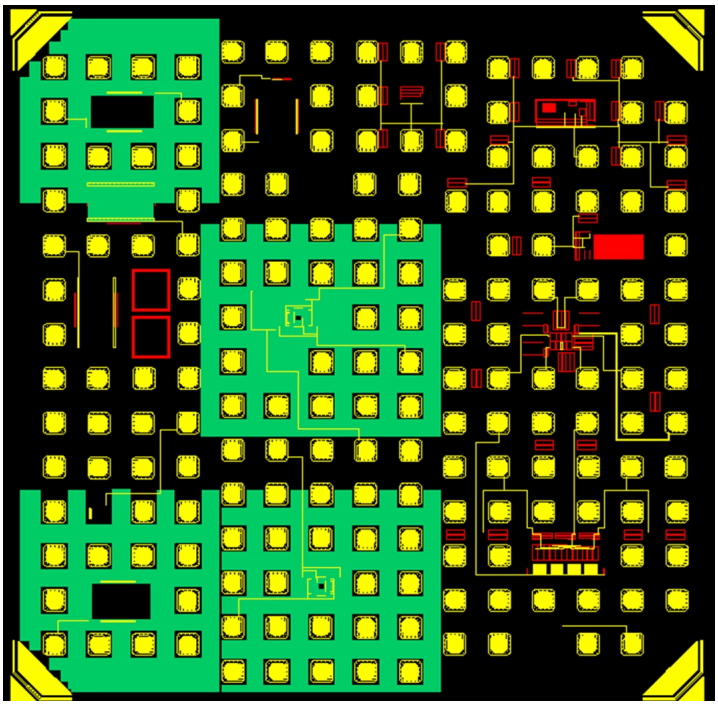

Figure 4.14 *the non active areas of the chip will be covered with gold film to understand if the additional contribute to the red signal is due to charges photogenerated outside of the pixel*

4.4 External Board for the Polarization and the Readout of Mini-matrices

Figure 4.15 shows a schematic of the board for the polarization and the readout of mini-matrices. The integrated emitter follower at the output of each color channel is biased by means of a stabilized current generator which will be described later in this section. Only three output signals can be read and transmitted to the *Labview* program at the same time due to the limited number of inputs of the digital acquisition board. The anodes biasing voltages are set from a *Labview* routine and are supplied by means of a 16-bit analog output generator (MC USB 3105). The LSB is $\frac{10V}{2^{16}} = 0.5fV$, which is sufficient for our purposes. The reset signal, supplied by a waveform generator, has a span of 1.8V and a reset frequency which depends on the required integration time.

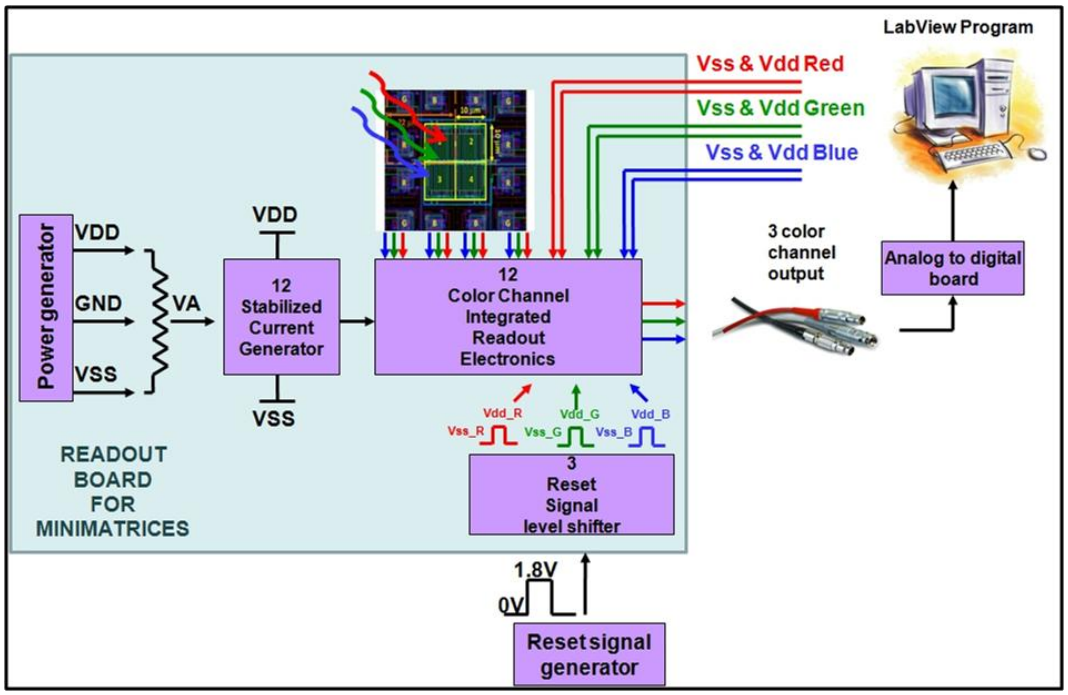

Figure 4.15 *Schematic of the External Readout Board for the readout of mini-matrices.*

4.4.1 External Voltage Level Translator

External voltage level translators (figure 4.16) have been implemented to provide the reset signals with the correct low and high levels to the readout circuits of the mini-matrix which has no integrated level shifter. The working principle is the same as the one of the integrated circuit described in section 3.3.1.5. There are three level shifters shared by the four pixels, one for each color. The input reset signal is provided by an external waveform generator and is a rectangular wave that goes between 0V and 1.8V. The reset signal is transmitted to the input of an inverter by means of a 100nF discrete capacitor. To bias the input voltage of the inverter, a resistor of $2M\Omega$ has been used. The value of the capacitance and the resistance have been chosen for the RC time constant to be high enough for the input voltage to be approximately constant during the reset time. For $C = 100nF$ and $R = 2M\Omega$ the resulting RC time constant is $\tau = R \cdot C = 200ms$, which is far longer than the integration times that have been used for the TFD characterization. The inverters are SN74AUC1G04 from Texas Instruments, and are biased with the same VSS and VDD provided to the integrated readout circuits of each color channel. At the output of the inverter the reset signal is still a rectangular waveform with a span

of 1.8V, but the high and low voltages are the VSS and VDD of the corresponding color channel readout circuit.

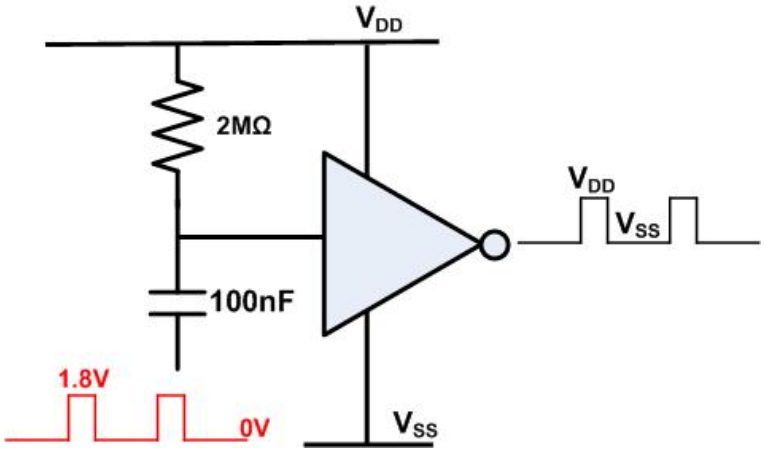

Figure 4.16 *Discrete Reset Voltage Level Shifter*

4.4.2 Stabilized Current Generators

The biasing current of the output stage of the integrated readout circuit is realized by means of a BJT in a negative feedback loop (figure 4.17). This circuit guarantees an output impedance of more than $9G\Omega$, which makes it invulnerable to fluctuations of the output signal of the integrated circuit. The BJT is a BC849B (Infineon Technologies) [39], while the Operational Amplifier is a TLV2262 by Texas Instruments [40]. Thanks to the negative feedback loop the voltage drop between the negative and the positive inputs of the Opamp tends to zero. Hence the voltage drop across the resistance is equal to $V_A - V_{SS}$ and, according to Ohm's law, the current that flows in the resistance is $I_R = I_E = \frac{V_A - V_{SS}}{R}$. The output current is $I_{pol} = I_C = I_R \times \frac{\beta}{1+\beta}$.

4.4.2.1 Output Resistance

As it has been discussed in Chapter 2, the output resistance of the current generator must be high for the current generator to be stable, and for the buffer to have a unity transfer gain. Since this circuit has a negative feedback loop, the open loop output resistance ${R^0}_{out}$ is increased by a factor $[1 - G_{loop}(0)]$:

$$R_{out} = {R^0}_{out}[1 - Gloop(0)] \tag{4.1}$$

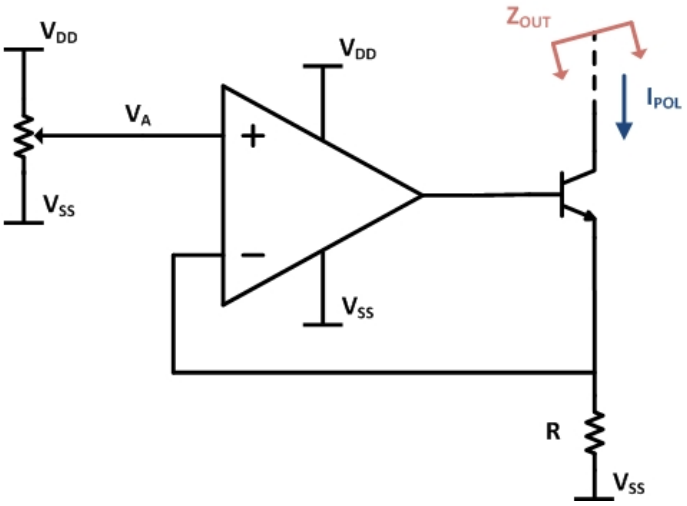

Figure 4.17 *Current Generator for the biasing of the IC output stage*

$R^0{}_{out}$ is the resistance at the collector of a bipolar transitor in degenerated emmitter configuration, hence it can be calcluated as:

$$R^0{}_{out} = R//R^*{}_b + r_0[1 + \frac{\beta R}{1 + R^*{}_b}] \tag{4.2}$$

$$R^*{}_b = R_b + \frac{\beta}{gm} \tag{4.3}$$

Where R_b is the base resistance, β is the common emitter current gain, g_m is the transconductance and r_0 is the collector resistance of the bipolar transistor. For $I_C = 1\mu A$, the BJT transconductance and gain factor are respectively $g_{mBJT} = I/V_{th} \approx 40\mu A/V$ and $\beta_{BJT} \approx 240$. Since $R_b < 1K\Omega$ and $R = 100k$, then $R^*{}_b \approx \frac{\beta}{gm} = 6M\Omega >> R$. Hence $R^0{}_{out}$ can then be calculated as:

$$R^0{}_{out} \approx R + r_0[1 + gmR] = 150k\Omega \tag{4.4}$$

The value of r_0 has been estimated with PSPICE simulations and is around $30k\Omega$.

4.4.2.2 Loop Gain

The gain of the negative loop can be calculated as:

$$G_{loop}(0) = -A(0)\frac{\beta R}{\frac{\beta}{gm} + \beta R} = -A(0)\frac{R}{\frac{1}{gm} + R} \approx -A(0) \cdot 0.8 = -64000 \tag{4.5}$$

Being $A(0) = 8 \times 10^4$ the operational amplifier DC gain, and $R = 100k\Omega$ the resistor in the feedback loop, the DC loop gain magnitude is: $\mid G_{loop} \mid \approx 96dB$. Hence, the close loop output resistance of this circuit is:

$$R_{out} = R^0{}_{out}(1 - G_{loop}(0)) \approx 9.6G\Omega \tag{4.6}$$

This value is fairly larger than the worse case resistance used to size the transistor of the integrated emitter follower stage. Hence the transfer gain for the buffer is approximately 1.

The layout of the top and the bottom of the PCB are presented in figure 4.18. The circuit simulation and the layout have been done with Orcad software.

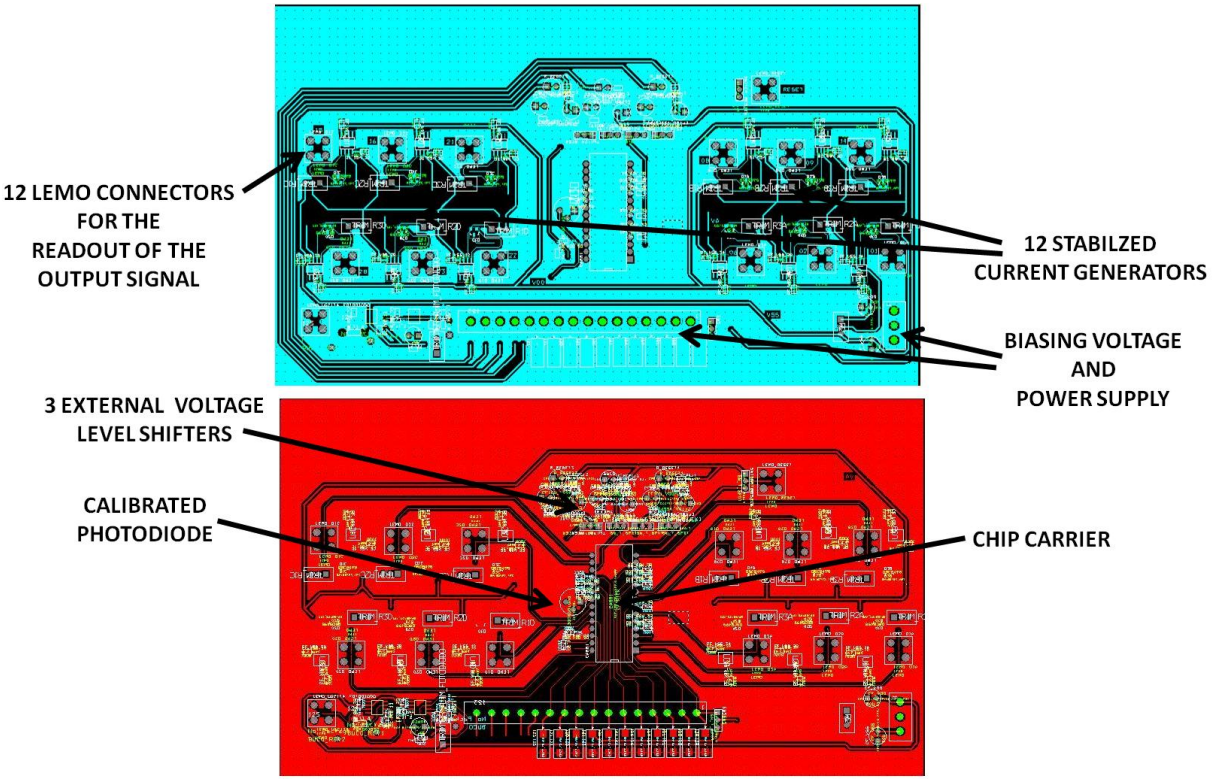

Figure 4.18 *Top (in Blue) and Bottom (in Red) View of the layout of the readout board for minimatrices*

4.5 Mini-matrices Characterization

The Minimatrices described in chapter 3 have been characterized in terms of noise, Dynamic Range and spectral responses.

4.5.1 Noise contributions in mini-matrices

4.5.1.1 Reset noise

The reset noise contribution is mainly due to the KTC noise on the feedback capacitance. In fact, the detector capacitance is between ground and a virtual ground, and the parasitic capacitance of the transistor can be neglected. Under these hypothesis the theoretical reset noise contribution in terms of V_{rms} can be calculates as

$$\sigma_{KTC} = \sqrt{\frac{KT}{C_F}} \approx 390\mu V_{rms} \tag{4.7}$$

The measured value is $230\mu\ V_{rms}$, in fairly good agreement with the theoretical one.

4.5.1.2 Dark current

Figure 4.19 shows the waveforms at the output of a TFD color channel, with the anode biased at 3V, in four different lighting conditions. The black waveform corresponds to dark current integration.

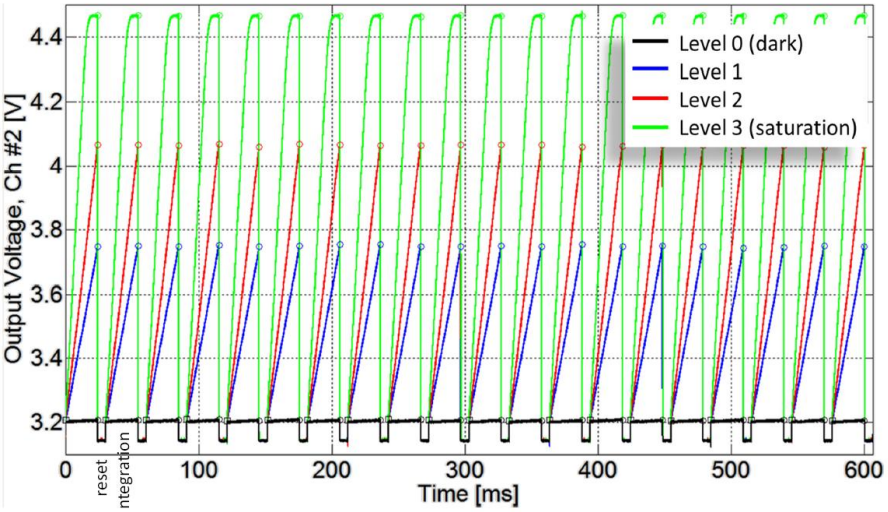

Figure 4.19 *Example of output waveforms for a TFD channel with the anode biased around 3 V in four different lighting conditions*

The dark current measured at the 3 anodes is different, and in particular the dark noise at the red channel is almost the double of the one at the green channel, which is in turn the double of the dark current measured at the blue channel. These results are in line with what was expected, since the red channels collects from a larger volume than the other two. The total charge collected by the three anodes is around $6 \cdot 10^{-17}$ C, hence for the an integration time of 3.03 ms (33Hz reset frequency), the resulting dark current density is 13 $\frac{nA}{cm^2}$, which is consistent with the values provided by the foundry (figure 4.20).

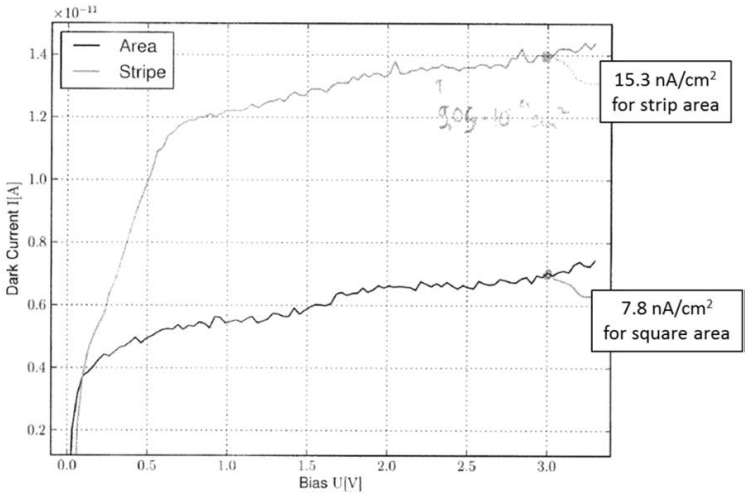

Figure 4.20 *Dark current density technological specifications*

4.5.1.3 FPN

In mini-matrices the Fixed Patter Noise is due to small differences among pixels in terms of their border geometry and of their readout circuits. To measure the FPN, the three photocurrents of each pixel have been measured and normalized with the sum of the three photocurrents corresponding to the same color channel (Figure 4.21). To give an example the blu photocurrent of pixel A has been divided by the sum of the blu photocurrent of pixel A, B and C of the mini-matrix. The normalization is necessary to appreciate the difference between the signals, since their shape is mainly determined by the light source spectral emittance. If the FPN was null, the three normalized signals would be equal to 0.33 (which means that the three blu photocurrent would be identical). The measured values are between 0.32 and 0.35. Hence good repeatability was obtained. An important contribution to this error seems to come from the digital acquisition board.

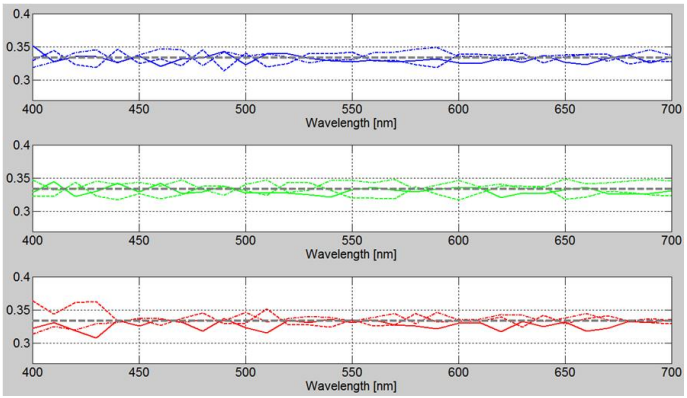

Figure 4.21 *FPN evaluation: each figure shows the normalized photocurrents for one specific color channel measured for three different pixels in the same biasing conditions, normalized by the sum of the three currents.*

4.5.2 Linearity and Dynamic Range

The Dynamic range is calculated as the ratio between the maximum measurable signal (limited by linearity saturation requirements) and the minimum measurable signal (which corresponds to a Signal to Noise Ratio equal to 1). To evaluate the linearity of the sensor, the saturation point has been defined, as suggested by Nakamura in [7], as the point where the linearity error reaches 5% (figure 4.22).

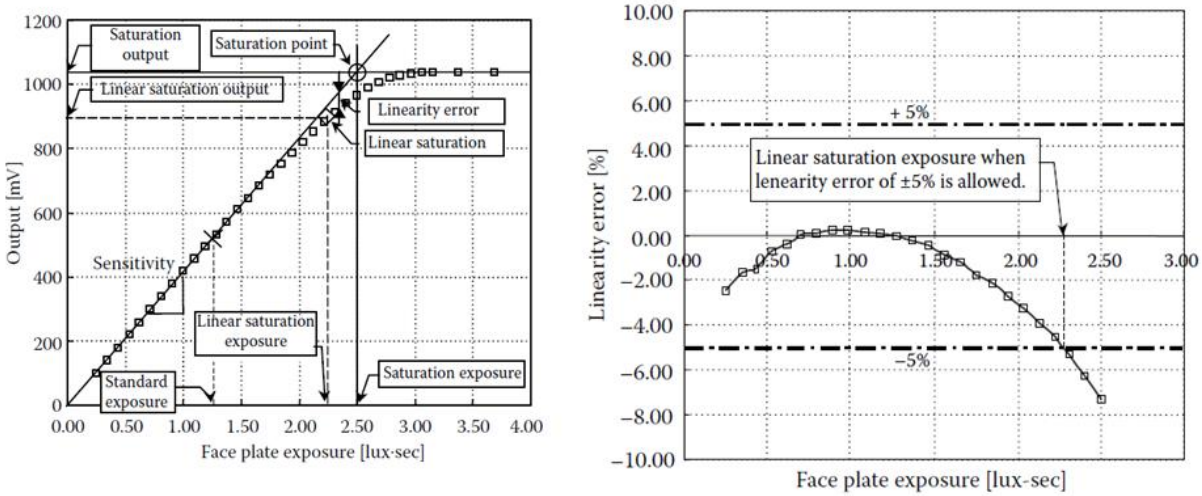

Figure 4.22 *Linearity range evaluation as defined in [7]*

Figure 4.23 shows light integration for one color channel at three different light intensities. The linear interpolation curves of the three currents have been estimated on the voltage range showed by the black arrow in the figure. The corresponding non

linearity error for the three curves is shown in figure 4.24. The maximum voltage sweep corresponding to 5‘% non linearity error is around 1.2V (indicated by the blue arrow in figure 4.23).

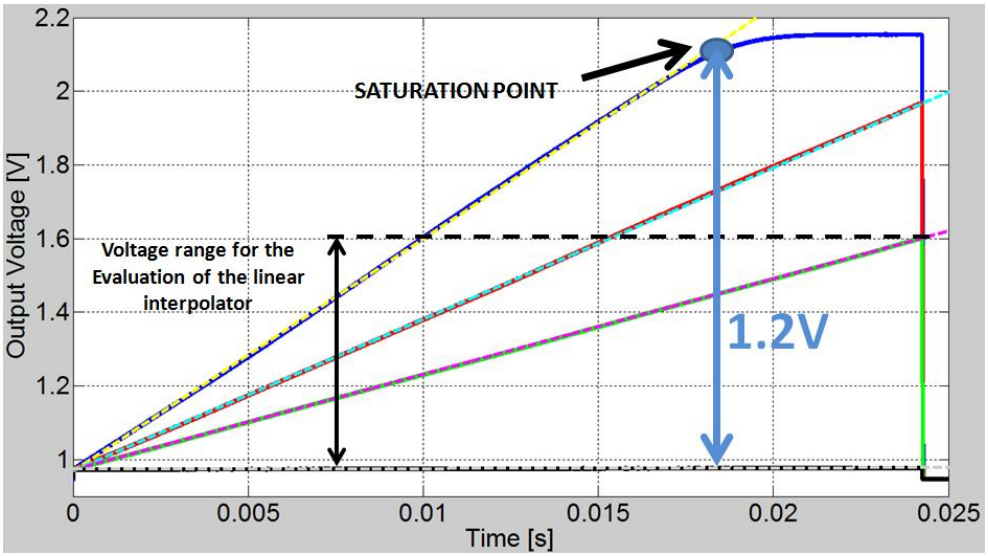

Figure 4.23 *Light integration for one color channel at three different light intensities. The linear interpolation curves of the three currents have been calculated on the voltage range showed by the black arrow in the figure*

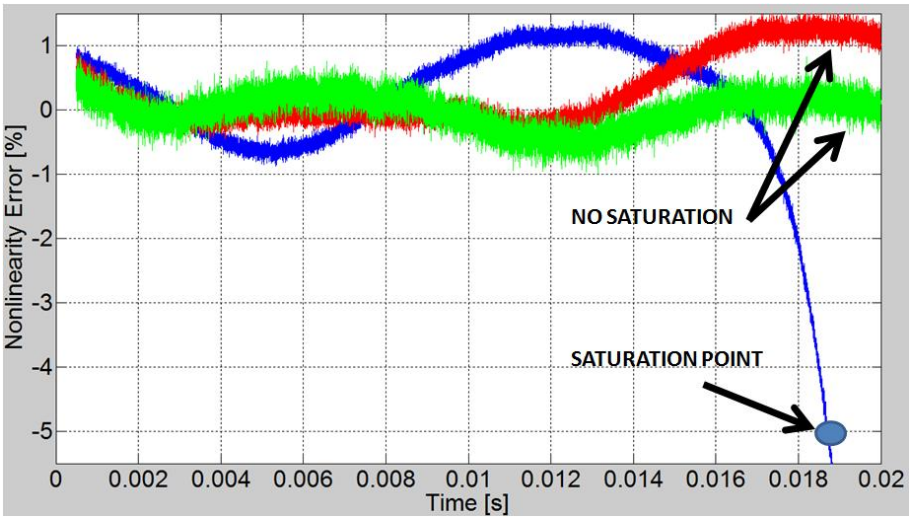

Figure 4.24 *Linearity error for the curves in figure 4.23*

The two main noise contributions are the KTC noise and the shot noise of the signal and the dark current. To calculate the minimum measurable signal the photocurrent is supposed smaller than the dark current, hence the voltage rms noise

can be calculated as:

$$V_{min} = \sqrt{{\sigma_V}^2} = \sqrt{{\sigma_{VKTC}}^2 + 2qi_{dark}t_{int}/{C_F}^2} \tag{4.8}$$

For low integrations times the shot noise contribution is negligible with respect to the reset noise, hence the minimum measurable signal is around $230\mu V_{rms}$ and the obtained dynamic range is

$$DR = 20log_{10}\frac{V_{max}}{V_{min}} \approx 20log_{10}\frac{1.2V}{230\mu V} = 74.4dB \approx 75dB \tag{4.9}$$

For integration times $>$ 20ms the shot noise becomes non negligible and the DR starts degradating.

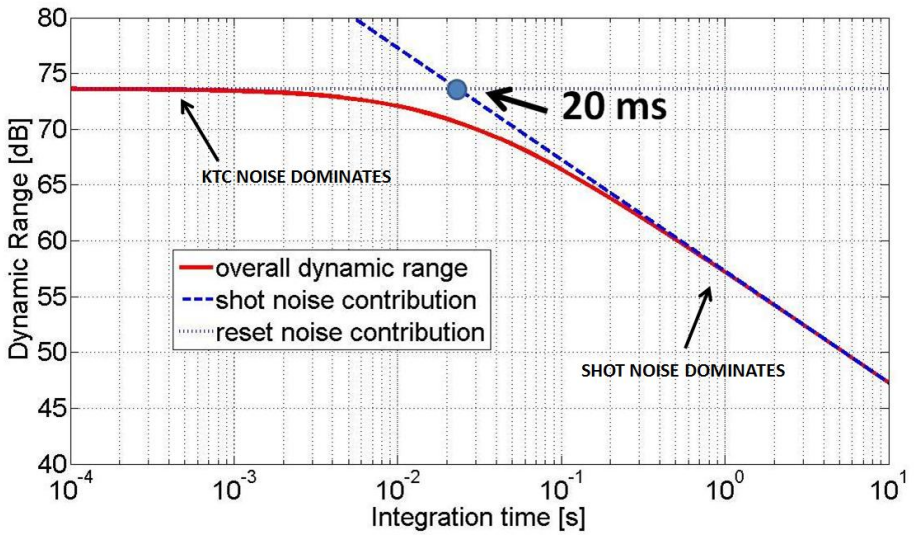

Figure 4.25 *TFD Dinamic Range: for a low integration time the DR is limited by the reset noise, hence is independent from the integration time. For longer integration times the shot noise becomes prevalent and the DR starts worsening.*

Chapter 5

Future Developments and Conclusions

This Master's thesis work regarded the simulation, design and characterization of a filter-less and tunable optical sensor for digital imaging, called Transverse Field Detector. The device has been optimized to obtain the maximum tunability of its spectral responses, while maintaining good RGB color reconstruction performances and an acceptable fill factor (22% for active mini-matrices and between 31% and 49% for passive structures).

The spectral responsivity of passive pixels showed a consistent improvement with respect to the past design, obtaining well balanced spectral sensitivities and an error in the CIE 1976 $L^*a^*b^*$ perceptual color space around 3. The level of the red signal toward short wavelength in all the tested devices is higher than what expected from the simulations. Possible explanation of the phenomenon have been discussed, but it is still an open issue. Further measurements will follow to evaluate if the additional signal is due to charged photogenerated outside of the pixels. In the next design a technology with metal fillings will be used to avoid photogeneration in non active areas.

The electrical tunability of the device has confirmed what was expected from the simulations, with a spectral shift of the green channel peak of over 100nm. Good color performances, both in terms of the ΔEa^*b^* error and of the CCM coefficients, have been obtained in High Color Accuracy mode by using 5 spectral responses. Specific algorithms still need to be implemented to evaluate the suitability for Multispectral imaging of the TFD experimental spectral responses, but this

work demonstrated the feasibility of the implementation of a multispectral analyzer using the TFD. Some software development is being carried on at the Universidad de Granada.

The integrated readout circuit for active TFD pixels proved to work well, with a dynamic range of 75dB and a low FPN. The main noise contributions are the KTC noise on the feedback capacitance at short integration times and the shot noise at long integration times. Given its performances and its simplicity, this circuit could be used for the readout of a larger matrix.

Much work has still to be done for the development of a full CMOS TFD sensor. The next step will be the design of a larger matrix, aiming to a maximization of the Fill Factor. Since in this run, the width of the anode implants and the size of the transistor in the integrated electronics weren't chosen the minimum allowed ones, to safely minimize differences between pixels caused by the process variance, some improvements in the FF can be easily obtained by designing both the pixels and the electronics with minimum dimensions. The FF can also be increased by smartly rearranging the pixels and the readout electronics in the matrix. An example of such a smart arrangement is shown in figure 5.1, where the pixels are placed in the matrix in such a way that the n-Mos transistors of the same color channel for different pixels share the same isolated n-well. The effect of pixel scaling will be investigated to reduce costs, but it won't affect the FF, since also the active areas would be scaled.

From a software point of view, much work has still to be done, developing algorithms for color reconstruction and multispectral imaging, specifically conceived for the TFD.

In conclusion the results of this thesis are promising, and this work has been a good proof concept for the development of the TFD as 'smart" pixel for both consumer and scientific applications. Its color performances are not yet at the level of CFAs, but the device isn't conceived to provide an alternative to CFA, rather to open the door to new applications, which can't be implemented with the sensors that are today available on the market.

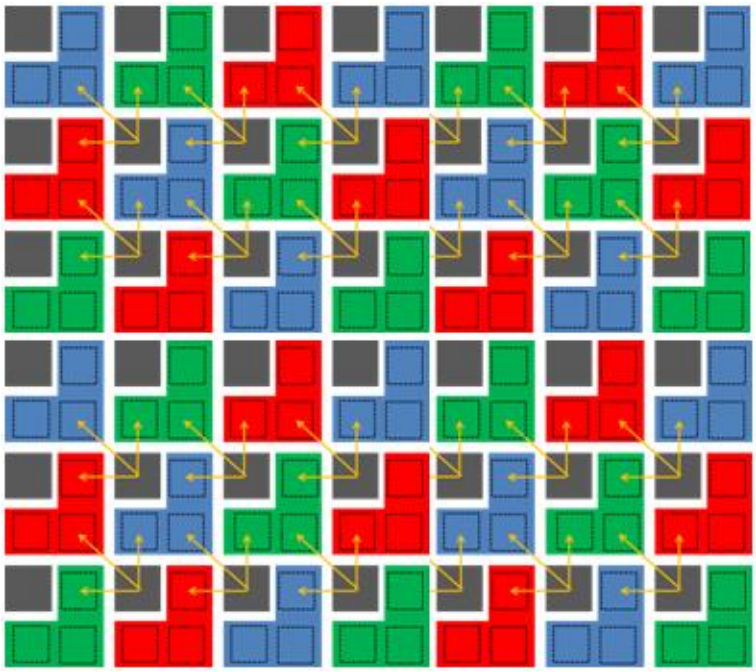

Figure 5.1 *Example of smart arrangement of pixels in the matrix to maximize the FF: the readout circuits for the same color channel of different pixels are placed close to eachothers, so that the n-Mos transistors can share the isolated n-well.*

Bibliography

[1] Paul M. Hubel Foveon Inc. USA. Foveon technology and the changing landscape of digital cameras. In *Thirteenth Color Imaging Conference: Color Science and Engineering Systems, Technologies, and Applications*, 2005.

[2] P. Rieve, M. Sommer, M. Wagner, and M. Bohm K. Seibel. a-si:h color imagers and colorimetry. *Journal of Non-Crystalline Solids*, 2000.

[3] Antonio Longoni, Federico Zaraga, Giacomo Langfelder, and Luca Bombelli. The transverse field detector (tfd): A novel color-sensitive cmos device. *IEEE Electron Device Letters*, 2008.

[4] Giacomo Langfelder, Antonio Longoni, Federico Zaraga, and Cesare Buffa. Color space tunability enabling adaptation to the scene in digital imaging. *IEEE Sensor Journal*, 2010.

[5] *Image System Evaluation ToolboxISET 2.0 UserManual*. Palo Alto, CA, Apr 2007.

[6] Lfoundry website. www.lfoundry.com.

[7] J. Nakamura. *Image Sensors and Signal Processing for Digital Still Cameras*. CRC Press, 2005.

[8] J.M Eder. *History of Photography*. Dover Publications, forth edition, 1978.

[9] Crawford William. *The Keepers of Light: A History and Working Guide to Early Photographic Processes*. Morgan & Morgan, 1979.

[10] James R. Janesick. *Scientific charge-coupled devices*. SPIE Press, 2001.

[11] Nobel prize website. url: http://www.nobelprize.org/.

[12] Micheal Bass. *Handbook of Optics Volume II - Devices, Measurements and Properties*. McGraw-Hill, second edition, 1995.

[13] Ohta Noboru, Alan R. Robertson, and Alan A. Robertson. *Colorimetry: fundamentals and applications*. John Wiley & Sons, Ltd, 2005.

[14] Radiometric and photometric characteristics of materials and their measurement - cie 038-1977.

[15] Shuxue Quan. *Evaluation and optimal Design of Spectral Sensitivities for Digital Color Imaging*. PhD thesis, Rochester Institute of Technology, 2002.

[16] S.O. Kasap. *Optoelectronics and Photonics: Principle and Practices*. Prentice Hall, 2001.

[17] Alex Byrne and David R. Hilbert. Color realism and color science. *Cambridge University Press*, 2003-2002.

[18] B.A Wandell. *Foundations of Vision*. Sinauer Assoc, 1995.

[19] *Color Imaging Processing*, 2005.

[20] Prof. Federico Zaraga. Slides of the courses of optoelectronic systems and digital imaging. url: http://risorse.dei.polimi.it/sensorlab/Education.html.

[21] N. Ohta. *Correspondence Between CIELAB and CIELUV Color Differences*, volume 2. Color Research and Application, 1977.

[22] Proc. SPIE-IS&T, editor. *Implementation of a multi-spectral color imaging device without Color Filter Array*, volume 7876, 2011.

[23] Roy S. Berns, Francisco H. Imai, Peter D. Burns, and Di-Y. Tzeng. Multi-spectral-based color reproduction research at the munsell color science laboratory. In *the Munsell Color Science Laboratory - Proc. SPIE 3409*, 1998.

[24] D. Y. Tzeng and R. S. Berns. A review of principal component analysis and its applications to color technology. *Color Research and Application*, 30, 2005.

[25] J. P. S. Parkkinen, J. Hallikainen, and T. Jaaskelainen. Characteristic spectra of munsell colors. *J. Opt. Soc.Am. A*, 6(2), 1989.

[26] Munsell book of color-matte finish collection, 1976.

[27] J. Park, M. Lee, M. D. Grossberg, and S. K. Nayar. Multispectral imaging using multiplexed illumination. In *IEEE International Conference on Computer Vision (ICCV)*, Oct 2007.

[28] NY) Nelson, Edward T. (Pittsford. Patent: Interline transfer ccd image sensing apparatus. http://www.freepatentsonline.com/5060245.html, October 1991.

[29] Bahadir K. Gunturk, John Glotzbach, Yucel Altunbasak, Ronald W. Schafer, and Russel M. Mersereau. Demosaicking: Color filter array interpolation. In *IEEE Signal Processing Magazine*, 2005.

[30] Astrosat website.

[31] Sony Corporation. Realization of natural color reproduction in digital still cameras, closer to the natural sight perception of the human eye. Sony technology development Article, July 2003.

[32] K. Martinez, J. Cupitt, and D. Saunders. High resolution colorimetric imaging of paintings. In *Proc. SPIE*, volume 1901, 1993.

[33] F. H. Imai and R. S. Berns. Spectral estimation using thricromatic digital cameras. In *Proc. International Symp. Multispectral Imaging and Color Reproduction for Digital Archives*, 1999.

[34] J. I. Park, M. H. Lee, M. D. Grossberg, and S. K. Nayar. Multispectral imaging using multiplexed illumination. In *IEEE International Conference on Computer Vision ICCV*, 2007.

[35] F. yasuma, T. Mitsunaga, D. Iso, and S. K. Nyar. Generalized assorted pixel camera: Postcapture control of resolution, dynamic range and spectrum. In *IEEE Transactions on Image Processing*, 2010.

[36] Giacomo Langfelder. Isolation of highly doped implants on low-doped active layers for cmos radiation drift detectors. *IEEE transactions on electron devices*, 2009.

[37] Poorvi L. Vora and H. Joel Trussell. Measure of goodness of a set of color-scanning filters. *J. Opt. Soc. Am. A*, 10(7):1499–1508, Jul 1993.

[38] Gaurav Sharma and H. Joel Trussell. Figures of merit for color scanners. *IEEE Trans. Image Processing*, 6:990–1001, 1997.

[39] Infineon Technologies. Bc849b, npn silicon af transistors. datasheet, Nov 2001.

[40] Texas Instruments. Tlv226x, tlv226xa advanced lincmos rail-to-rail operational amplifiers. datasheet, Aug 2006.